3 Radiopharmaceuticals for Imaging in Oncology with Special Emphasis on Positron-Emitting Agents

Brian M. Zeglis, Jason P. Holland, Artem Y. Lebedev, Melchor V. Cantorias, and Jason S. Lewis

Abstract

Over the past twenty years, nuclear imaging has arguably had more impact on oncology than any other field of medicine, particularly due to the ability of nuclear imaging to provide functional information about tumors rather than anatomical images alone. As a result, the design, synthesis, and development of cancer-targeted radiopharmaceuticals, particularly those for positron emission tomography (PET), have become areas of significant and intense investigation. A wide variety of factors must be considered in the design and synthesis of a novel, effective cancer-targeted radiopharmaceutical, including the choice of a cancer-specific molecular target capable of producing high tumor-to-background contrast, the creation of a targeting molecule able to bind the target with high specificity and affinity, the selection of a radioisotope appropriate for the pharmacokinetics of the targeting molecule, the methodology for incorporating the radiolabel into the targeting molecule, and the synthetic strategy for radiolabeling the targeting molecule. By a wide margin, the most commonly employed PET tracer in oncology is [^{18}F]-fluorodeoxyglucose ([^{18}F]FDG), an FDA-approved radiopharmaceutical that concentrates in tumors due to the tendency of many neoplasms to possess up-regulated glycolytic pathways and over-expressed glucose transporters. However, [^{18}F]FDG is far from the only cancer-targeted PET agent: a large number of effective radiopharmaceuticals have been developed to target other differences between neoplastic and normal tissue. Indeed, radiopharmaceuticals have been created to target over-expressed cell surface biomarkers (e.g. HER2/*neu* or PSMA), up-regulated processes in tumor cells (e.g. nucleic acid metabolism or amino acid transport), and traits of the tumor microenvironment (e.g. acidosis or hypoxia). In the following chapter, the fundamental principles of the design, synthesis, and development of small molecule, peptidic, and antibody-based radiopharmaceuticals will be presented along with a wide-ranging review of the most promising emerging cancer-targeted PET and SPECT imaging agents.

Keywords

Radionuclides • Radiochemistry • Cyclotron • Targetry • PET • SPECT • Radiopharmaceuticals • Small molecules • Peptides • Antibodies • Imaging in oncology

B.M. Zeglis, PhD • J.P. Holland, PhD • A.Y. Lebedev, PhD • M.V. Cantorias, PhD • J.S. Lewis, PhD (✉)
Radiochemistry and Imaging Sciences Service,
Department of Radiology, Memorial Sloan-Kettering Cancer Center,
1275 York Ave, New York, NY 10065, USA
e-mail: lewisj2@mskcc.org

H.W. Strauss et al. (eds.), *Nuclear Oncology: Pathophysiology and Clinical Applications*,
DOI 10.1007/978-0-387-48894-3_3, © Springer Science+Business Media New York 2013

Johns Hopkins University EX2023
GE Healthcare v. Johns Hopkins
IPR2026-00069

Over the last two decades, the focus of medical imaging research has shifted from its initial foundations in anatomical imaging to techniques designed to probe tissue function [1]. Variations in tissue phenotype and biochemical fluctuations in tissue metabolism have emerged as particularly important new targets [2]. Nuclear imaging methods are at the forefront of this movement. The increased sensitivity of positron emission tomography (PET) and single photon emission computed tomography (SPECT), and their ability to provide complementary information to the anatomic maps produced by other imaging modalities render them ideal for noninvasively studying the pharmacokinetics and pharmacodynamics of radiopharmaceuticals [3, 4].

This chapter begins with a brief review of the various radioimaging modalities currently employed in the clinic. This is followed by a more extensive discussion of the fundamental considerations of radiopharmaceutical design, synthesis, and production. The bulk of the chapter is dedicated to a survey of the design, development, and clinical application of radiotracers for the diagnostic imaging of cancer.

Imaging Modality Fundamentals

A review of the physics and instrumentation of radionuclide imaging is presented in Chaps. 4 and 5. In SPECT, an image is acquired using a gamma camera to record single photons emitted from a radiopharmaceutical containing a γ-ray-emitting radionuclide [4–6]. The nuclear decay characteristics of ^{99m}Tc are almost ideal for imaging: ^{99m}Tc decays by isomeric transition with a half-life of 6.01 h and emits γ-rays at 140 keV (89%). Furthermore, ^{99}Mo/^{99m}Tc generators produce sterile pertechnetate, [^{99m}Tc]-TcO_4^-, and thus facilitate in-house production of ^{99m}Tc-radiopharmaceuticals. This fortuitous combination of favorable decay characteristics and production has made ^{99m}Tc the radionuclide of choice for SPECT imaging [7].

At present, the primary clinical limitations of SPECT imaging are low image resolution and the qualitative nature of the information provided by the scan. In theory, submillimeter resolution can be achieved by SPECT imaging, but the short wavelength of γ-rays precludes the use of conventional optics to focus the radiation and produce sharp images. In practice, standard gamma cameras use a Söller collimator to filter the γ-rays, which reduces both signal intensity (typically <1% of incident radiation is collected by the detector) and spatial resolution (6–8 mm) [1, 8].

The first devices for recording images using coincident detection of the annihilation of radiation resulting from the conversion of the positron–electron pair to two 511.0 keV γ-rays were designed and built by Brownell [9] and Sweet [10] during the 1950s. The first positron emission images of localized brain tumors followed soon after, in 1953 [9]. At the same time, Wrenn et al. independently reported a method for detecting annihilation radiation [11]. It was not until the 1970s, however, that the field took a major practical step forward with the substitution of detector rings, as suggested by Ter-Pogossian and Phelps, for the planar detectors utilized by Brownell. The placement of detectors around the object increased the geometric sensitivity of the instrument.

PET is quantitative, and the coincident detection methodology dramatically decreases noise and increases spatial resolution (typically to 2–3 mm) while retaining the same functional information about tissue physiology [3, 5, 12–14]. The resolution of PET is, however, limited by the distance through which the emitted positron travels through the tissue before annihilation (typically 0.6–5 mm, depending on the radionuclide, and determined by the kinetic energy of the positron, with higher energies leading to increased distances and decreased resolution). PET is also more sensitive than SPECT; radiotracers for PET imaging are usually administered at concentrations in the range of 10^{-8}–10^{-10} M, whereas SPECT requires higher concentrations (~10^{-6} M) to achieve acceptable signal-to-noise ratios [15].

The complementary anatomic information available from CT and MRI and the functional information from SPECT and PET have fostered the development of hybrid imaging. For example, combined SPECT/CT and PET/CT cameras are now routinely used in oncology [16–19]. In one elegant study, Quon et al. used PET/CT as a presurgical tool to identify lung cancer lesions in a patient at Johns Hopkins University Hospital (Baltimore, USA) (Fig. 3.1) [18, 20].

Radiopharmaceutical Design, Synthesis, and Production

Radiolabeling

An array of chemically and radiochemically diverse radionuclides are available for PET and SPECT imaging (Fig. 3.2) [21]. Consequently, the selection of a radionuclide for a given imaging application becomes particularly important. Salient considerations include radionuclide decay characteristics (physical half-life, the types of particles emitted, particle energy and range, and the nature of daughter nuclei) and the synthetic chemistry required for incorporation of the nuclide into the radiotracer, as well as practical issues such as radiation safety, radionuclide cost, and availability. The decay characteristics of selected radionuclides which have been used for clinical investigations employing PET and SPECT imaging are reported in Tables 3.1 and 3.2, respectively [21]. In addition, the decay characteristics of selected

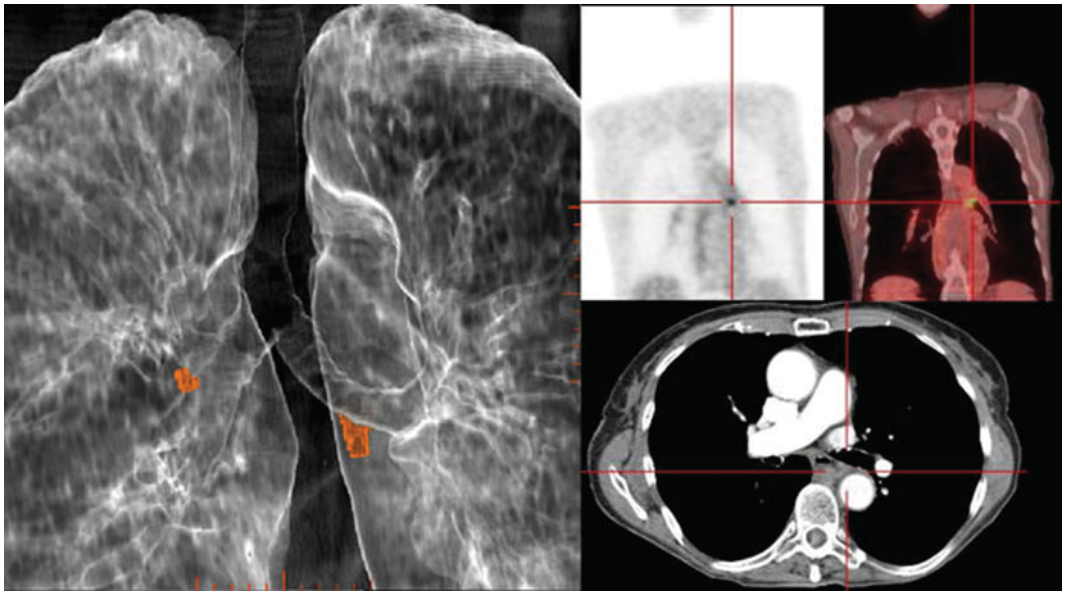

Fig. 3.1 Hybrid PET/CT image showing uptake of [^{18}F]FDG in a primary cancer lesion, a mediastinal lymph node (*orange*), and the structure of the bronchioles (*white*). (From Quon A, Napel S, Beaulieu, CF, Gambhir SS. "Flying through" and "flying around" a PET/CT scan: pilot study and development of 3D integrated [^{18}F]FDG-PET/CT for virtual bronchoscopy and colonoscopy. J Nucl Med. 2006;47:1081–7. Reprinted with permission of the Society of Nuclear Medicine)

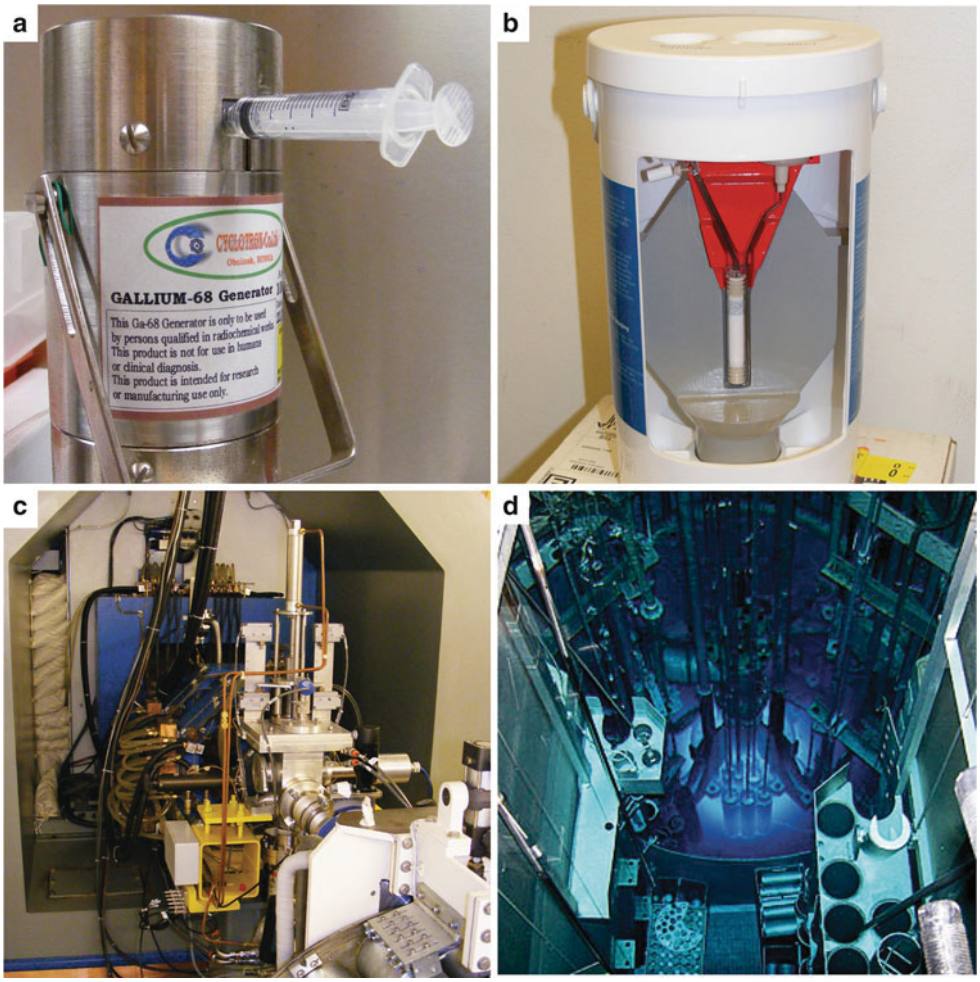

Fig. 3.2 Four methods for the production of radionuclides: (**a**) ^{68}Ga generator, (**b**) ^{99m}Tc generator, (**c**) cyclotron, and (**d**) nuclear reactor. (Courtesy of Rashid Ghani, Memorial Sloan-Kettering Cancer Center, and David Nickolaus, Missouri University Research Reactor, for the photos of the ^{99m}Tc generator and nuclear reactor, respectively)

Table 3.1 Physical decay characteristics of PET radionuclides [21]

Radionuclide	Half-life ($t_{1/2}$)	Decay mode yield/% (error)	Production route	$E(\beta^+)$/keV[a]	β^+ Endpoint energy/keV	Abundance, $I_{\beta+}$/%	E_γ/keV (intensity, I_γ/%)
Cyclotron-produced conventional PET radionuclides							
^{11}C	1,223.1 (12) s	β^+ 100	^{14}N(p,α)^{11}C	386	960	99.8	511 (200)
^{13}N	9.965 (4) min	β^+ 100	^{16}O(p,α)^{13}N	492	1,199	99.8	511 (200)
^{15}O	122.24 (16) s	β^+ 100	^{15}N(p,n)^{15}O ^{14}N(d,n)^{15}O	735	1,732	99.9	511 (200)
^{18}F	109.77 (5) min	β^+ 100	^{18}O(p,n)^{18}F ^{20}Ne(d,α)^{18}F	250	634	96.7	511 (194)
Generator-produced unconventional PET radionuclides							
^{62}Cu	9.673 (8) min	β^+ 97.4	^{62}Zn/^{62}Cu	1,316	2,926	97.2	511 (195)
^{68}Ga	67.71 (9) min	β^+ 89.1	^{68}Ge/^{68}Ga	352 836	1,899	87.9	511 (178)
Cyclotron-produced unconventional PET radionuclides							
^{60}Cu	23.7(4) m	β^+ 93	^{60}Ni(p,n)^{60}Cu	840 872 1,325	1,911 1,981 2,946	12 49 15	511 (185) 826 (22) 1,333 (88) 1,791 (45)
^{61}Cu	3.333(5) h	β^+ 61	^{61}Ni(p,n)^{61}Cu ^{60}Ni(d,n)^{61}Cu	524	1,215	51	511 (123)
^{64}Cu	12.701(2) h	ε 43.9 β^+ 17.6 β^- 38.5	^{64}Ni(p,n)^{64}Cu	278	653	18	511 (35)
^{86}Y	14.74 (2) h	ε 68.1 β^+ 31.9	^{86}Sr(p,n)^{86}Y	535	1,221	12	511 (64) 628 (36) 777 (22) 1,077 (83) 1,153 (31) 1,192 (21)
^{89}Zr	78.41 (12) h	ε 77.3 β^+ 22.7	^{89}Y(p,n)^{89}Zr	396	902	23	511 (46) 909 (99)
^{94m}Tc	52.0 (10) m	ε 29.8 β^+ 70.2	^{94}Mo(p,n)^{94m}Tc	1,094	2,439	68	511 (140) 871 (94)
^{124}I	4.1760 (3) days	ε 77.3 β^+ 22.7	^{124}Te(p,n)^{124}I	687 975	1,535 2,138	12 11	511 (45) 603 (63) 723 (10) 1,691 (11)

ε electron capture
[a]Where positrons with different energies are emitted only those with abundance >10 % are listed

Table 3.2 Physical decay characteristics of SPECT radionuclides [21]

Radionuclide	Half-life, $t_{1/2}$ (error)	Decay mode (% branching ratio)	Production route	E_γ/keV	Intensity (I_γ/%)
^{67}Ga	3.2617 (5) days	ε (100)	^{nat}Zn(p,x)^{67}Ga ^{68}Zn(p,2n)^{67}Ga	93 185 300	39 21 17
^{99m}Tc	6.01 (1) h	β^- (0.004) IT (99.996)	^{99}Mo/^{99m}Tc	141	89
^{111}In	2.8047 (4) days	ε (100)	^{111}Cd(p,n)^{111m,g}In ^{112}Cd(p,2n)^{111m,g}In	171 245	91 94
^{123}I	13.2234 (19) h	ε (100)	^{124}Xe (p,2n)^{123}Cs $\rightarrow$ ^{123}Xe $\rightarrow$ ^{123}I ^{124}Xe (p,pn)^{123}I ^{123}Te(p,n)^{123}I	159	83

ε electron capture, *IT* isomeric transition

Table 3.3 Physical decay characteristics of β-emitting radionuclides

Radionuclide	Half-life, $t_{1/2}$ (error)	Decay mode (% branching ratio)	E_{np}/keV	Abundance (I_{np}/%)[a]	E_γ/keV	Intensity (I_γ/%)
^{32}P	14.263 (3) days	β⁻ (100)	171	100	–	–
^{66}Cu	5.120 (14) min	β⁻ (100)	2,642	91	1,039	9
^{67}Cu	61.83 (12) h	β⁻ (100)	377 468 562	57 22 20	93 185	16 49
^{89}Sr	50.53 (7) days	β⁻ (100)	1,495	100	–	–
^{90}Y	64.00 (21) h	β⁻ (100)	2,280	100	–	–
^{131}I	8.0252 (6) days	β⁻ (100)	606	90	364	82
^{177}Lu	6.647 (4) days	β⁻ (100)	177 498	12 79	208	10
^{186}Re	3.7183 (11) days	ε (7.5) β⁻ (92.5)	932 1,070	22 71	137	10
^{188}Re	17.0040 (22) h	β⁻ (100)	1,965 2,120	26 70	155	16

[a]Only emissions with abundance >10 % are shown
From Welch MJ, Redvanly CS, editors. Handbook of radiopharmaceuticals: radiochemistry and applications. Chichester, UK: Wiley; 2003, with permission

Table 3.4 Physical decay characteristics of α-emitting radionuclides

Radionuclide	Half-life, $t_{1/2}$ (error)	Decay mode (% branching ratio)	E_α/keV	Abundance (I_α/%)
^{212}Bi	60.55 (6) min	α (36) β⁻(64)	6,050 690	25 10
^{213}Bi	45.59 (6) min	α (2.2) β⁻ (97.8)	5,549 5,869	0.15 2
^{211}At	7.214 (7) h	α (41.8) ε (58.2)	5,870	42
^{225}Ac	10.0 (1) days	α (100)	5,637 5,724 5,732 5,790 5,792 5,830	4 3 8 9 18 51
^{230}U	20.8 (21) days	α (100)	5,817 5,838	32 67

From Welch MJ, Redvanly CS, editors. Handbook of radiopharmaceuticals: radiochemistry and applications. Chichester, UK: Wiley; 2003, with permission

β- and α-emitting radionuclides—often employed in radiotherapeutic agents—are presented in Tables 3.3 and 3.4, respectively [21].

Radionuclides can be incorporated into PET and SPECT imaging agents in a variety of ways (Fig. 3.3): as isotopic substitutes for identical atoms in the molecular structure (e.g., [^{15}O]H_2O); as non-innocent replacements for normal molecular substituents (e.g., [^{18}F]FDG); as small, direct modifications to the building blocks of larger constructs (e.g., radioiodinated tyrosine residues in a peptide); as components of prosthetic groups coupled to macromolecules; and as metallo-radionuclides bound to large molecules modified with chelating groups (e.g., ^{89}Zr-desferrioxamine-labeled antibodies). Regardless of the labeling method, however, the exigencies of radiochemistry demand that the incorporation of a radiolabel into any imaging agent must be rapid and highly efficient. The short half-life of many PET and SPECT radionuclides (especially ^{11}C and ^{18}F) dictates that radiolabeling methods must be fast, as long reaction times would result in the decay of the activity of the radiolabel. Furthermore, the radiolabeling step in the synthesis of a tracer is often left as the final chemical transformation,

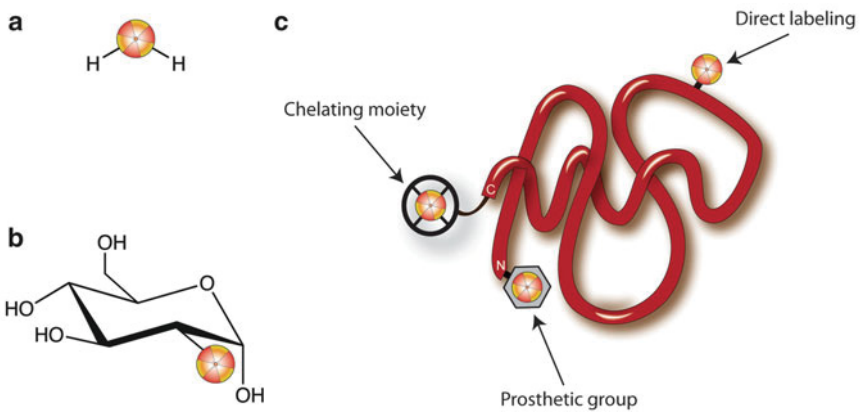

Fig. 3.3 Strategies for the incorporation of radionuclides into radiopharmaceuticals: (**a**) isotopic substitution of an identical atom in the molecular structure, $[^{15}O]H_2O$; (**b**) replacement of a key molecular substituent, $[^{18}F]$FDG; and (**c**) labeling of a macromolecule via direct, prosthetic group, and chelating group methods

minimizing the time for decay between the production of the nuclide and the completion of the radiopharmaceutical.

The efficiency of radiolabeling and the purity of the final product are also of the utmost importance in the synthesis of a radiopharmaceutical. Simply put, the specific activity of a radiotracer is the amount of radioactivity associated with a given amount of material (i.e., Bq per mass amount). Reductions in specific activity can have deleterious effects on the biodistribution of an imaging agent, primarily due to a consequent increase in competition between unlabeled agents and their radiolabeled counterparts on the cellular level; this competition not only results in attenuated accumulation of the radiotracer in the target tissue but also increased nontarget tissue uptake. For example, specific activity is of particular importance for imaging low-density steroid-based receptors. There are typically about 10,000 steroid receptors per tumor cell, and steroid ligands have binding affinities ranging from sub-nanomolar to nanomolar concentration [22]. To avoid saturating the receptors (with the possible consequence of causing a pharmacologic effect), a small injected dose of high specific-activity radiotracer is necessary.

Given these considerations, it is not surprising that the incorporation of the radionuclide is the single most important step in the synthesis of a radiotracer. Synthetic methodologies for the radiolabeling of small molecules are often either nucleophilic or electrophilic in nature, and reaction schemes can vary widely from one tracer to the next. These methods will be addressed on a case-by-case basis throughout the chapter. Strategies for radiolabeling larger molecules are more easily generalized and are presented here as a precursor to the discussion of the agents themselves.

The strategies for radiolabeling large molecules—most often peptides or antibodies—fall into two broad categories: direct and conjugate-based labeling. Direct methods are primarily used for labeling molecules with the halogen radionuclides of fluorine, bromine, iodine, and astatine. Indeed, radionuclides of iodine—including ^{123}I for SPECT, ^{124}I for PET, and ^{131}I for SPECT and radioimmunotherapy (RIT)—are particularly attractive for labeling monoclonal antibodies (mAbs). For example, in 2003, Bexxar™ ($[^{131}$I]-tositumomab) was the second radioimmunoconjugate (after $[^{90}$Y]-Zevalin in 2002) to receive United States Food and Drug Administration (USFDA) approval for use in humans as an RIT agent for B-cell lymphoma [23].

Direct iodination methods usually rely on the chemical modification of tyrosine or histidine residues. The most common iodination procedures employ electrophilic substitution using reagents that generate synthetic equivalents of the I^+ synthon—such as the H_2OI^+ cation or the mixed halogen species ICl—and give radioiodinated proteins with either mono- or di-iodinated tyrosines and/or mono-iodinated histidines (Fig. 3.4). The most frequently used reagents for the generation of ICl in situ include sodium *N*-chlorotoluenesulfonamide (chloramine-T), introduced by Greenwood et al. in 1963; Iodobeads™ (Thermo Fisher), a solid-phase analogue of chloramine-T bound to polystyrene beads; and 1,2,4,6-tetrachloro-3α,6α-diphenylglycouril (Iodogen™, Thermo Fisher), which is insoluble in water and simplifies subsequent purification steps (Fig. 3.5) [24]. Iodination reactions are often extremely fast and can go to completion at room temperature in reactions times ranging from 10 s to 30 min. Importantly, unless the reaction occurs at a residue that is particularly important for the integrity or function of the peptide, mono-iodination does not usually affect the chemical properties of the protein. However, the oxidative conditions of the iodination reaction can affect redox-sensitive functional groups such as sulfhydryls, and the iodination of tyrosine residues can lead to UV/vis spectral red shifts from the characteristic absorbance at 280 to 305–315 nm. Further, di-iodination has the potential to reduce the aqueous solubility of the labeled compound, but under the nanomolar conditions employed in radiochemical syntheses, di-iodination reactions are unlikely.

Radiohalogenations can also be achieved by employing pre-radiolabeled chemical moieties to functionalize primary amine groups (Fig. 3.6). These types of labeling reactions fall into a middle ground between direct and conjugate labeling

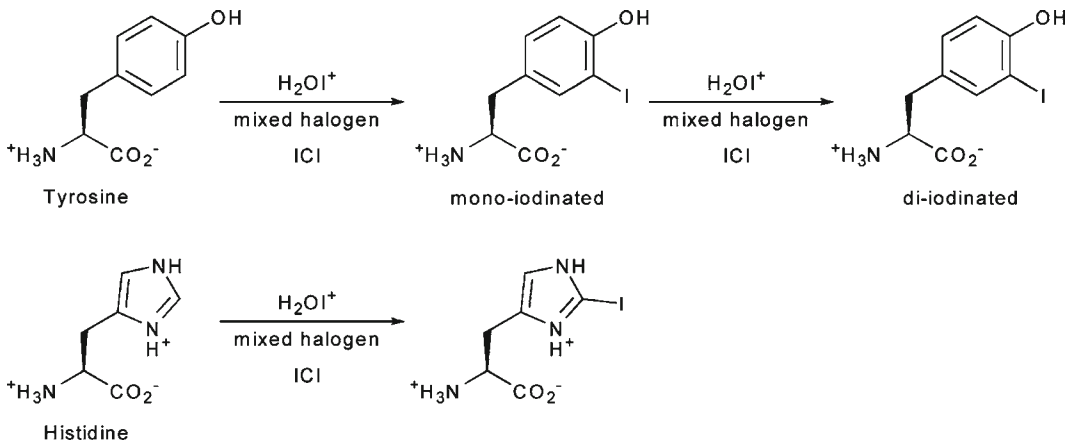

Fig. 3.4 Radioiodination of histidine and tyrosine amino acid residues

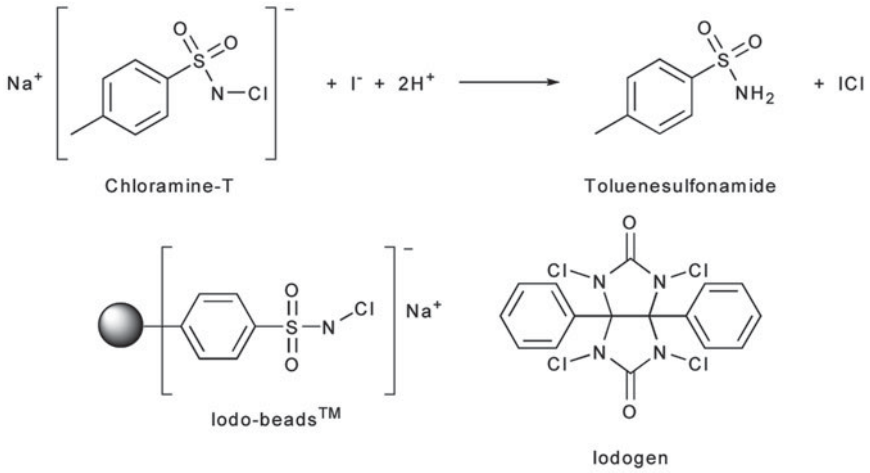

Fig. 3.5 Reagents used for oxidative generation of electrophilic iodine species for use in radioiodination reactions

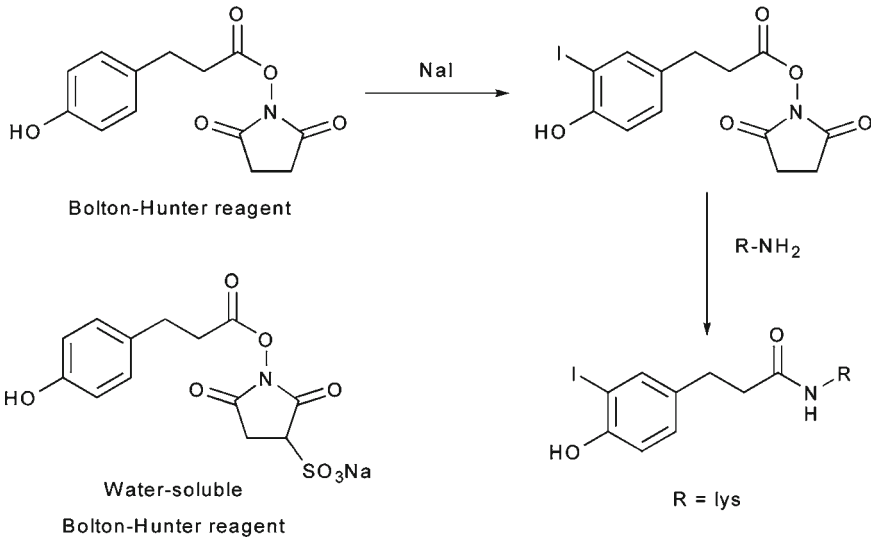

Fig. 3.6 Bolton–Hunter reagents for prosthetic-group labeling of proteins and mAbs

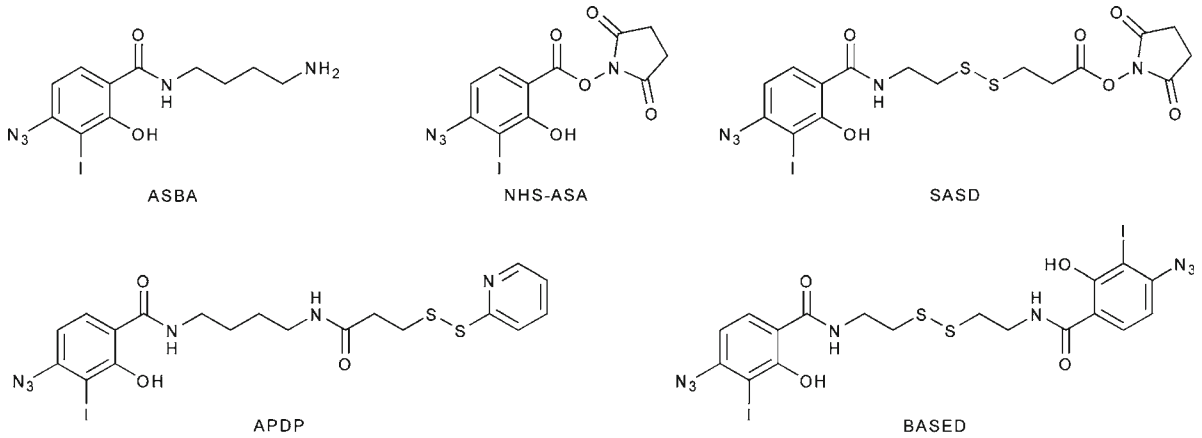

Fig. 3.7 Selected photoactive/amine-reactive cross-linking agents for radioiodination and protein functionalization reactions

and are thus often distinguished by the use of the term *prosthetic group*. Reagents for this type of labeling, most often Bolton–Hunter reagents, are commonly employed in situations in which direct radiolabeling methods are either unsuccessful or lead to the loss of function of the protein (Fig. 3.6) [24, 25]. A range of other photoactive and amine-reactive cross-linking agents based on Bolton–Hunter-type chemistry have also been developed. For example, the heterobifunctional agents 4-(*p*-azidosalicylamido)butylamine (ASBA), *N*-hydroxysuccinimidyl-4-azidosalicylic acid (NHS-ASA), *N*-[4-(*p*-azidosalicylamido)butyl]-3′-(2′-pyridyldithio) propionamide (APDP), sulfosuccinimidyl-2-(*p*-azidosalicylamido)ethyl-1,3′-dithiopropionate (SASD), and the homobifunctional agent *bis*-[β-(4-azidosalicylamido)ethyl] disulfide (BASED) are often employed for prosthetic group radioiodination and cross-linking reactions (Fig. 3.7) [24].

Conjugate radiolabeling methods are most frequently used for radiolabeling peptides, mAbs, and antibody fragments with metallo-radionuclides such as $^{60/61/62/64/67}$Cu, $^{67/68}$Ga, $^{86/90}$Y, ^{89}Zr, ^{111}In, and ^{225}Ac. Conjugate labeling involves the covalent derivatization of the molecule of choice with a bifunctional chelate via a chemically stable linker. Bifunctional chelates are chelating or macrocyclic ligands which both bind avidly to metal ions and have the ability to be covalently appended to biologically active targeting vectors. Interestingly, conjugation to biologically active molecules can be accomplished either before or after radiolabeling of the chelate. However, the functionalization of mAbs with post-radiolabeled chelates provides better control over the chemistry and thus often allows for the preparation of radiolabeled species in higher specific activity than analogous pre-radiolabeling routes. Selected examples of the more common chelates employed in conjugation and metallo-radiolabeling are presented in Fig. 3.8 [25, 26].

The thermodynamics and kinetics of metal ion complexation are dependent on the size, charge, and electronic configuration of the metal ion, as well as the number and types of donor atoms, charge, and cavity size of the chelating ligand. An ideal chelate has facile kinetics for metal ion complexation under mild conditions (temperature, pH, solvents) and leads to the formation of a complex with high thermodynamic and kinetic stability. For example, 1,4,7,10-tetraazacyclododecane-1,4,7,10-tetraacetic acid (DOTA) is a 12-membered tetraazamacrocycle with additional acetate functionalization at each of the four nitrogen atoms (Fig. 3.8) [27]. DOTA has a remarkable scope for complexing metal ions with +2 and +3 charges and is thus often used for binding the metallo-radionuclides of Cu, Ga, Y, In, Lu, and Ac. The scope and flexibility of DOTA chelation chemistry have been the principal driving forces behind the widespread use of this ligand in radiopharmaceutical applications.

Other common chelates and macrocycles include diethylenetriamine pentaacetic acid (DTPA) for use in the complexation of ^{111}In and $^{86/90}$Y and the naturally occurring bacterial siderophore desferrioxamine B (DFO). DFO, isolated from *Streptomyces pilosus*, has recently been exploited for chelation of $^{89}Zr^{4+}$ ions in the radiolabeling of mAbs for immuno-PET [28–31]. Furthermore, a variety of chelating and macrocyclic derivatives which contain an aryl isothiocyanate functional group for conjugation to the amines of biologically active vectors have also been reported [26].

Radiopharmaceutical Design

The ultimate goals in the development of any radiotracer are high target accumulation and low background activity. In pursuit of these objectives, the concerns in the design of novel, effective agents do not end with the production of the radiotracer. In practice, the development of a radiopharmaceutical often requires a delicate balancing act. In the case of a receptor-targeted small molecule, for example, the binding

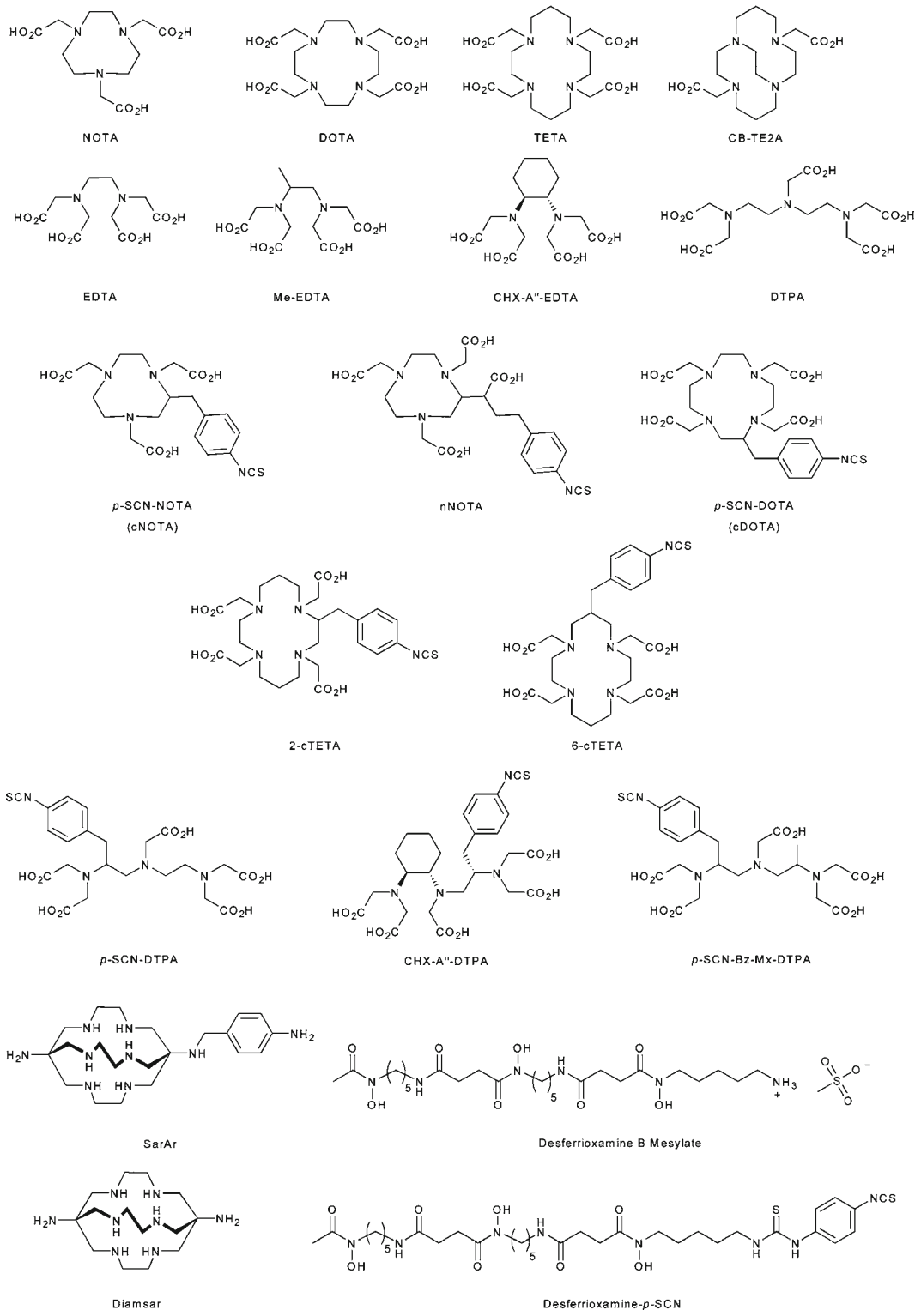

Fig. 3.8 Chelating and macrocyclic ligands used for metallo-radionuclide complexation and mAb conjugation

properties of the tracer for its target receptor must be given the utmost consideration; it is important that the tracers are sufficiently selective, with high binding affinity for the target and low binding affinity for other competing receptors [32]. The radiolabeling chemistry must also not perturb the affinity of the radiotracer for its receptor. It is possible that the incorporation of a radionuclide near the receptor-binding region of the small molecule can dramatically alter the interactions

between the receptor and its ligand [33]. Additionally, lipophilicity is an important factor, as small molecules which are weakly to moderately lipophilic have a lower degree of nonspecific binding than those exhibiting high lipophilicity [34]. Finally, when designing an agent for brain imaging, the size, charge, and lipophilicity of a radiopharmaceutical must all be considered in the context of crossing the blood–brain barrier [35].

Pharmacokinetic properties such as the rate and stability of uptake at the target and clearance from nontarget tissues are also important parameters in achieving high target-to-background contrast ratios. An ideal imaging agent should be cleared rapidly from background tissues that are close to the target site. Very rapid uptake at the target makes the agent very dependent on perfusion. On the other hand, slow uptake (as often occurs with larger molecules such as antibodies) allows the concentration of the radiopharmaceutical at the target to reflect the concentration of receptors/antigen. The clearance rate from nontarget tissue (e.g., blood pool and extravascular tissue) is reasonable when it allows an imaging agent to accumulate sufficiently to provide a target-to-background ratio > 1.5 at a time when there is sufficient activity remaining to allow collecting PET or SPECT images in < 20 min/view. Target-to-background contrast is also influenced by the stability of radiotracers. An imaging agent with low resistance to metabolic degradation is far more likely to produce metabolites prone to circulation in the bloodstream, thereby increasing background activity and decreasing image contrast [36].

Quality Control

After the aseptic preparation and formulation of a radiopharmaceutical, several experiments must be conducted to ensure that the product is of suitable quality for in vivo clinical use. Simple physical and chemical tests are employed to measure the radiochemical and radionuclidic purity of the agents; these include instant thin-layer chromatography (ITLC), size-exclusion chromatography (SEC), and radio-analytical high-performance liquid chromatography (radio-HPLC), as well as γ-spectroscopy using a cryo-cooled, high-purity GeLi detector coupled to a multichannel analyzer (MCA). In the case of shorter-lived radionuclides (^{11}C, ^{18}F, ^{68}Ga, etc.), the identity of the radionuclide is also confirmed by monitoring the rate of radioactive decay and thus measuring the half-life. Once the radiochemical purity of an agent has been established, its chemical identity must be confirmed independently. This is often achieved chromatographically by demonstrating co-elution of the radiolabeled compound with a known standard. Other essential tests of newly produced radiopharmaceuticals include endotoxin and pyrogenicity measurements, as well as residual organic solvent measurements using gas-phase chromatography (GC). For human studies, clinical trials investigating factors such as biodistribution, dosimetry, and immunogenicity must be conducted before a product can be considered safe. It is important to note that in the USA, all quality control standards are governed by the United States Pharmacopeia (USP), General Chapters 797 and 823.

The Ubiquitous Agent: 2-[^{18}F]Fluoro-2-deoxy-D-glucose

2-[^{18}F]Fluoro-2-deoxy-D-glucose ([^{18}F]FDG) is the most prominent PET imaging agent, and its use in both basic science and clinical practice has fundamentally changed our understanding of cancer. [^{18}F]FDG (Fig. 3.9) was first synthesized at the Brookhaven National Laboratory in the late 1970s, and its potential for applications in oncology continues to be the subject of extensive laboratory and clinical research [37, 38]. In 1998, [^{18}F]FDG was approved by the Health Care Financing Administration for coverage of the evaluation of indeterminate solitary pulmonary nodules and the initial staging of lung cancer. In 2000, the USFDA likewise approved [^{18}F]FDG for assisting in the "evaluation of malignancy in patients with known or suspected abnormalities found by other testing modalities, or in patients with existing diagnoses of cancer." [39] These two important decisions laid the foundation for a dramatic increase in the clinical use of [^{18}F]FDG in oncology; [^{18}F]FDG-PET has now been approved for investigating a wide variety of malignancies and has become a routine clinical tool in the diagnosis and management of many cancers [40].

The accumulation of [^{18}F]FDG in tumors is predicated on the increased rate of glycolysis of cancer cells relative to normal cells [41]. This characteristic of cancer cells was first reported over 80 years ago by Otto Warburg and is thus now commonly referred to as the Warburg Effect [42]. The underlying causative mechanisms for the Warburg Effect remain the subject of considerable debate [43]; however, it is well-known that malignant tumors overexpress both glycolytic enzymes and glucose transporters [44–46]. Further, a number of other modifications which promote glycolysis have also been observed in cancer cells. Notably, elevated levels

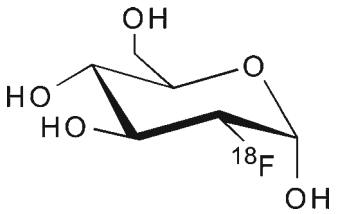

Fig. 3.9 The structure of 2-[^{18}F]fluoro2-deoxy-D-glucose

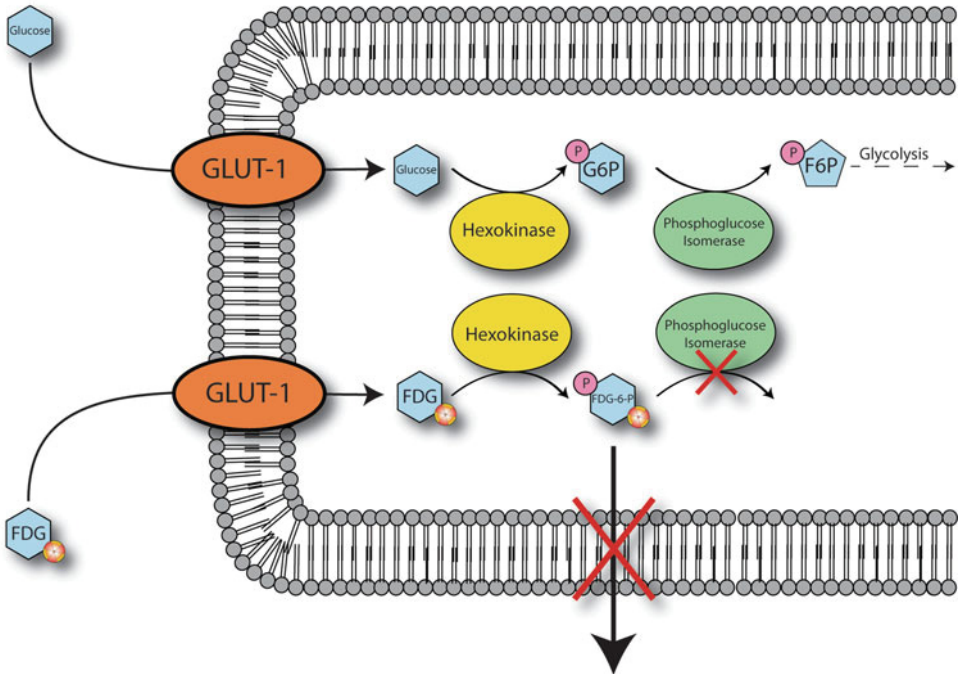

Fig. 3.10 Proposed mechanism for the cellular accumulation of [^{18}F]FDG

of the glycolysis activator fructose-2,6-bisphosphonate and the presence of high levels of hexokinase in the membranes of mitochondria are common characteristics of tumors [47]. From a medical imaging perspective, however, more important than the proximal and immediate causes of the Warburg Effect is the simple fact that many tumors exhibit dramatically augmented rates of glucose—and thus [^{18}F]FDG—uptake.

[^{18}F]FDG, like glucose, enters cells via facilitated diffusion through sodium-independent glucose transporters (Fig. 3.10) [48]. One of these transporters, GLUT-1, is often overexpressed in tumor cells, and high expression levels of others (notably GLUT-3 and GLUT-12) have also recently been reported [46]. Once inside the cell, [^{18}F]FDG follows the normal glucose metabolic pathway and is phosphorylated by hexokinase (also overexpressed in many tumor cells) to form 2-[^{18}F]fluoro-2-deoxy-D-glucose-6-phosphate ([^{18}F]FDG-6P). At this point, the metabolic fates of glucose and [^{18}F]FDG diverge. Glucose-6-phosphate is first converted to fructose-6-phosphate by phosphoglucose isomerase, irreversibly phosphorylated to fructose-1,6-bisphosphate by phosphofructokinase, and then continues on in the glycolytic pathway [49]. In contrast, the fluorine atom in [^{18}F]FDG-6P precludes its conversion by phosphoglucose isomerase, thereby preventing further progression through the glycolytic cycle. The presence of the charged phosphate group prevents [^{18}F]FDG-6P from leaving the cell. In theory, dephosphorylation by glucose-6-phosphatase could reverse the phosphorylation process, thereby facilitating excretion of [^{18}F]FDG from the cell; however, many tumor cells exhibit very low levels of glucose-6-phosphatase, making this pathway unlikely [50]. Thus, [^{18}F]FDG-6P is sequestered in the cell, and as tumor cells are often characterized by increased rates of glycolysis, [^{18}F]FDG-6P tends to accumulate to a greater extent in tumors than in normal tissue.

[^{18}F]FDG does not localize exclusively in malignant tissues [51]. High levels of [^{18}F]FDG uptake are often observed in the brain, kidneys, liver, gastrointestinal tract, and laryngeal muscles [52], with excreted activity in the urinary bladder. In contrast, [^{18}F]FDG uptake in the breasts, mediastinum, and bone marrow is minimal, and muscular uptake is normally negligible, though exercise can lead to uptake in skeletal muscle, and hyperventilation can prompt uptake in the diaphragm [53].

As with all imaging modalities, [^{18}F]FDG-PET has a number of limitations [54]. First, not all tumors exhibit elevated rates of glycolysis. For example, bronchioloalveolar carcinoma [55], many mucin-producing tumors, and other well-differentiated tumors like early prostate cancer [56] often exhibit inherently low uptake of [^{18}F]FDG. Second, inflammation with activation of macrophages can also lead to elevated levels of [^{18}F]FDG uptake and thus false-positive results [57, 58]. Third, variations in blood glucose levels can dramatically alter [^{18}F]FDG uptake; this issue becomes especially important with diabetic patients. Fourth, the limited spatial resolution of commercial systems can lead to false-negative results when dealing with particularly small tumors

Table 3.5 Detection of metastases by [^{18}F]FDG-PET

Cancer location/type	Patients	Site	Sensitivity	Specificity
Breast [257]	44	Bone	84	99
Breast [258]	50	LN	95	66
Breast [259]	23	LN	94	100
Cervical [260]	33	Local	60	94
Colon [261]	42	Liver	100	100
Colon [262]	28	Extrahepatic or hepatic	100	91
Colon [263]	68	Distant and local	95	83
Colon [264]	37	Liver	88	100
Head and neck [265]	60	LN	90	94
Melanoma [266]	38	Liver	91	92
Nasopharyngeal [267]	95	Distant	100	90
NSCLC [65]	120	LN	100	98
NSCLC [65]	120	Distant	98	92
NSCLC [268]	110	Bone	90	98
Ovarian [269]	50	Staging	87	100
Prostate [270]	24	LN	75	100
Salivary [271]	48	Staging	93	96
Renal [272]	53	Liver	100	94
Renal [273]	15	Lung	90	80
Gastric [274]	68	LN	94	92
Esophageal [275]	91	Distant	57	97

Adapted from Gillies RJ, Robey I, Gatenby RA. Causes and consequences of increased glucose metabolism of cancers. J Nucl Med. 2008;49:24S–42S, with permission

[59, 60]. Finally, the physiologically high levels of [^{18}F]FDG in the brain (vide infra) limit the applicability of [^{18}F]FDG-PET scans in brain tumor imaging.

From an analytical perspective, while qualitative examination plays a significant role in the assessment of PET images, quantitative measures—most notably standardized uptake values (SUV)—also play an important role in the evaluation of [^{18}F]FDG uptake [61]. The SUV is a ratio between the concentration of a radiotracer in a particular area of the body (e.g., a tumor) and its concentration in the entire body if it were uniformly distributed throughout [62]. Practically, SUVs are obtained by determining the activity of a radiotracer in a given region of interest (in microcuries per cubic centimeter) and dividing this value by the injected dose divided by the patient's body mass:

$$\mathrm{SUV} = \frac{\mu\mathrm{Ci}\,/\,\mathrm{mL\ of\ tissue}}{\mu\mathrm{Ci\ injected}\,/\,\mathrm{g\ body\ mass}}.$$

While the methods of calculating SUVs can vary and are thus subject to debate, a few basic requirements exist, including the use of attenuation-corrected scans, accurate image calibration, and body weight measurements. In the case of [^{18}F]FDG, SUVs can provide a valuable quantitative counterpart to the normally qualitative analysis of PET images. In pulmonary lesions, for example, a cutoff SUV of 2.5 is generally accepted for differentiating between benign and malignant tissues [40]. Furthermore, [^{18}F]FDG values have also been shown to be useful in the assessment of treatment efficacy. In one study, dramatic (over 60%) decreases in [^{18}F]FDG SUVs were observed after chemotherapeutic treatment in patients with non-Hodgkin's lymphoma [63].

In the clinic, [^{18}F]FDG is employed in the diagnosis, staging, and restaging of a wide variety of tumors. Particularly notable is the effectiveness of [^{18}F]FDG in the detection of distant metastases; an assessment of a variety of clinical studies showed that for the majority of distant metastases, the sensitivity and specificity of [^{18}F]FDG-PET are well over 85% (Table 3.5, Fig. 3.11) [43, 64, 65]. Specific applications of [^{18}F]FDG have been reviewed elsewhere [40, 51, 64, 66, 67], and a recent special contribution describing "Recommendations on the Use of [^{18}F]FDG-PET in Oncology" has been published in the *Journal of Nuclear Medicine* [68]. Further examples of the use of [^{18}F]FDG appear throughout this book.

Imaging the Tumor Microenvironment

The molecular imaging of tumors is often predicated on exploiting differences between neoplastic and normal tissue. From a targeting perspective, these phenotypic abnormalities fall into two broad categories: those characteristic of individual cells (e.g., the presence or absence of particular cancer biomarkers) and those characteristic of the tumor

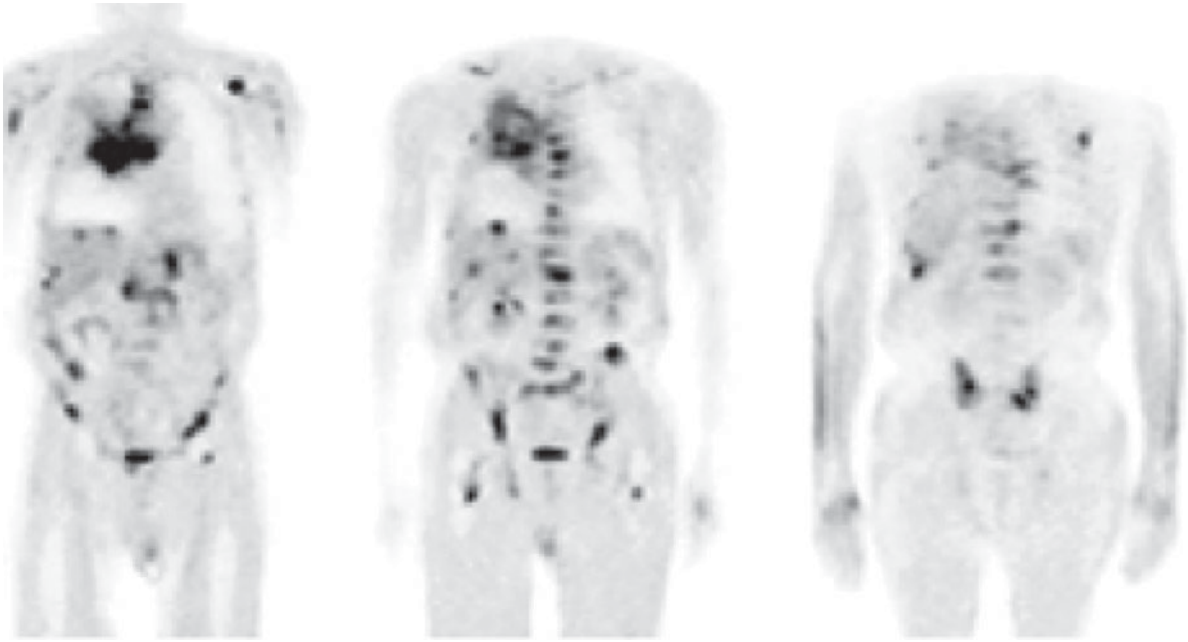

Fig. 3.11 A 69-year-old man with SCLC and multiple metastases. Coronal [^{18}F]FDG-PET images show the primary tumor in the right lung and mediastinum and metastases in the liver and right adrenal gland, the thoracic and lumbar spine, ribs, upper limbs, femora, and pelvis. (From Brink I, Schumacher T, Mix M, et al. Impact of [^{18}F]FDG-PET on the primary staging of small-cell lung cancer. Eur J Nucl Med Mol Imaging 2004;31, with permission of Springer Science and Business Media)

microenvironment as a whole (for instance, the hypoxic or acidic nature of many tumors). The following sections discuss radiopharmaceuticals which target properties of the tumor microenvironment, specifically agents which exploit abnormalities in tumor angiogenesis, perfusion, and hypoxia.

Imaging the Tumor Microenvironment: Angiogenesis

Angiogenesis is the fundamental process by which new vascular channels are formed from preexisting ones, as seen, for example, in the repair and regeneration of tissue during wound healing [69]. If the growth of new blood vessels requires the differentiation of cell precursors (angioblasts) into endothelial cells (e.g., in embryonic development), the phenomenon is strictly referred to as vasculogenesis [70]. In general, angiogenesis is tightly regulated by a balanced interaction between stimulatory and inhibitory signaling molecules [71]. However, if this dynamic balance is perturbed by, for example, a primary tumor that releases vascular endothelial growth factors (VEGF), the rapid proliferation of new vessels can occur (Fig. 3.12) [72].

In cancer, angiogenesis is essential to the survival and growth of developing tumors. When a tumor is smaller than a few millimeters across, it can readily gain oxygen and nutrients via passive diffusion through neighboring tissues. To permit the tumor to grow larger than a few millimeters, however, the tumor requires dedicated blood vessels to supply the developing malignancy with nutrients. In contrast to the vasculature of normal organs, the neovasculature of tumors is a heterogeneous network of leaky, dilated, irregular blood vessels through which the tumor can receive both oxygen and nutrients [73, 74].

Given its paramount importance in the development of tumors, angiogenesis has received considerable attention as a target for chemotherapeutic agents. The first antiangiogenic drug approved by the USFDA was a humanized monoclonal antibody called bevacizumab which targets VEGF [75]. Indeed, much of the focus in the development of angiogenesis radiotracers has been given to two classes of stimulatory signaling pathways: the VEGF/VEGF receptor (VEGFR) and integrin pathways. Peptides, monoclonal antibodies, and proteins have been labeled with various radionuclides and have been used with either SPECT or PET to target the angiogenic modulators. Radionuclide-based nanoparticles are also currently under investigation for the multi-modality imaging of these pathways [76].

The VEGF/VEGFR signaling pathway is mediated by a class of receptor tyrosine kinases, namely VEGFR-1 (Flt-1/FLT-1) and VEGFR-2 (Flk-1/KDR). VEGFR-2 is preferred over VEGFR-1 as a target for imaging agents because laboratory studies demonstrated high VEGFR-1 expression in rodent kidneys, which are considered a dose-limiting organ. In addition, VEGFR-2 is the major mediator of the mitogenic, angiogenic, and permeability-enhancing effects

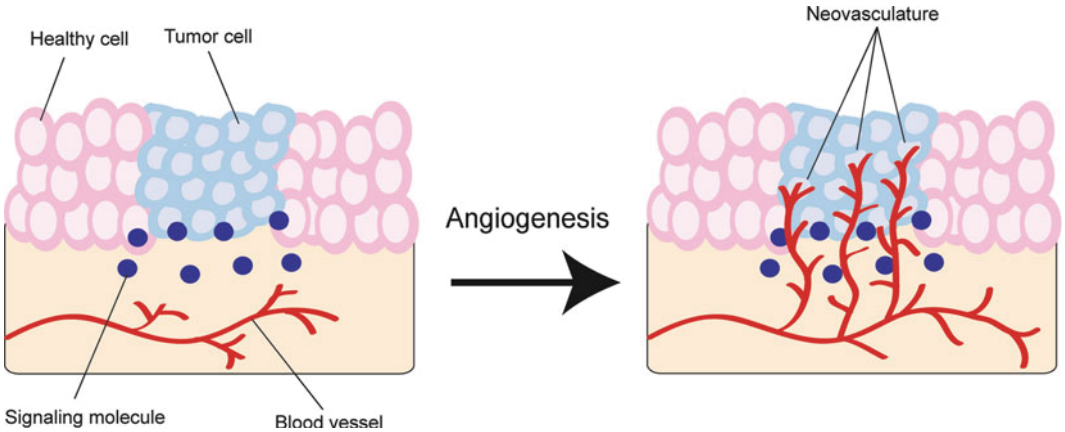

Fig. 3.12 Schematic representation of the process of angiogenesis. The formation of heterogeneous neovasculature in and around the nascent tumor will provide it with both essential nutrients for growth and survival and an avenue for metastasis

of VEGF [71]. A recent report by Cai et al. demonstrated that [^{64}Cu(DOTA)]-VEGF$_{121}$ has nanomolar binding affinity to VEGFR-2, and blocking studies with non-radiolabeled VEGF$_{121}$ confirmed that binding of the radiotracer is specific for VEGFR [77]. In the same study, PET imaging of [^{64}Cu(DOTA)]-VEGF$_{121}$ showed a significant difference in tumor uptake between small and large U87MG tumors. In highly vascularized small tumors where VEGFR-2 expression is high, the tracer localized rapidly, achieving a concentration of about 15%ID/g; in contrast, large tumors with low VEGFR-2 expression levels had sporadic, low tumor uptake of about 3%ID/g. In a Phase I clinical trial, 20 patients with progressive solid tumors were treated with various doses of HuMV833, a humanized version of a murine anti-VEGF mAb MV833. The same patients were also treated with [^{124}I]-HuMV833 to measure the distribution and clearance of HuM833 with PET. The PET data demonstrated that on a per-patient and per-lesion basis, tumor biology is heterogeneous [78].

Another pathway, integrin signaling, can also be exploited for imaging tumor angiogenesis. Integrins are cell adhesion molecules that are expressed on either endothelial or carcinoma cells. There are 24 known integrin molecules with distinct adhesive properties [79]. Among them, the most studied is $\alpha_v\beta_3$, which is found on both tumor neovasculature and tumor cells. Peptides containing an integrin-binding, arginine-glycine-aspartic acid (RGD) peptide motif have been labeled with various radionuclides to image tumor angiogenesis in models which overexpress $\alpha_v\beta_3$ [80]. For example, Galacto-RGD labeled with ^{18}F was studied in 19 cancer patients: 7 had metastatic melanomas, 10 had sarcomas, and 2 had osseous metastases. Dynamic PET scans of the tumors over 60 min followed by static scans revealed an SUV range of 1.2–9.0 at various tumor sites, demonstrating that ^{18}F-Galacto-RGD PET allows imaging of $\alpha_v\beta_3$ integrin expression in tumors with high contrast (Fig. 3.13) [81].

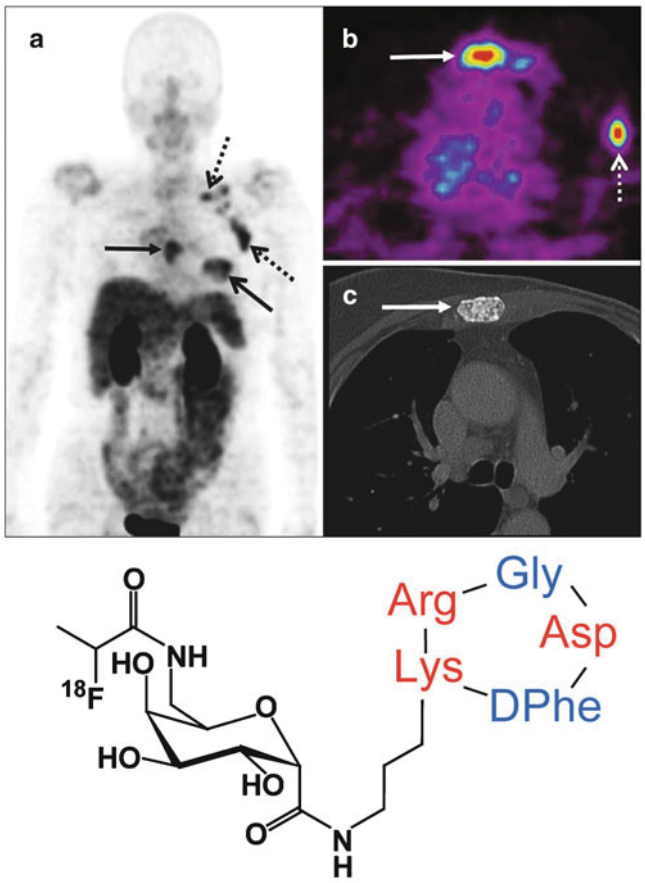

Fig. 3.13 Patient with invasive ductal breast cancer of the left breast (*arrow, open tip*), axillary lymph node metastases on the left side (*arrow, open tip, dotted line*), and an osseous metastasis to the sternum (*arrow, closed tip*). The maximum intensity projection of the ^{18}F-Galacto-RGD PET [(**a**), stand-alone PET] and the planar image [(**b**), stand-alone PET, (**c**), CT, separate scan] show the primary tumor, the lymph node metastases and the osseous metastasis (**d**) Structure of ^{18}F-Galacto-RGD. (From Beer AJ, Schwaiger M. Imaging of integrin $\alpha_v\beta_3$ expression. Cancer Metastasis Rev. 2008;27:631–44, with kind permission of Springer Science and Business Media)

Imaging the Tumor Microenvironment: Perfusion

Perfusion of the tumor and surrounding tissues also holds tremendous promise as a clinical tool for the planning, monitoring, and evaluation of therapy. In recent years, tracers bearing PET radionuclides such as ^{13}N and ^{82}Rb have been used extensively in the evaluation of myocardial, cerebral, and pulmonary perfusion [82–84]. However, despite their significant potential, the clinical impact of PET and SPECT radiotracers for imaging tumor perfusion has been limited.

$[^{15}O]H_2O$ is one of the most promising radiotracers for PET imaging of tumor perfusion [85]. The radiotracer diffuses passively through membranes, has 100% first-pass tissue extraction, and, due to the abundance of unlabeled water in the body, does not participate appreciably in metabolic processes over the time course of a typical study. Therefore, $[^{15}O]H_2O$ can be described as an inert tracer and can provide clinicians with highly accurate quantifications of tumor blood flow [86]. Furthermore, $[^{15}O]H_2O$ is easily produced with small cyclotrons, has a half-life (2 min) suitable for repeat experiments, and has favorable dosimetric properties. Finally, from a practical standpoint, $[^{15}O]H_2O$ can be administered by several routes including bolus injection, continuous intravenous infusion, and, interestingly, as $[^{15}O]CO_2$, which is converted to $[^{15}O]H_2O$ by carbonic anhydrase in the lungs.

Over the past 15 years, $[^{15}O]H_2O$ has most frequently been employed in investigations of blood flow, hypoxia, and neovascularization in primary and secondary brain tumors [87, 88]. Furthermore, $[^{15}O]H_2O$ has been utilized in the clinical assessment of perfusion in breast [89–91], renal [92], intra-abdominal [93], colon [94], and lung [95–97] cancers and has also been used to evaluate vasculature-targeting chemotherapeutic treatments [98, 99]. For example, $[^{15}O]H_2O$ and $[^{18}F]$FDG were used in conjunction to measure the blood flow and glycolytic activity of solid tumors before and after treatment with the antiangiogenic chemotherapeutic human recombinant endostatin (Fig. 3.14) [98]. In another investigation, $[^{15}O]H_2O$ was successfully employed to measure the reduction in perfusion of solid tumors in patients treated with the vasculature-targeting agent combretastatin A4 phosphate (CA4P) [100]. Interestingly, $[^{15}O]H_2O$ and $[^{15}O]CO$ have often been employed together in investigations as tracers for tumor perfusion and blood volume, respectively [86, 88, 100].

Not surprisingly, several important drawbacks to the use of $[^{15}O]H_2O$ in perfusion imaging exist. Most notably, the $[^{15}O]H_2O$ blood flow model becomes unreliable at high flow rates, a consequence of the dependence of the model on the difference between the time–activity curves of arteries and tissue. However, this is not a major concern in *tumor* perfusion imaging, as the flow rates in the heterogeneous neovasculature of tumors are usually low. In addition, increased activity at the site of administration may obscure organs or sites of interest. Finally, the temporal and spatial resolution of $[^{15}O]H_2O$ PET dictate that it provides a measure of perfusion of the whole region of interest throughout the duration of the scan. Consequently, microscopic (i.e., within a specific area of a small tumor) and ephemeral (i.e., within a small amount of time) changes in blood flow cannot be measured accurately.

Copper complexes of pyruvaldehyde *bis*(4-*N*-methyl-3-thiosemicarbazone) — $[^{62}Cu^{II}PTSM]$ ($t_{1/2}$ = 9.8 min.) or $[^{64}Cu^{II}PTSM]$ ($t_{1/2}$ = 12.7 h) — have also shown potential as blood flow tracers in the brain, myocardium, and kidney [3, 83, 101–103]. Given their success as imaging agents in normal tissue, they have also been subject to considerable interest as tracers of tumor perfusion [104–106]. The lipophilic metal complexes travel through the blood stream and freely diffuse across cell membranes; once inside the cell, however, sulfhydryl groups reduce the copper from Cu^{II} to Cu^{I}, and subsequent proton-mediated ligand-dissociation sequesters the radionuclide within the cytoplasm. To date, the complexes have been employed in the imaging of models of spontaneous neoplasms [105] and colorectal cancer [106] and in evaluation of the performance of chemotherapeutics in colorectal liver metastases [104]. However, Cu-*bis*(thiosemicarbazonato) complexes have so far failed to have significant impact in the clinic, as their lipophilicity leads to a high affinity for serum albumin, a property which reduces tissue uptake at high rates of blood flow [107]. Subsequent generations of these compounds have sought to decrease lipophilicity by functionalizing the complex with hydrophilic groups, including glucose [108, 109].

Other PET perfusion imaging agents include $[^{13}N]NH_3$, $[^{82}Rb]RbCl$, $[^{201}Tl]TlCl$, ^{18}F-fluoromethane, and ^{68}Ga-citrate. These radiotracers are mostly used in brain and myocardial imaging but have also received attention from the oncologic imaging community [83, 110]. However, each has inherent limitations that seriously impair its suitability for imaging tumor perfusion. For example, while $[^{13}N]NH_3$ has been employed in a small number of brain tumor perfusion studies [111], both its participation in the glutamine synthetase metabolic pathway and concerns about its reliable extraction into tissues have limited its application in clinical cancer research; ^{201}Tl has poor spatial resolution resulting from its lower energy photons, and $[^{82}Rb]RbCl$, while an attractive tracer for myocardial imaging, has been limited by the variability in its extraction from blood by various normal and malignant tissues. Clearly, despite some important successes, the measurement of tumor perfusion with PET remains very much a developing field.

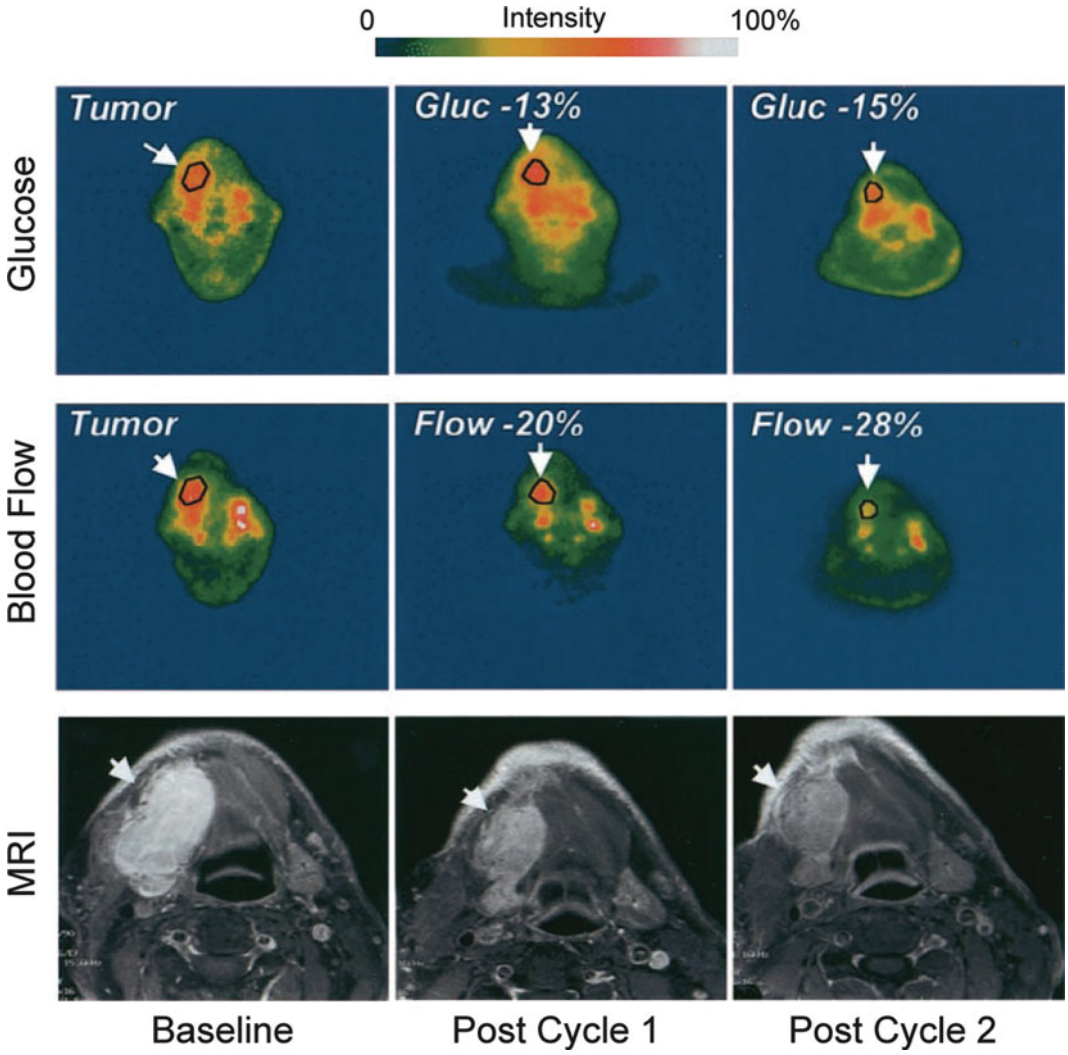

Fig. 3.14 PET scans before and after antiangiogenic treatment with human recombinant endostatin of a representative patient with synovial cell carcinoma of the mandible. Scans depicting both tumor glycolytic activity ([^{18}F]FDG) and perfusion ([^{15}O]H_2O) are shown alongside MRI scans of the lesion. Tumor glucose metabolism and blood flow decreased with each interval of tumor measurement, and the mass also decreased in size during the same period of treatment. (Adapted from Herbst RS, Mullani NA, Davis DW, et al. Development of biologic markers of response and assessment of antiangiogenic activity in a clinical trial of human recombinant endostatin. J Clin Oncol. 2002;20:3804–14. © 2008 American Society of Clinical Oncology. All rights reserved)

Imaging the Tumor Microenvironment: Hypoxia

Hypoxia is a pathological condition characterized by reduced levels of tissue oxygenation; hypoxic cells have oxygenation levels of <3 mmHg, compared to 20–80 mmHg for their normal counterparts [112, 113]. In tumors, vascular irregularities can lead to inefficient supplies of oxygen (ischemic hypoxia) and other nutrients to rapidly proliferating regions. The severity of tumor hypoxia is highly dependent on the cancer phenotype; for example, hypoxia is often particularly severe in cervical cancer [114]. Furthermore, the presence of hypoxia is associated with other important changes in the tumor microenvironment, including the stimulation of angio- and vasculogenesis, apoptosis, and an increased propensity for tumor invasion and metastasis [115]. In the clinical setting, patients with hypoxic tumors have been shown to have a poorer prognosis for disease-free survival after standard surgical, chemo-, or radiotherapeutic treatment [116–118].

Hypoxia also presents a problem for standard chemo- and radiotherapeutic treatment. Gray et al. demonstrated that the presence of oxygen at the time of irradiation is responsible for radiation sensitivity [112, 119]. Furthermore, the origins of chemotherapeutic resistance involve several factors which include altered gene expression and changes in the rate of

cell cycle progression [120]. As most anticancer drugs target rapidly proliferating cells, the decreased rate of cell cycle progression with increasing distance from tumor vasculature causes decreased cytotoxicity in hypoxic tissues. In addition, the concentration of anticancer drug decreases with increased distance from the capillaries, a consequence of both the limited diffusion and high reactivity of most drugs. The limited diffusion of drugs from blood vessels is a major problem of targeted therapies and is also an important consideration for radiopharmaceutical development. Figure 3.15 shows the relative change in tissue oxygen concentration as a function of distance from blood vessels.

A range of radiotracers have been developed as potential hypoxia-selective imaging agents (Fig. 3.16). Most of these have been developed for use with PET imaging. In particular, two agents, ^{18}F-fluoromisonidazole (^{18}F-FMISO) and the $^{64}Cu^{II}$ complex of the diacetyl-2,3-*bis*(4-*N*-methyl-3-thiosemicarbazonato) ligand ([$^{64}Cu^{II}$ATSM]) have been translated for use in the clinic. Extensive mechanistic studies have also been reported for both nitroimidazoles [121] and copper *bis*(thiosemicarbazonato) complexes [122–124]. With regard to the metal complexes, selectivity for hypoxia both in vitro and in vivo is thought to be the result of delicate equilibria involving the initial reduction of the compound to give an anionic species, protonation, and subsequent metabolism [122]. [$^{64}Cu^{II}$ATSM], for example, can freely diffuse in and out of normoxic cells, but the altered redox environment of hypoxic cells leads to its selective metabolic trapping. The performance of ^{18}F-FMISO and [$^{64}Cu^{II}$ATSM] for PET imaging of hypoxia are the subject of ongoing Phase I/II clinical trials [125–127].

In 2006, Yuan et al. validated [$^{64}Cu^{II}$ATSM] as a radiopharmaceutical for delineating hypoxia both by performing in vivo PET studies and also by comparing the autoradiographic distributions of [$^{64}Cu^{II}$ATSM] in tumor slices with the well-established hypoxia markers EF5, pimonidazole, and carbonic anhydrase IX [128]. This study confirmed that [$^{64}Cu^{II}$ATSM] is a valid PET marker of hypoxia for some but not all tumors. In the clinic, [$^{64}Cu^{II}$ATSM] has been used successfully for imaging lung metastasis [127] and cervical

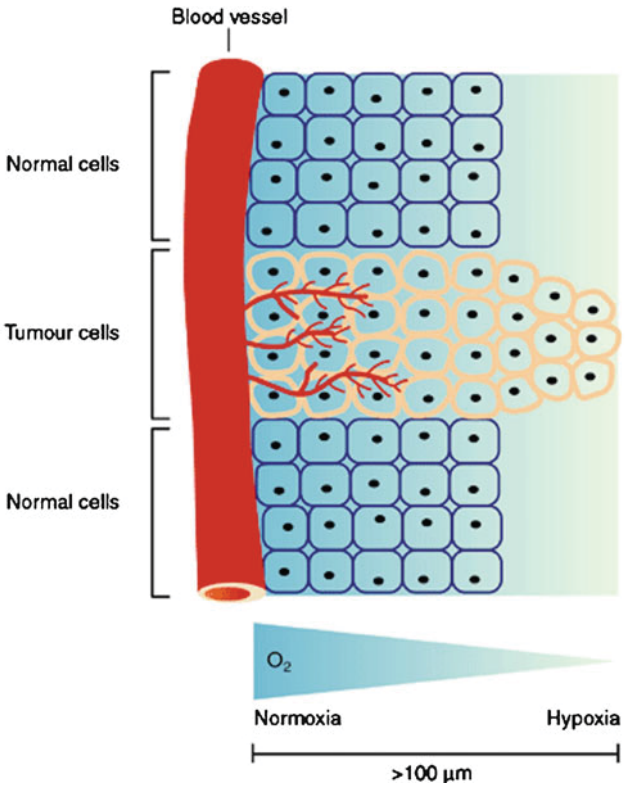

Fig. 3.15 Schematic representation showing the relative change in tissue oxygenation as a function of distance from the vascular system. At distances >100 µm, hypoxia begins to develop which stimulates further changes in tissue physiology. (From Carroll VA, Ashcroft M. Targeting the molecular basis for tumour hypoxia. Expert Rev Mol Med. 2005;7:1–16. © Cambridge Journals, published by Cambridge University Press, reproduced with permission)

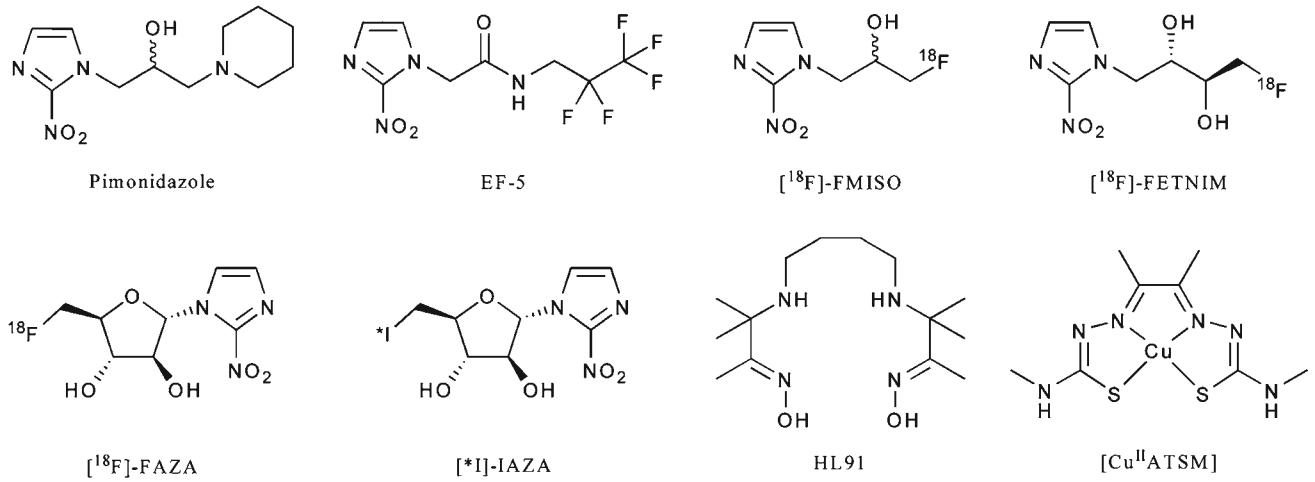

Fig. 3.16 Chemical structures of a range of compounds that have been explored in the design of hypoxia-selective radiotracers

carcinoma [129], but concerns remain over its ability to delineate hypoxia in other types of cancer, such as prostate cancer [130, 131]. The first human trials of [^{64}Cu^{II}ATSM] as a radiopharmaceutical for PET imaging of lung cancer were conducted in 2000 [132]. Later, in 2003, Dehdashti et al. demonstrated that in a sample of 14 patients with non-small-cell lung cancer (NSCLC), tumor uptake of [^{60}Cu^{II}ATSM] was predictive of patient response to radiotherapy [127]. PET images were acquired pre-therapy using both [^{18}F]FDG and [^{60}Cu^{II}ATSM] (Fig. 3.17) [127, 133]. Tumor uptake of [^{18}F]FDG was not significantly different between those patients who responded to therapy and nonresponders. Furthermore, [^{18}F]FDG uptake did not correlate with [^{60}Cu^{II}ATSM] uptake. Of the 14 patients, 8 responded to radiotherapy, with 5 making a complete recovery and 3 showing partial response. Patients who responded to therapy were found to have pre-therapy tumor-to-muscle (T/M) ratios for [^{60}Cu^{II}ATSM] uptake of 1.5 ± 0.4, whereas nonresponders showed much high tumor uptake, with T/M ratios of 3.4 ± 0.8. Interestingly, [^{64}Cu^{II}ATSM] has also been characterized as a potential hypoxia-selective agent for radiotherapy [134].

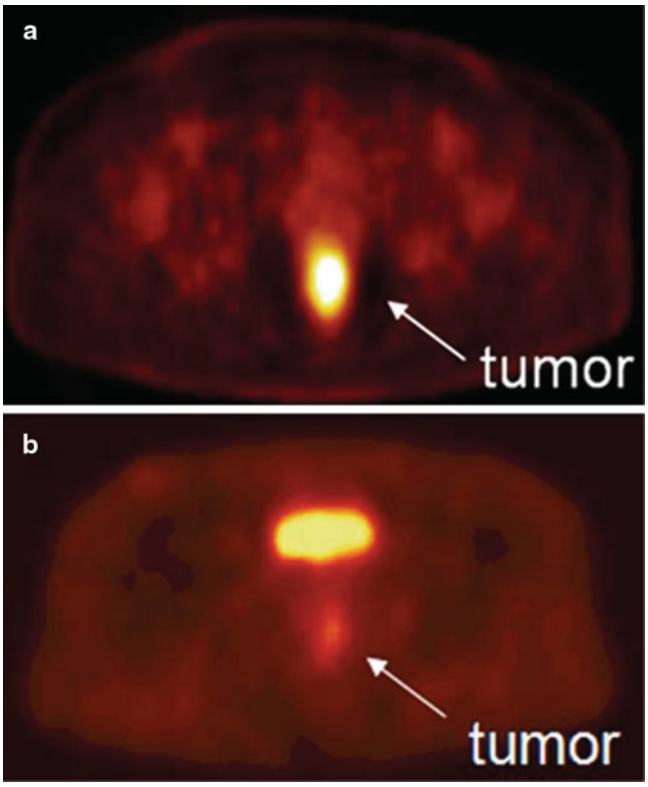

Fig. 3.17 (**a**) [^{60}Cu^{II}ATSM] PET scan showing a hypoxic tumor (tumor-to-muscle (T/M) uptake ratio = 3.1). The tumor has increased tracer uptake compared with surrounding tissues because the [^{60}Cu^{II}ATSM] is reduced and retained more avidly in hypoxic tissues. This tumor did not respond to neoadjuvant chemoradiation therapy. (**b**) [^{60}Cu^{II}ATSM] PET scan showing a normoxic tumor (T/M ratio = 2.3). This tumor responded to neoadjuvant chemoradiation therapy. The bright spot above the tumor is the bladder. (From Dietz DW, Dehdashti F, Grigsby PW, et al. Tumor hypoxia detected by positron emission tomography with ^{60}Cu-ATSM as a predictor of response and survival in patients undergoing neoadjuvant chemoradiotherapy for rectal carcinoma: a pilot study. Dis Colon Rectum 2008;51:1–8, with permission)

Imaging Cancer Biomarkers

While targeting the overall microenvironment of tumors is a promising strategy for cancer imaging, it is not the only option. Malignant tumors can often be discriminated from healthy tissues by differences present on the cellular level. These alterations often manifest themselves in the presence or overabundance of molecular biomarkers. These biomarkers are usually displayed on the cell surface and as such offer extremely attractive targets for radiotracers capable of avid, marker-specific binding. In addition, significant discrepancies in fundamental cellular processes—notably the metabolism of molecular building blocks—exist between cancerous cells and their normal counterparts, and these differences can also be exploited as targets for imaging. In the following pages, the targeting of these cellular differences by small molecules, peptides, and antibodies will be discussed.

Imaging Cancer Biomarkers with Small Molecules

Small molecules are organic moieties with median molecular weights of 450 Da and below [135]. Typically, these agents accumulate at their intended target sites through metabolic, transport-based, or receptor-mediated processes [136]. Examples of agents that follow each of these pathways are included in the following pages.

Hormone Receptors

Hormone receptors—most notably steroid, sigma, and folate receptors—are often overexpressed in breast and prostate tumors. Specifically, estrogen, progesterone, and androgen receptors are found in the cell nucleus, whereas sigma and folate receptors are membrane-bound [36, 137]. A number of receptor-targeted, small-molecule imaging agents have been developed to obtain both information about the location of the tumor and to assess the level and functional status of these receptors themselves. Several of these molecules labeled with radiohalogens, ^{99m}Tc, and ^{68}Ga have proved successful in animal models, but only a handful have been translated to the clinic (Table 3.6) [138, 139]. One of the most promising small-molecule imaging agents studied to date is 16α-^{18}F-fluoro-17β-estradiol (^{18}F-FES), a radiopharmaceutical employed most often in breast cancer (Fig. 3.18) [140, 141]. ^{18}F-FES has high estrogen receptor (ER) binding affinity and can be prepared in high specific activity [142]. Also, an improved automated radiosynthesis of ^{18}F-FES has

Table 3.6 Some small molecule imaging agents that have been tested in the clinic

Imaging agent	Imaging modality	Receptor target	Tumor type	No. of patients
Z-^{123}I-MIVE [276]	SPECT	Estrogen	Breast cancer	23
P-^{123}I-MBA [277]	SPECT	Sigma	Breast cancer	12
16β-^{18}F-βFMOX [278]	PET	Estrogen	Breast cancer	12
^{18}F-FES [145]	PET	Estrogen	Breast cancer	51
^{18}F-FES [279]	PET	Estrogen	Breast cancer	11
^{18}F-FES [280]	PET	Estrogen	Breast cancer	16
^{18}F-FES [281]	PET	Estrogen	Breast cancer	40
^{18}F-FES [282]	PET	Estrogen	Breast cancer	43
^{18}F-FES [283]	PET	Estrogen	Breast cancer	47
^{18}F-FDHT [284]	PET	Androgen	Prostate cancer	20
^{18}F-FDHT [148]	PET	Androgen	Prostate cancer	7
^{18}F-FDHT [149]	PET	Androgen	Prostate cancer	7

Source: http://www.clinicaltrials.gov. Accessed October 15, 2009

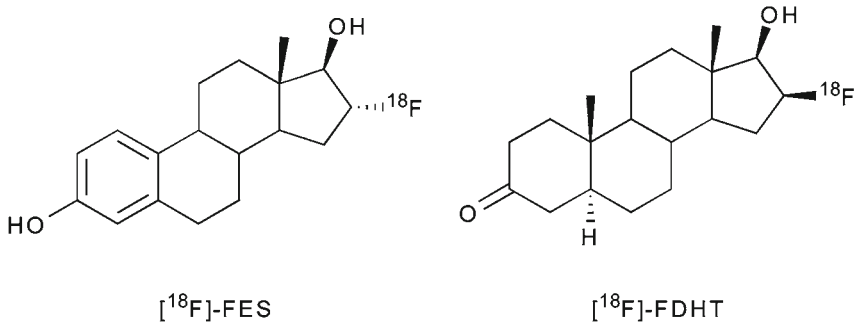

Fig. 3.18 Chemical structures of the steroid-based imaging agents ^{18}F-FES and ^{18}F-FDHT

been developed [143]. In a study of 13 breast cancer patients, ^{18}F-FES uptake was detected in primary breast carcinomas and generated PET images which correlated strongly with ER concentrations obtained by in vitro receptor binding assays ($R=0.96$) [144]. In another human study, ^{18}F-FES PET could be used as a predictive tool to assess patient response to hormone therapy [145]. Despite the clear clinical utility of ^{18}F-FES, it is still not considered an optimal tracer due to its facile reduction to give radioactive metabolites that recirculate in the blood. In an effort to remedy this issue, several analogs of ^{18}F-FES have also been synthesized by radiolabeling the parent molecule with ^{18}F at various positions (C-2, C-4, C-17) or adding a methoxy group at C-11 [142, 146, 147].

Another hormone-based radiopharmaceutical, 16β-^{18}F-dihydrotestosterone (^{18}F-FDHT), is currently under investigation as a prostate cancer imaging agent in humans (Fig. 3.18). ^{18}F-FDHT targets androgen receptors (AR) that are overexpressed by aggressive prostate tumors. In a clinical trial conducted at Memorial Sloan-Kettering Cancer Center (New York), seven patients showing signs of metastatic prostate cancer were subjected to ^{18}F-FDHT PET and [^{18}F]FDG-PET scans. Remarkably, the average SUV of multiple lesions for both scans were 5.28 and 5.22, respectively. Furthermore, two patients who received testosterone therapy showed markedly reduced ^{18}F-FDHT uptake at the tumor site [148]. Estimates of normal tissue radiation-absorbed dose from ^{18}F-FDHT administration were also obtained from the same patient base, and a recommended maximum administered activity of 331 MBq ^{18}F-FDHT was proposed [149].

Lipid Metabolism

In addition to upregulated glycolytic activity, tumors are also often characterized by perturbed lipid metabolism. Under normal conditions, the synthesis of triglycerides is the primary cellular mechanism for the long-term storage and transport of energy derived from carbohydrate metabolism. Cancer cells, however, do not maintain substantial energy stores and thus preferentially employ lipid metabolism pathways in the production of essential membrane phospholipids, such as phosphatidylcholine [150]. Consequently, overexpression of fatty acid synthase (FAS) and choline kinase (ChoK)—two enzymes essential for the production of phospholipids—are often seen in malignancies, including lung, colon, breast, ovarian, and prostate cancer [151]. FAS catalyzes the de novo synthesis of fatty acids from malonyl-CoA, a precursor

derived from acetic acid (Fig. 3.19) [152]. ChoK is responsible for the synthesis of phosphocholine, a product that eventually converges with the products of FAS activity in the synthesis of the phospholipid phosphatidylcholine.

Several PET radiotracers have been developed for imaging choline uptake and metabolism. Both ^{11}C and ^{18}F-labeled choline derivatives such as ^{18}F-choline and ^{18}F-fluoroethylcholine have been used to study tumor lipid metabolism (Fig. 3.20) [153–155]. The uptake of these radiotracers is extremely rapid and occurs within the first few minutes post-injection, permitting the use of short-lived radionuclides [153]. It was found that choline metabolism is not significant on this timescale, an observation that suggests that the accumulation of radiotracer is due to elevated rates of choline transport and not the activity of ChoK [156]. This hypothesis was supported by subsequent investigations with ^{18}F-deshydroxycholine, a choline analogue which is not phosphorylated by ChoK. In these experiments, the uptake of ^{18}F-deshydroxycholine closely resembled that of radiolabeled choline at early time-points (<10 min), but differences were more pronounced at later time-points, suggesting differences in irreversible cellular retention due to ChoK activity [157].

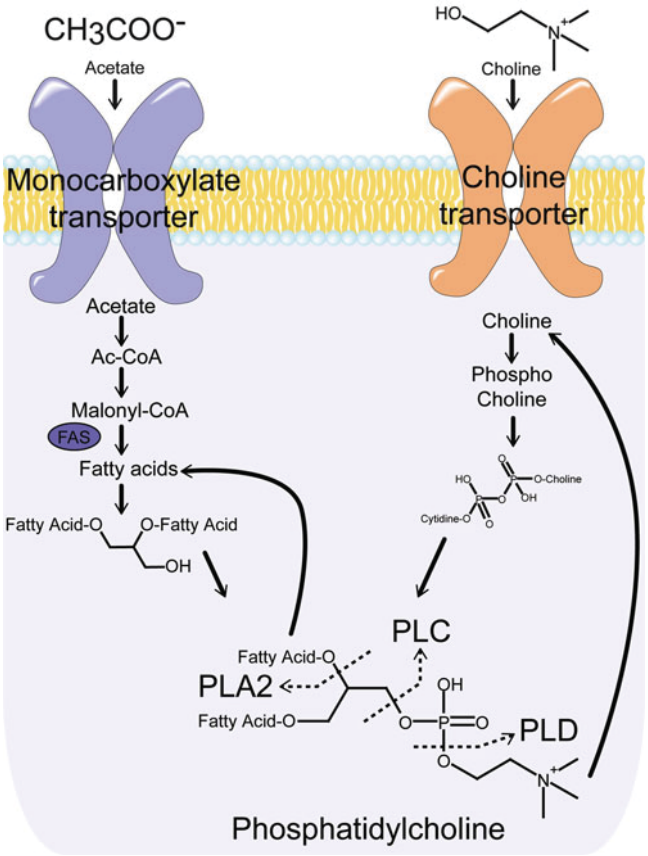

Fig. 3.19 The transport and metabolic pathways for acetate and choline converge on phosphatidylcholine

Another radiotracer, [^{11}C]acetate, has also been employed to image lipid metabolism in tumors [158]. In tissues with active oxidative phosphorylation (e.g., myocardial tissue), [^{11}C]acetate is funneled into the Krebs cycle, and within minutes after intravenous injection, the tracer is metabolized and released as [^{11}C]CO_2. In tumors, however, the rate of oxidative metabolism is reduced. In this case, [^{11}C]acetate accumulates steadily within the malignant tissue [159], indicating the prominent use of acetate in the synthesis of fatty acids and lipids. Indeed, direct correlation between [^{11}C]acetate uptake and FAS expression in tumors was observed in animal models [160]. It is unlikely, though, that lipid synthesis is the only reason for the rapid uptake of acetate, as the use of FAS inhibitors failed to completely suppress radiotracer uptake [160].

PET imaging of lipid metabolism is most often used as a diagnostic tool in prostate, breast, and brain tumors (Fig. 3.21) [161]. In prostate cancer imaging, for example, choline-based PET radiotracers offer several important advantages over conventional [^{18}F]FDG-PET, which can often give false-negative results due to the low metabolic rates of prostate tumors [162]. For instance, in comparison to [^{18}F]FDG, the activity of [^{11}C]choline—and, to a lesser extent, ^{18}F-choline—in urine is dramatically reduced, leading to decreased background from bladder activity, allowing better delineation of tumors in the pelvic region [154]. In practice, however, the apparent advantages of [^{11}C]choline versus [^{18}F]FDG-PET imaging for staging prostate cancer have not been widely accepted due to weak correlations with the

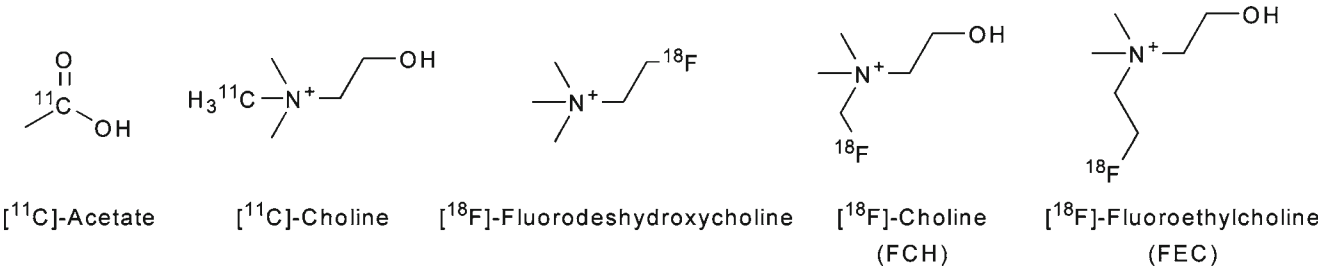

Fig. 3.20 PET tracers for studying tumor lipid metabolism

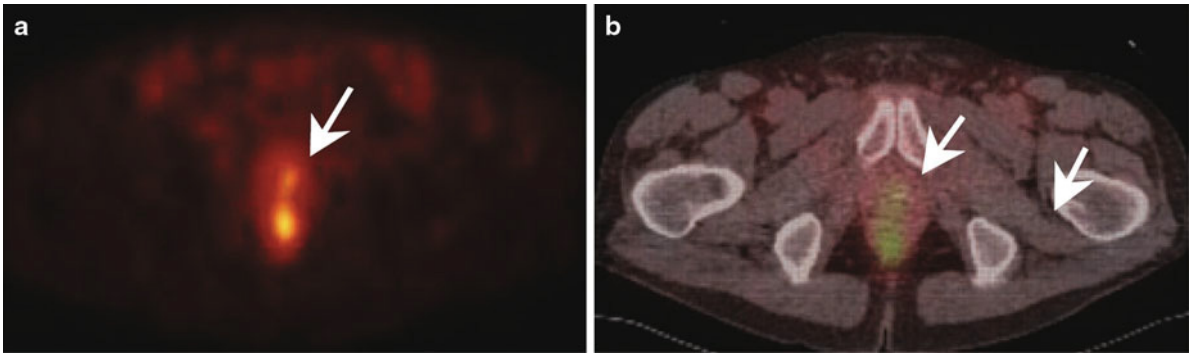

Fig. 3.21 An example of a [^{11}C]acetate PET scan showing (**a**) focal hyperactivity in the prostate bed and (**b**) the fused imaging with the corresponding CT. Note the small, focal hyperactivity (*arrows*)

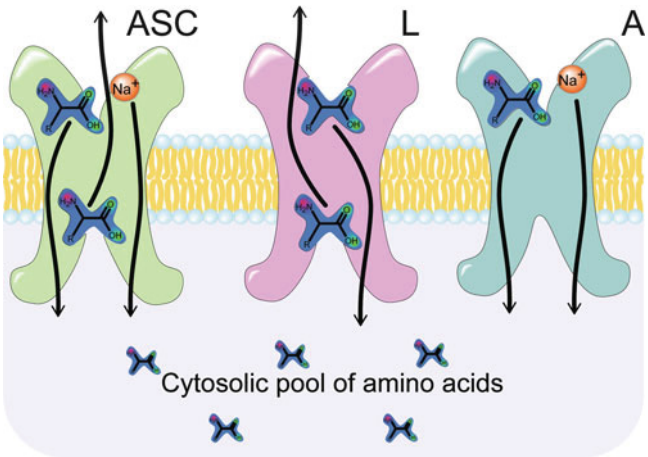

Fig. 3.22 Principal mechanisms of the amino acid transport. ASC transporters move one molecule of amino acid and Na^+ ion inside the cell for each amino acid moved outside the cell (sodium dependent, active transport). L transporters move one amino acid inside the cell for every one amino acid moved outside the cell (passive transport along the concentration gradient). A transporters move one amino acid inside the cell along with one Na^+ ion (sodium dependent, active transport)

Gleason scoring method [163]. In addition, newly diagnosed prostate cancer shows a strong inverse correlation between antihormonal therapy and choline uptake; [163] after radical prostatectomy or radiotherapy, this correlation becomes less apparent [164]. Further examples of the use of radiotracers in prostate imaging can be found in Chap. 21.

Amino Acid Transport

Amino acids are too polar for passive diffusion through the cell membrane, and as such, mammalian cells have developed a set of specialized transporters for the uptake of these important building blocks. Thirteen major amino acid transporters have been identified to date, and these can be subdivided into two groups: sodium-dependent (ASC and A) and sodium-independent (L) transporters (Fig. 3.22) [165]. The activity of the ASC- and A-type transporters depends on the transmembrane sodium gradient, with the enzymes transporting sodium ions along with their amino acid cargo. In contrast, L-type transporters act by exchanging one amino acid for another and are thus free of any sodium dependence. Regardless of their mechanism, amino acid transporters are ubiquitous in many proliferating tissues [166], and tumors often exhibit dramatically elevated levels of expression compared with normal tissue [167]. Indeed, the production of both the A and L families of transporters has been found to be upregulated in certain cancer cell lines. The activity of A-type transporters has shown a positive correlation with cell growth in many cell types, including virally transduced cells [168]. Likewise, histological data on L-transporter expression was found to correlate with poor prognosis in patients with gliomas [169] and transitional cell carcinomas [170].

Given these correlations, a number of PET radiotracers have been developed to probe the expression of amino acid transporters in tumors (Fig. 3.23). The small size of these molecules and rapid kinetics favors the use of short-lived isotopes, and thus most studies have been conducted using ^{11}C and ^{18}F. The short half-life of these radionuclides is actually beneficial, because imaging at early time-points reduces the contribution of catabolic and anabolic pathways to the background activity [171]. This idea was reinforced by a comparison between the in vivo behavior of the radiotracers and their analogs modified to preclude biological transformations [172]. A recent review by Plathow et al. provides a comprehensive overview of radiolabeled amino acids for PET imaging [173].

One radiolabeled nonnatural amino acid—[^{11}C]methylaminoisobutyric acid, commonly known as [^{11}C]MeAIB—has been shown to be a specific agent for imaging the activity of A transporters [174]. Despite uptake in various normal tissues, including the salivary glands and pancreas [175], [^{11}C]MeAIB was found to accumulate in lymphomas and head and neck malignancies with low renal excretion [176].

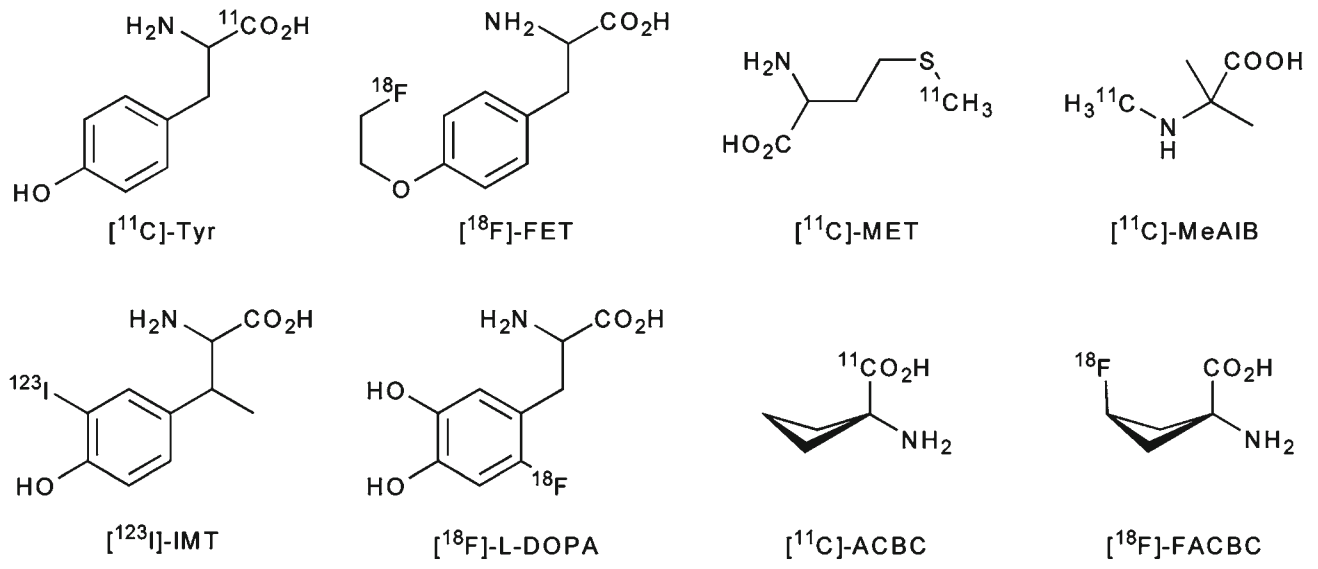

Fig. 3.23 PET and SPECT radiotracers based on the amino acids: L-[^{11}C]-Tyr, L-[^{123}I]-IMT, L-[^{18}F]-FET, [^{18}F]-L-DOPA, [^{11}C]-MET, [^{11}C]-MeAIB, [^{11}C]-ACBC, and [^{18}F]-FACBC

In contrast, the possibility of a specific radiotracer for L transporter activity is precluded by the broad range of amino acids translocated by these proteins. L transporters have been identified as the main conduits by which L-(methyl-[^{11}C])-methionine ([^{11}C]MET) [177], radiolabeled tyrosine/phenylalanine analogs [178], 1-aminocyclobutane-1-[^{11}C] carboxylic acid ([^{11}C]ACBC), and 1-amino-3-^{18}Ffluorocyclobutylcarboxylic acid (^{18}F-FACBC) [179] accumulate in cells. The lack of specificity of the L transporters is thought to be responsible for the similarities observed in the biodistribution profiles of radiolabeled methionine analogues with tyrosine analogs ^{123}I-α-methyl-L-tyrosine (^{123}I-IMT) [180] and 3,4-dihydroxy-6-[^{18}F]fluoro-L-phenylalanine ([^{18}F] L-DOPA) [172].

In the clinic, radiolabeled amino acid analogues show high background uptake in the liver, pancreas, and intestines [181], and tissues which are infected or inflamed often display high accumulation of activity [182]. With the exception of [^{11}C]MET [183] and ^{18}F-FACBC [184], which have both been employed in the delineation of prostate cancer, amino acid radiotracers have had limited clinical impact in cancers of the ventral cavity, primarily because their uptake and sensitivity is less favorable than that of [^{18}F]FDG [185]. However, amino acid radiotracers have found widespread application in brain tumor imaging. This is primarily due to the limitations of [^{18}F]FDG-PET in brain imaging: glucose metabolism of the brain is persistently high, resulting in high cerebral uptake of [^{18}F]FDG and low tumor-to-background ratios (vide supra) [186]. A comparison of [^{11}C]MET with [^{18}F]FDG uptake in glioblastoma clearly demonstrates the efficacy of using amino acid-based radiotracers in neurological cancer imaging (Fig. 3.24) [187].

High-resolution PET imaging of the brain with amino acid radiotracers is also used to direct stereotactic and intensity-modulated radiotherapy, a technique with high spatial accuracy of irradiation. For maximum efficacy, these new radiation treatment methods require the accurate delineation of tumor borders. Contrast-enhanced CT or MRI is frequently used to delineate gross tumor volume of high-grade tumors but has had only limited success in brain tumors [188]. As an alternative to CT, [^{11}C]MET PET can be used to improve accuracy in defining the boundaries of brain malignancies [189]. This observation has been confirmed in a series of studies correlating amino acid PET with stereotactic biopsies [190]. Similarly, the addition of O-(2-^{18}F-fluoroethyl)-L-tyrosine (^{18}F-FET) PET data to an MRI study improved the specificity of tumor delineation from ~50 to ~90% [191]. The efficiency of PET for accurately marking high-grade gliomas for further intervention has been illustrated in a group of 44 glioma patients [192]. For patients whose treatment plan was based solely on MRI or CT, median overall survival did not exceed 5 months; the addition of amino acid PET imaging to the protocol increased median survival to 9 months.

Nucleic Acid Metabolism

While increased glycolytic activity is not tumor specific and may be caused by other conditions such as inflammation, increased cellular proliferation is a specific characteristic of tumors and thus is an attractive target for the molecular

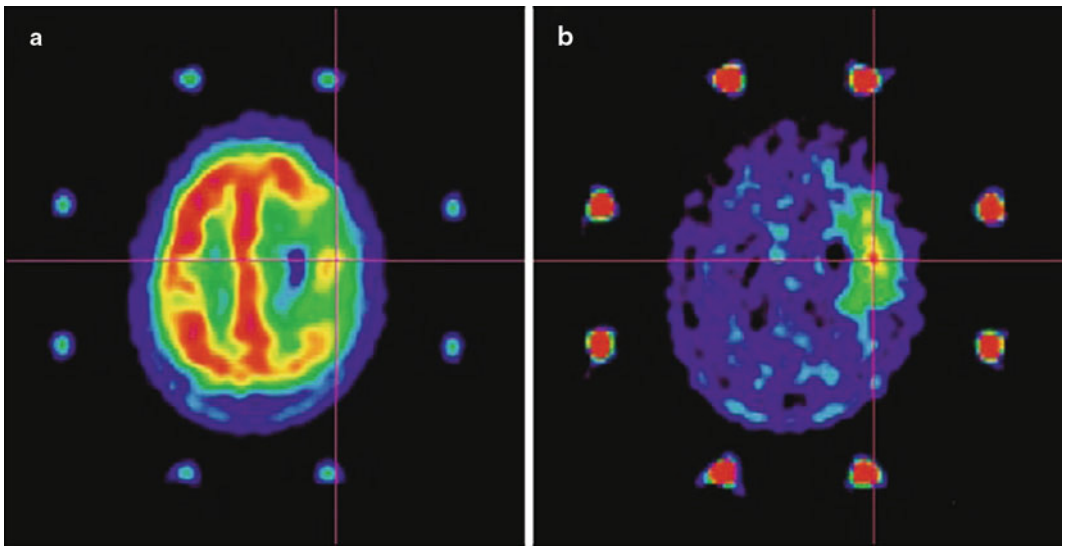

Fig. 3.24 PET [^{18}F]FDG (**a**) and [^{11}C]MET (**b**) of a 62-year-old woman with a glioblastoma in the right prerolandic cortical area. Uptake of [^{18}F]FDG was reduced in the tumor area except for one spot of uptake equivalent to that in the surrounding gray matter. Uptake of [^{11}C]MET was markedly higher in the tumor than in the cortex. When PET images obtained with the two tracers were co-registered, the highest focus of [^{11}C]MET uptake corresponded to the spot of highest [^{18}F]FDG intensity (crosshairs). (From Pirotte B, Goldman S, Massager N, et al. Comparison of [^{18}F]FDG and ^{11}C-methionine for PET-guided stereotactic brain biopsy of gliomas. J Nucl Med. 2004;45:1293–8. Reprinted with permission of the Society of Nuclear Medicine)

imaging of cancer [140, 193, 194]. Indeed, two hallmarks of cellular proliferation—nucleic acid metabolism and DNA synthesis—are especially promising targets for the design of imaging agents [195, 196]. In particular, the de novo synthesis and salvage pathways of thymidine (TdR, the only nucleoside employed in DNA and not RNA) have attracted significant attention. The de novo synthesis pathway is generally less favored for radiotracer development because it involves precursors—such as deoxyuridine, uridine, and uracil—which are incorporated not only into DNA but also RNA. In contrast, the thymidine salvage pathway has been the focus of enthusiastic radiotracer development. Indeed, [^{3}H]TdR was the first radiolabeled thymidine molecule introduced in the 1950s. This paved the way for the development of [^{11}C]methyl-thymidine ([^{11}C]TdR) as the first PET imaging agent to successfully measure proliferative activity in tumors (Fig. 3.25) [197, 198].

[^{11}C]TdR suffers from rapid catabolism upon injection [199], and because of the short half-life of ^{11}C, several alternate TdR-based PET radiotracers—including 3′-deoxy-3′-^{18}F-fluorothymidine (^{18}F-FLT), 5-methyl-(2-^{18}F-fluoro-2-β-D-arabinofuranosyl)uracil (^{18}F-FMAU), and 5-^{76}Br-bromo-(2-fluoro-2-β-D-arabinofuranosyl)uracil (^{76}Br-FBAU)—have been developed. In practice, ^{18}F is preferable to ^{11}C because the longer half-life of ^{18}F ($t_{1/2}$ = 109.7 min) is more useful in the clinical setting and facilitates off-site production of radiotracers. Indeed, ^{18}F-FLT and ^{18}F-FMAU

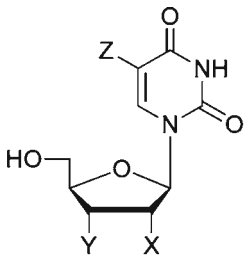

Substrate	X	Y	Z
TdR	H	OH	CH_3
[^{11}C]-TdR	H	OH	$^{11}CH_3$
[^{18}F]-FLT	H	^{18}F	CH_3
[^{18}F]-FMAU	^{18}F	OH	CH_3
[^{76}Br]-FBAU	F	OH	^{76}Br

Fig. 3.25 Thymidine-based PET radiotracers: [^{11}C]TdR, ^{18}F-FLT, ^{18}F-FMAU, and ^{76}Br-FBAU

are the most extensively studied TdR analogs to date and have proven successful in clinical trials [198].

^{18}F-radiolabeling at the 3′ and 2′ positions of the ribose in ^{18}F-FLT and ^{18}F-FMAU, respectively, provides enhanced stability with respect to TdR degradation [194]. Once transported into the cell, both of these agents interact with different subtypes of thymidine kinase (TK), an essential enzyme in the thymidine salvage pathway. ^{18}F-FLT is phosphorylated by

TK-1 to give the monophosphate form, ^{18}F-FLT-MP, while ^{18}F-FMAU is phosphorylated mainly by TK-2 to yield ^{18}F-FMAU-MP. Subsequent additional phosphorylation of each TdR analog produces di- and triphosphate species (^{18}F-TdR-DP, ^{18}F-TdR-TP) which are very hydrophilic and thus unable to diffuse through the cell membrane [200]. These phosphorylated agents thus become irreversibly trapped in the cell, and the accumulation of activity over time correlates with cellular proliferation. Therefore, PET imaging with ^{18}F-FLT and ^{18}F-FMAU has been used clinically to monitor the antiproliferative effects of chemo- and radiotherapy. One key difference between the tracers is their ultimate fate. ^{18}F-FLT is not incorporated into DNA; however, it provides specific biologic information about TK-1 activity, cell cycle progression, and tissue proliferation. In contrast, ^{18}F-FMAU is incorporated into mitochondrial DNA, because the presence of the hydroxyl group on 3′ position of the sugar ring is essential for this process. Therefore, ^{18}F-FMAU can be used as a radiotracer for measuring the index of mitochondrial mass [201].

Imaging Cancer Biomarkers with Peptides

Small molecules are not the only constructs employed as radiopharmaceuticals. Peptides, chains of amino acids up to several dozen units long, also hold a significant position in the field of radiotracer development. Indeed, a number of receptors that bind peptide ligands are also known to be overproduced in tumors and therefore represent promising candidates for imaging. One class of proteins, the G-coupled receptors, are particularly important in this regard. The G-coupled receptors comprise a large class of proteins responsible for sensing extracellular peptide signals and relaying these signals to cellular components in the cytosol. Several families of G-coupled receptors have been found to be overexpressed in tumors, and a number of strategies for targeting this class of receptors with radiolabeled peptides have been developed.

It is important to note that both agonist and antagonist peptides can be employed as peptide-based imaging agents. It was long believed that the internalization of agonist:receptor complexes was responsible for the accumulation of the peptides in cells, a supposition which led to the development of agonist radiotracers. However, several examples of probes based on antagonist peptides have emerged, casting doubt on the aforementioned internalization hypothesis. In many cases, the success of antagonist imaging agents can best be explained by the very slow dissociation of these ligands from their receptors, as well as increases in the number of accessible binding sites per cell for antagonists as compared to their agonist analogs. The potential applicability of antagonistic peptide ligands as receptor-targeted radiopharmaceuticals has had particular impact on systems in which agonist binding stimulates tumor growth, namely gastrin-releasing peptide (GRP), cholecystokinin, neurotensin, vasoactive intestinal peptide, and neuropeptide Y receptors [202].

Design

Conceptually, the core design of G-protein targeting agents is straightforward. Nature has designed regulatory peptides to bind tightly and selectively to their receptors. Therefore, simply radiolabeling a receptor-specific peptide stands as a promising route to an effective radiopharmaceutical. However, experience has revealed that the development of peptide radioimaging probes is far more complicated; of the hundreds of proposed agents, less than a dozen have been translated.

One of the most important limitations in the use of short peptides for imaging is the influence that the radiolabel can have on the structure and binding properties of the peptide. Ligands for G-coupled receptors are usually relatively small peptides (1–5 kDa) suitable for solid-phase peptide synthesis. These peptides are intermediate in size between antibodies (~150 kDa) and small molecules (<1 kDa), and their pharmacokinetic properties reflect this standing. The average rate of accumulation of small peptides in target tissue is on the timescale of a few hours, squarely between that of small molecules and antibodies.

From a chemical standpoint, the intermediate size of peptides presents both challenges and benefits. As is the case with many small molecules, particular care must be paid to the position of the radiolabel, for modest changes in the molecular structure of the peptide can have dramatic effects on the solubility, binding properties, and secondary and tertiary structure of the agent. Almost inevitably, the radiolabeling of a peptide will result in some pronounced alterations in the physicochemical behavior in vivo of the radiolabeled peptide compared to the precursor molecule. However, prudent design can ensure that these alterations will not involve the binding of the peptide to its target site.

On the other hand, the intermediate size of peptides facilitates the use of most common organic transformations for radiotracer development. Further, automated peptide synthesis and functional group modification chemistry are well-developed techniques which facilitate the fine-tuning of peptide-based agents via structure–activity investigations. Such facile modularity is rarely, if ever, available in small molecules or antibodies.

Radiochemistry

The specific activity of peptide-based radiopharmaceuticals can play an important role in the success of receptor imaging. Common tools available in radiochemical laboratories typically allow for the preparation of high specific activity, no-carrier-added formulations of radiopeptide, which enable injection of a minimal molar amount of tracer for imaging applications [203]. Unwanted effects in vivo, such as receptor saturation in target tissues or pharmacological actions of the

peptide, can be minimized under these conditions. However, the radiolabeling of peptides using commercial kits often leads to carrier-added radiopharmaceutical preparations. For example, in the case of ^{111}In-DTPA-octreotide, more than 90% of the peptide mass administered with the radiopeptide is unlabeled. In this case the presence of carrier is not a problem, because octreotide analogs act as inhibitors of tumor growth [202]. However, the pharmacological effects of low specific-activity radiopeptides become a serious concern in the case of agonists derived from peptides such as bombesin, gastrin, cholecystokinin, or neurotensin, all of which have been shown to stimulate tumor growth in vivo [202]. Indeed, the typical peptide dose administered for somatostatin (SST)-receptor imaging (e.g., 10–20 μg) can result in unwanted pharmacological side effects with some of the aforementioned peptides.

Stability

The lack of stability of radiolabeled peptides in vivo is another important issue which, at present, represents a limitation to the clinical translation of many promising radiotracers. Radiotracers derived from small regulatory peptides—for example, SST-14 or SST-28, bombesin, GRP, and neurotensin—often have short biological half-lives. From an imaging perspective, a short biological half-life does not allow for the accumulation of high amounts of radioactivity in malignant tissue. Therefore, increasing the in vivo stability of these peptides without concomitantly decreasing their binding affinity is a primary focus in the development of these agents. In many cases, standard chemical modifications, such as truncation of the peptide sequence, can often increase in vivo stability. Alternatively, the introduction of nonnatural amino acids that mimic the chemical properties of their natural counterparts can often prevent the recognition of cleavage sites by peptidase enzymes. Further, the cyclization of peptide sequences in imaging agents can protect the peptide from interaction with proteolytic enzymes capable of degrading the sequence from the chain terminus. Other modifications to enhance stability include alkylation or reduction of the peptide amide groups to amines, as well as amidation and acylation of peptide termini [204]. As the result of these techniques, the radiolabeled peptides currently proposed for clinical use show plasma half-lives on the scale of hours [205].

Tumor Accumulation and Renal Clearance

In the case of peptide-based agents, tumor accumulation is mainly a function of receptor-binding affinity, expression levels, and in the case of agonists, ligand internalization rates. Background levels, on the other hand, depend primarily on tracer excretion, and for peptide radiotracers, the overall excretion pattern is determined by the physiological receptor expression profile, the metabolic behavior of the agent, and its physicochemical characteristics (e.g., lipophilicity, net charge, and charge distribution). Several factors play important roles in determining the excretion and clearance kinetics of a given peptide radiotracer: primary amino acid sequence, radiolabeling chemistry, chelate stability, and presence of functional group modifiers. The relationship between each of these and excretion and clearance is described below.

Peptide Sequence. Quite simply, an increase in the lipophilicity of the amino acids in a given radiopeptide increases hepatobiliary clearance.

Radiolabeling Chemistry. Interestingly, the identity of the radiometal attached to a peptide can have a significant influence on its biodistribution. For example, substituting ^{111}In with ^{68}Ga in DOTA-TOC led to a more than twofold enhanced tumor uptake (predominantly due to increased receptor affinity) and reduced renal accumulation, which has been explained by an alternative coordination mode for the Ga^{3+} complex [206].

Chelate Stability. DOTA, NOTA, and CB-TE2A have been coupled to the bombesin analog Aoc-BN(7-14) (see Fig. 3.8). A comparative evaluation in a PC-3 tumor model showed decreased hepatic and renal uptake of the NOTA compared to the DOTA analog, while tumor accumulation remained unchanged [207]. Furthermore, the CB-TE2A-derivative showed improved clearance from nontarget tissues and higher tumor/background ratios than the DOTA peptide. These observations were attributed to an increased in vivo stability of the respective ^{64}Cu-NOTA and ^{64}Cu-CB-TE2A chelates with respect to demetallation. Further, changing the chelator for ^{111}In in Tyr3-octreotide from DTPA to DOTA resulted in slightly increased tumor accumulation but also significantly higher renal tracer uptake [208].

Presence of Modifiers. Pharmacokinetic modifiers such as carbohydrates [209, 210] or polyethylene glycol (PEG) chains of varying length [211] have been introduced successfully to reduce tracer lipophilicity and thus to induce a shift toward predominantly renal tracer excretion without compromising binding affinity. In the case of radiometallated octreotide analogs, for example, the introduction of spacers of various natures (Asp, Lys, uncharged amino acids, PEG, carbohydrates [212]) is generally well tolerated and, in some cases, can lead to improved pharmacokinetics. The same applies to RGD peptides [213] but not to bombesin analogs. The insertion of uncharged aliphatic or aromatic spacers [214] between the chelator and the peptide core allows the fine-tuning of tumor accumulation versus tracer excretion, whereas the introduction of charged amino acids leads to a complete loss of binding affinity [215].

Diagnostic Radioimaging

Three examples of peptide-based imaging agents—SST analogs, integrin binding peptides (see *Angiogenesis* section),

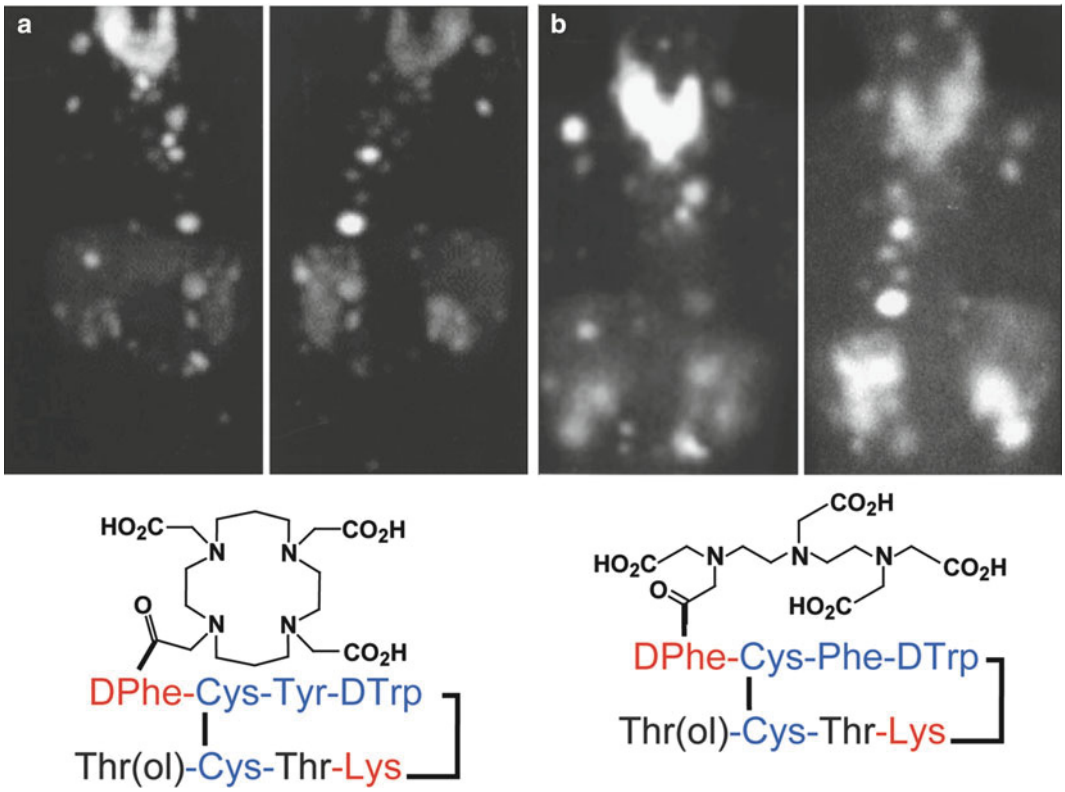

Fig. 3.26 Anterior and posterior PET (SPECT) images throughout the neck, chest, and abdomen of a 45-year-old man with numerous metastatic foci of carcinoid tumor. Images were obtained 4 h after injection. Structure of PET imaging agents: (**a**) ^{64}Cu-TETA-OC (**b**) ^{111}In-DTPA-OC. (From Shi W, et al. Localization of neuroendocrine tumors with [^{111}In] DTPA-octreotide scintigraphy (Octreoscan): a comparative study with CT and MR imaging. QJM 1998;91: 295–301, by permission of Oxford University Press)

and GRPs—illustrate both the current success and future potential of cancer imaging with these promising radiopharmaceuticals.

SST is a hormone produced by neuroendocrine neurons in the brain and by paracrine cells in the GI tract. SST regulates release of growth hormone, glucagon, insulin, thyroid-stimulating hormone, and gastrin among others. SST receptors are overexpressed in prostate carcinomas, sarcomas, neuroblastomas, meningiomas, breast carcinomas, lymphomas, small-cell lung cancers, and inactive pituitary adenomas. Imaging agents based on analogs of this peptide were the first receptor-targeting peptides approved for clinical use. The success of octreotide, the first in a long line of SST analogs, portended the vigorous development of the field (Figs. 3.26 and 3.27). A detailed description of imaging with SST analogs can be found in recent reviews [216]. It has been noted that high levels of SST receptor expression are also known to occur in the human spleen and kidney, central nervous system, hypothalamo-pituitary system, and gastrointestinal system; fortunately, however, this expression does not dramatically affect imaging. It has been demonstrated that the uptake of ^{111}In-DTPA-octreotide in these organs was significantly reduced in patients receiving treatment with unlabeled octreotide (uptake in kidney and spleen, respectively, was diminished to 85 and 31 % of control), while surprisingly, tumor uptake remained unaffected [217].

GRP receptors are a family of receptors involved in the regulation of muscle contraction, immune functions, body temperature, and cardiac rhythm. Activation of these receptors has been shown to initiate and promote the growth of lung, breast, pancreatic, and prostate tumors. It has been determined, however, that peptides other than GRP bind to the receptors of this family. The most important of these is bombesin, originally isolated from South American frogs. Since its discovery, several radiolabeled derivatives of bombesin have been investigated as radiotracers in humans, including ^{68}Ga-BZH3 (Fig. 3.28). Notably, ^{68}Ga-BZH3 posses several features aimed at improving its in vivo stability, including the introduction of the nonnatural amino acids D-tyrosine (DTyr), norleucine (Nle), and thienylcarbonylornithine (Thi) to eliminate recognition sites used by proteinases and the amidation of the C terminus to likewise increase proteolytic stability. Moreover, the pharmacokinetic profile of the agent is improved by the addition of an uncharged, hydrophilic PEG linker that confers increased hydrophilicity to the construct.

Fig. 3.27 (*Top*) ^{68}Ga-DOTA-TOC PET scan of a 56-year-old woman with multiple liver and lymph node metastases. (*Bottom*) Structure of DOTA-TOC. (From Gabriel M, Decristoforo C, Kendler D, et al. ^{68}Ga-GOTA-Tyr3-octreotide PET in neuroendocrine tumors: comparison with somatostatin receptor scintigraphy and CT. J Nucl Med. 2007;48:508–18. Reprinted with permission of the Society of Nuclear Medicine)

Imaging Cancer Biomarkers with Proteins: Apoptosis

The imaging of apoptosis provides a particularly interesting case study in the development of a radiopharmaceutical that lies in the middle ground between short peptides and antibodies.

Apoptosis is a process of regulated or programmed cell death. During apoptosis, the mitochondria and ribosomes of the cells affected often remain intact, and surrounding cells internalize them along with the other components of the post-apoptotic cell. Necrotic cells, in contrast, lose membrane integrity, swell, and then lose their contents to the surrounding tissue, causing inflammation and initiating an immune response. On the cellular level, apoptosis is carried out by a group of Cys-Asp-specific proteases known as *caspases* (Fig. 3.29). Caspases are usually subdivided into two groups: initiator caspases (numbered 8–10) and executioner caspases (3, 6, and 7) [218]. Activation of the initiator caspases can occur via external stimuli (e.g., binding of tumor necrosis factor) or intrinsic mitochondrial pathways (e.g., release of cytochrome from the mitochondria), and these initiators in turn proceed to engage the executioner caspases via proteolytic activation. The activation of these executioner caspases results both in the orderly breakdown of cellular proteins, including the cytoskeleton and nuclear matrix, and the activation of poly-ADP-ribose polymerase (PARP), an enzyme responsible for the degradation of nuclear DNA. Combined, these processes are termed the "execution phase." From a targeting standpoint, the most interesting feature of the execution phase is the exposure of phosphatidylserine (PS) on the cell surface [219]. This membrane component is normally restricted to the inner surface (inner leaflet) of the lipid bilayer; however, during apoptosis, the mechanisms that maintain membrane asymmetry are deactivated, and PS becomes distributed on the outer membrane. Indeed, even stressed—but not necessarily apoptotic—cells have been shown to express low levels of PS on the surface of their outer membrane [220].

Surface-exposed PS provides a convenient handle for discriminating apoptotic cells from healthy cells. Annexin V (molecular weight ~36 kDa) is a large, well-studied protein that interferes with the immunosuppressive mechanisms of apoptotic and necrotic cells and is distributed widely in the human body. [221, 222] Complete functional details of the annexin V pathway have yet to be elucidated, but a variety of evidence suggests that annexin V acts as a naturally occurring ligand specific for PS, capable of binding the cell-surface marker and thereby preventing apoptotic cells from suppressing the immune response. From a radiochemical point of view, annexin presents somewhat of a unique challenge. The macromolecule is certainly not an antibody, yet it is far too large to be treated as a short peptide. Thus, the strategies for the design and development of annexin for use as a radiopharmaceutical must necessarily lie in between those employed for peptides and those utilized for antibodies.

Radiolabeled annexin V was proposed for imaging apoptosis in cancer [223]. The earliest methods for labeling annexin V involved the modification of the intact protein with ^{99m}Tc via bifunctional N_2S_2 chelation. In a study of 15 patients with late-stage lung cancers, lymphomas, and metastatic breast cancers, annexin V SPECT was performed before chemotherapy (48 and 24 h prior to treatment) and immediately after the first course of treatment (day +1 and day +2) [224]. Out of eight patients with unchanged uptake, six were nonresponders to paclitaxel-based chemotherapy. Better correlations were found for the patients responding to the chemotherapy; all seven patients exhibited elevated uptake of the tracer in the tumor after the therapy.

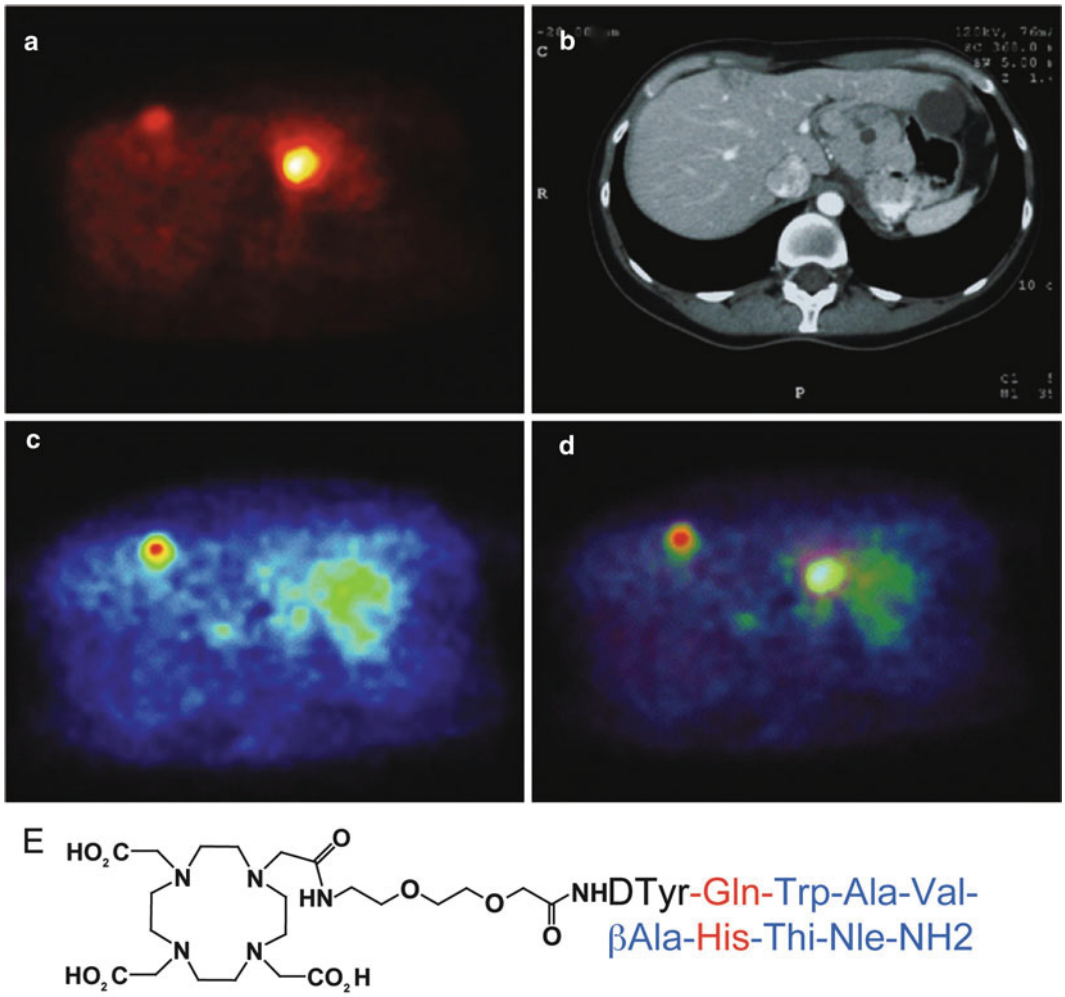

Fig. 3.28 Transaxial images of a patient with stomach tumor and liver metastasis. (**a**) [^{18}F]FDG image: two hypermetabolic areas, one in ventral part of right liver lobe and another in stomach. (**b**) CT image at same level demonstrates the two hypodense lesions in stomach and liver. (**c**) ^{68}Ga-BZH3 image at level of CT image demonstrates enhanced uptake in liver lesion and only slight diffuse enhancement in stomach. (**d**) Fused image of [^{18}F]FDG and ^{68}Ga-BZH3. (**e**) Structure of BZH3. (From Dimitrakopoulou-Strauss A, Hohenberger P, Haberkorn U, et al. ^{68}Ga-labeled bombesin studies in patients with gastrointestinal stromal tumors: comparison with [^{18}F]FDG. J Nucl Med. 2007;48:1245–1250. Reprinted with permission of the Society of Nuclear Medicine)

The N_2S_2 labeling method, however, is complex and results in unstable complexes. Even the simplified kit contains 11 components, and the preparation of the tracer involves a series of lengthy reaction steps using different conditions. The purification of the final material is also nontrivial. Consequently, the implementation of the bifunctional agent hydrazinonicotinamide (HYNIC) has allowed for simplified tracer preparation [225]. ^{99m}Tc-HYNIC-annexin shows no bowel excretion, thus facilitating imaging in the abdominal region; however, this agent concentrates in the cortex of the kidney, limiting visualization of any paranephric structures [226].

Like its predecessors, ^{99m}Tc-HYNIC-annexin has been employed for monitoring the efficacy of chemotherapy in cancer patients [227]. For patients with late-stage lung cancer (both small-cell lung cancer and non-small-cell lung cancer) [228], a single scan 24 h after the start of treatment may be sufficient to determine which patients have at least partial response to platinum-based chemotherapy; a low-level baseline uptake of the radiotracer has been observed in patients who later showed response to the therapy. Two possible explanations exist: either tumors with high natural levels of apoptosis are more susceptible to chemotherapy or increased expression of PS on endothelial cells of tumor vasculature is

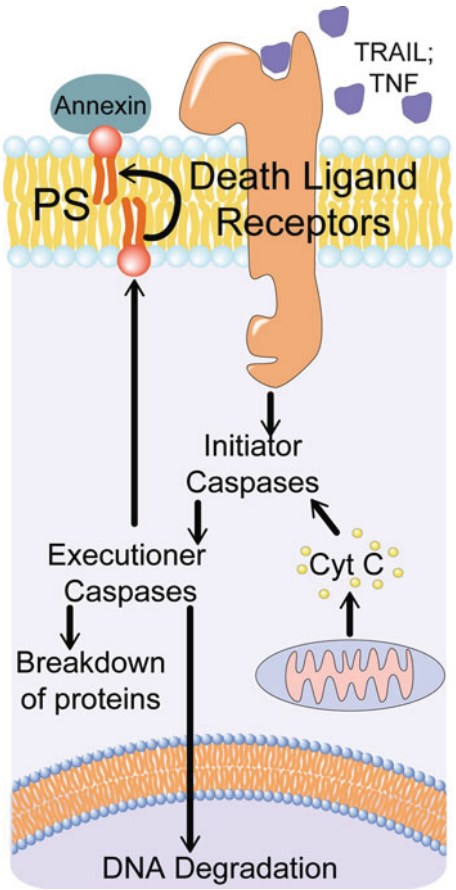

Fig. 3.29 Interconnection of apoptotic events. Two major pathways trigger apoptosis: external (via death receptors) and internal (via release of cytochrome C from the mitochondria). Inhibition of floppase and activation of scramblase lead to the exposure of PS on outer leaflet of the membrane; annexin can then bind PS

a feature indicative of the later success of chemotherapy [229]. Figure 3.30 provides examples of the images obtained with ^{99m}Tc-HYNIC-annexin.

Recently published animal experiments suggest an improved protocol for annexin labeling via the use of self-chelating annexin V mutants. In these cases, an amino acid sequence capable of metal chelation is added to the amino terminus of a linker peptide, followed by the wild-type annexin V [230]. The best-studied mutant capable of self-chelating technetium is known as V-117, and another commonly employed self-chelating annexin V mutant is known as V-128 [231]. In both cases, the radiotracers exhibit reduced abdominal background and decreased renal radiation dose.

Imaging Cancer Biomarkers with Antibodies

In 1908, Paul Ehrlich and Ilya Mechnikov received the Nobel Prize for Physiology and Medicine for their pioneering work on immunity. Ehrlich's legacy to medical science is profound, but the concept of "antibodies" and his vision that "magic bullets" could selectively target disease are arguably his most important contributions [232]. In 1975, Köhler and Milstein introduced hybridoma technology and, along with Jerne, received the Nobel Prize in 1984 for their work on the control of the immune system and the development of mAbs [233]. Further technological advances, including the development of chimeric (c-mAbs), humanized (h-mAbs), and fully human mAbs, have circumvented problems associated with immunogenicity. More recently, engineered mAb fragments have been embraced by radiochemists and nuclear physicians as potential radiotracers due to their tunable and highly specific target binding and favorable clearance properties. This section provides a brief overview of the methods used for the design and production of radioimmunoconjugates. A number of examples from recent clinical trials will further serve to illustrate the potential of mAb-based radiotracers for the diagnostic imaging and radioimmunotherapy (RIT) of cancer.

Radioimmunoconjugates

An immunoconjugate is defined as the combination of a diagnostic or therapeutic substance linked chemically to a specific immune species, such as an immunoglobulin, mAb, engineered mAb fragment, or antigen [234]. When the diagnostic or therapeutic group incorporates a radionuclide, the molecule is termed a radioimmunoconjugate. In recent years, radioimmunoconjugates have received a great deal of attention from the basic science and clinical research communities, and a wide range of radiolabeled mAbs and related fragments have been developed for use in both nuclear diagnostic imaging (immuno-SPECT and immuno-PET) and RIT [23, 25]. Immunoconjugates present one of the most versatile platforms for the design of site-specific radiopharmaceuticals due to their high in vivo stability, prolonged circulation time in blood, comparative ease of chemical functionalization, and high antigen specificity and affinity.

Antibody Structure

The basic structure of a monomeric immunoglobulin (Ig) and strategies for radiolabeling such a macromolecule are shown in Fig. 3.31. Antibodies are comprised of two heavy (yellow and blue) and two light (red and green) protein chains, with a total molecular weight around 150 kDa. The heavy chains have four distinct protein domains, three which are conserved (C_H1–C_H3) and one which has a highly variable sequence (V_H). The light chains have two protein domains: one constant (C_L) and one variable (V_L). The antigen recognition site is located at the end of the variable domains (V_H and V_L) and is known as the complementarity-determining region (CDR). Sequence variation in the V_H and V_L domains is responsible for the high target specificity displayed by antibodies and related fragments.

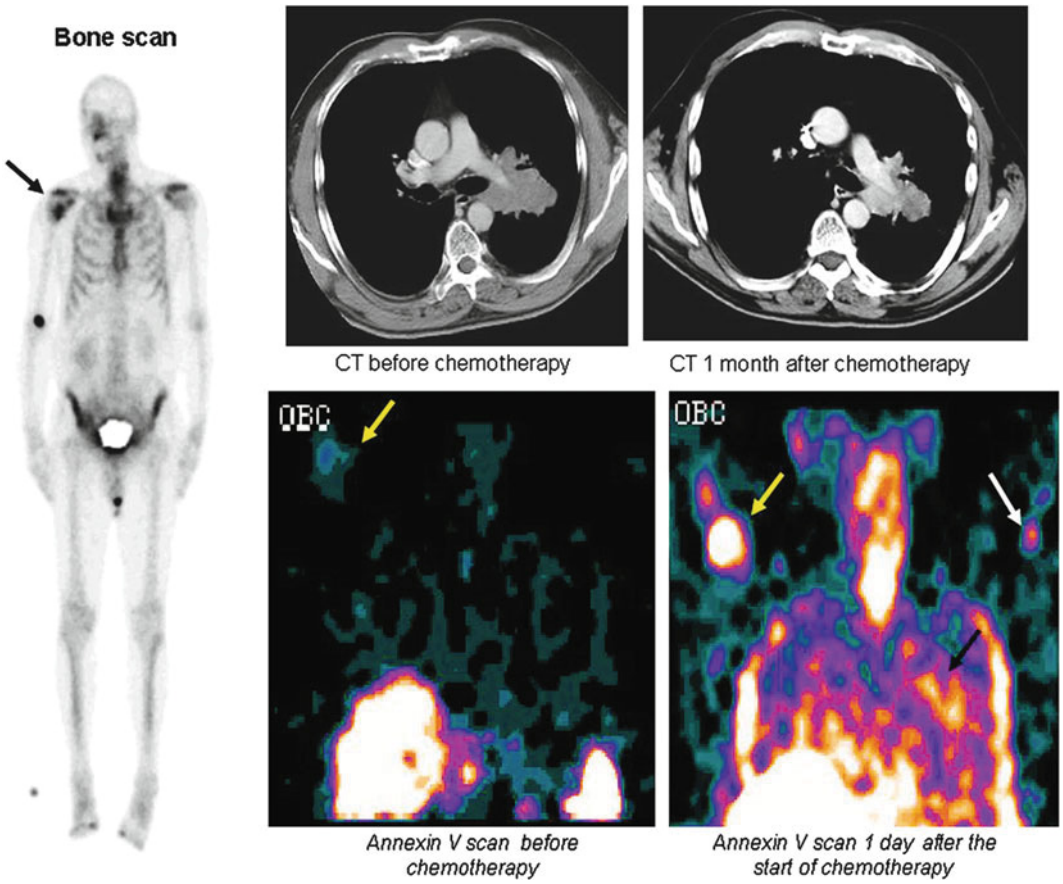

Fig. 3.30 (*Left*) new right humeral metastasis was demonstrated on bone scan (*black arrow*) in 70-year-old man with stage IV NSCLC. (*Right, top row*) Chest CT (axial or transverse plane) showed response to treatment at 1 month after treatment, with decrease in largest tumor diameter from 7.5 to 6.5 cm. (*Right, bottom row*) ^{99m}Tc-HYNIC-annexin V assessment (in coronal plane) revealed faint uptake at level of bony metastasis 2 h before first course of chemotherapy (*yellow arrows*), which significantly increased 1 day after start of therapy. In addition, increased tracer uptake was detected within primary lung tumor as early as 1 day after initiation of cis-platinum-based chemotherapy (*black arrow*). *White arrow* shows intravenous injection site in left arm. (Courtesy of Dr. Tarik Belhocine and Dr. Johan Vandevivere, Antwerp, Belgium, NAS Clinical Trial)

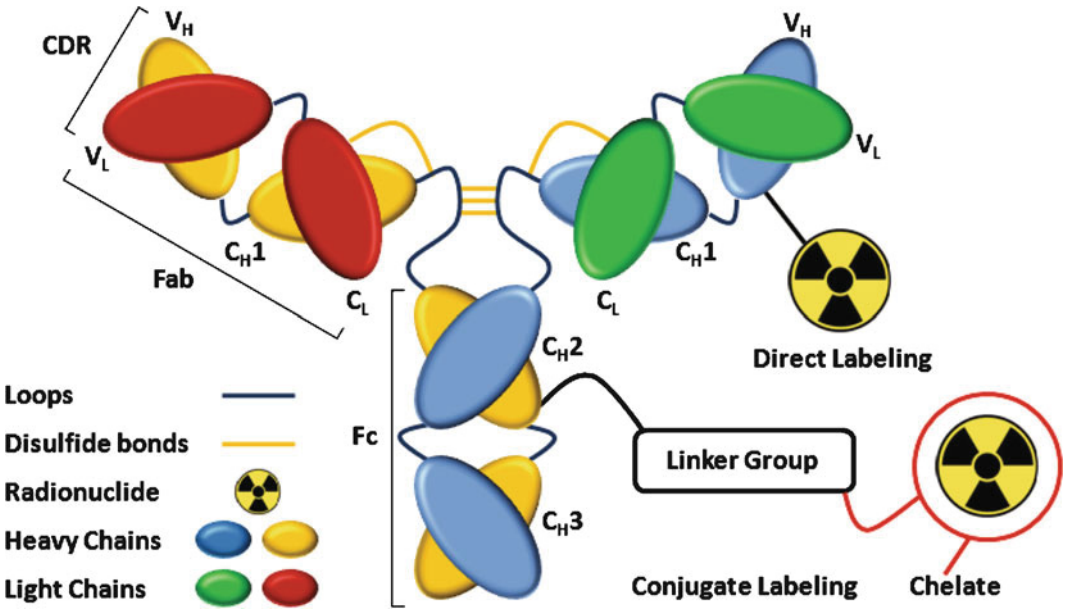

Fig. 3.31 Schematic representation of the structure of an intact IgG immunoglobulin showing the four main chains (two heavy and two light) with loops and disulfide bonding connecting variable (V) and constant (C) domains associated with the Fc and Fab and antigen-binding (CDR) regions. In a standard antibody, the *blue and green chains* are equivalent to the *yellow and red chains*, respectively, but are distinguished here for clarity. The concepts of direct and conjugate labeling strategies used in the preparation of radioimmunoconjugates are also illustrated

Humans produce five classes of immunoglobulins which are defined by the type of heavy chain: IgD, IgE, IgG (monomers), IgA (dimers), and IgM (pentamers), with corresponding heavy chains δ, ε, γ, α, and μ, respectively. Each class has a distinct and important role in the adaptive immune systems. However, the majority of research involving antibody constructs for nuclear medicine has focused on the use of IgG antibodies due to their prominent role in immunity against invading pathogens. Thus, the remainder of this section will focus on IgG molecules. A typical intact IgG antibody can be divided into distinct regions known as the Fab (fragment, antigen binding; C_H1, C_L, V_H, and V_L) and Fc (fragment, crystallizable; C_H2 and C_H3). The Fab fragment can be divided further, and the Fv region (fragment, variable; V_H and V_L) is often utilized in radiotracer design.

Monoclonal Antibodies

The advent of murine-based hybridoma cells (antibody-secreting, splenic-mouse plasma cells fused by cell membrane permeation with immortalized myeloma immune cells) led to the development of cell culture techniques for the facile production of antigen-specific murine mAbs in vitro [233]. Despite high antigen specificity and affinity, initial studies conducted using murine mAbs were often hampered by short serum half-lives, lack of interaction with human immune effector cells, and high immunogenicity [234]. The human immune system often develops an immune response with subsequent acquired resistance to the foreign murine mAbs through the production of human anti-mouse antibodies (HAMAs). Other techniques used to produce high-affinity monoclonal antibodies include phage, yeast or ribosomal display, and antibody generation using transgenic mice [234].

Many of the problems associated with the immunogenicity of murine mAbs were successfully overcome by the development of chimeric, humanized, and fully human mAbs (Fig. 3.32). A range of antibodies spanning each of the aforementioned types has been investigated clinically [23]. Examples include the anti-B-cell lymphoma CD20-targeting murine mAbs ibritumomab tiuxetan (^{90}Y-Zevalin) and tositumomab (^{131}I-Bexxar) for RIT; the chimeric anti-EGFR, anti-VEGF, and anti-CD20 antibodies cetuximab (Erbitux™) and rituximab (Rituxan™) for treatment of colorectal and B-cell lymphoma, respectively; the humanized mAbs trastuzumab (Herceptin™, anti-HER2/*neu* for breast cancer), bevacizumab (Avastin™, anti-VEGF for colorectal cancer), alemtuzumab (Campath™, anti-CD52 for chronic lymphocytic leukemia), and the drug conjugate gemtuzumab ozogamicin (Mylotarg™, anti-CD33 IgG_4 functionalized with calicheamicin for acute myelogenous leukemia); and the fully human mAb panitumumab (Vectibix™, anti-EGFR for metastatic colorectal cancer) [23]. Selected examples of clinical investigations using radiolabeled mAbs are presented below.

Further problems encountered in the use of mAb-based radiotracers include extravasation of the mAb from the blood supply into nontarget background tissue, low tumor delivery as a result of poor tumor vascularization, lymphatic drainage, antigen binding-site barriers, and low expression and heterogeneity of the target antigen. These factors affect tumor-to-background ratios, target tissue retention, and clearance.

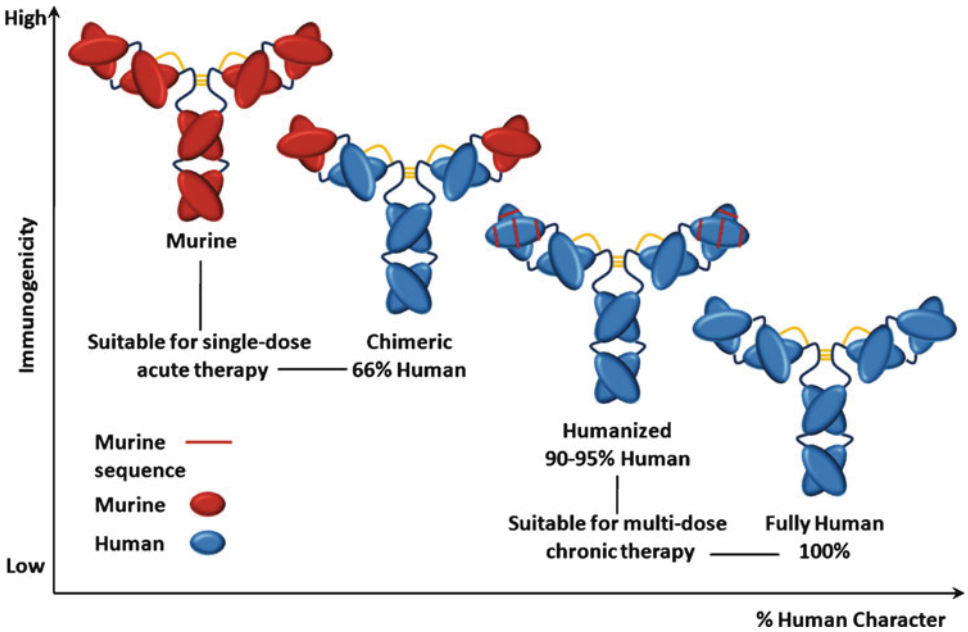

Fig. 3.32 Schematic representation of the relationship between the structure of engineered mAbs and their relative potential immunogenicity

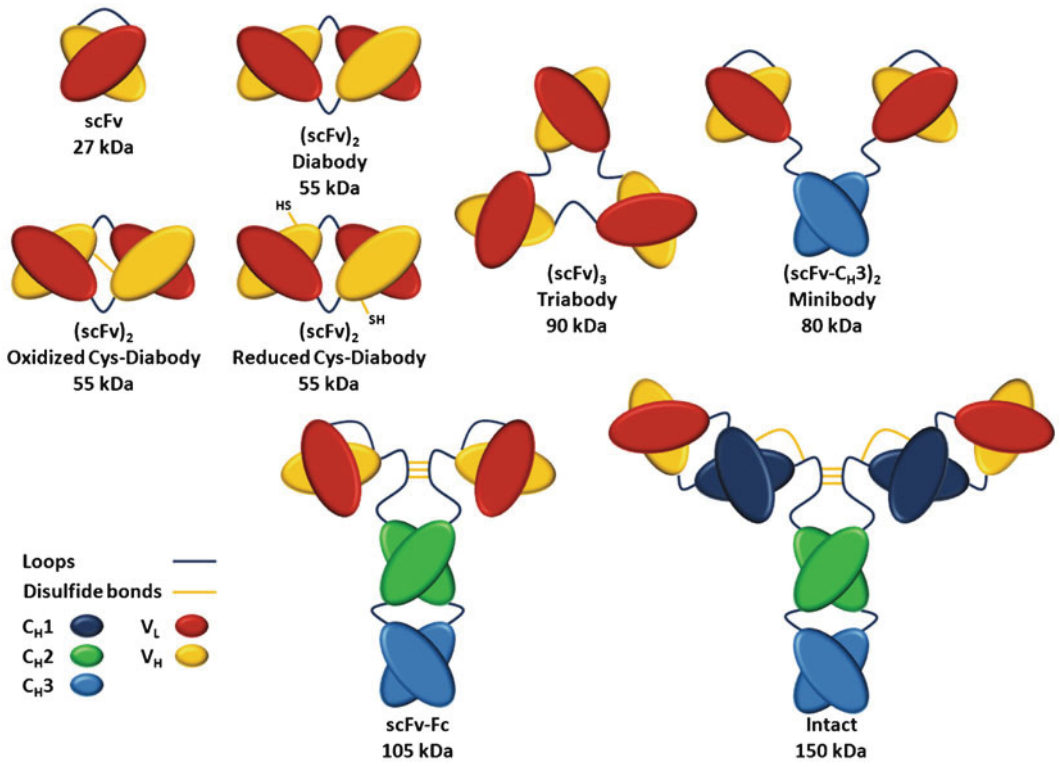

Fig. 3.33 Schematic representation of the structures of engineered antibody fragments

Antibody Fragments

Protein engineering has facilitated the development of a diverse range of immunoglobulin-based molecules (Fig. 3.33). The majority of these species have been produced by either genetic or chemical recombination of the normal protein domains found within IgG molecules. The new molecules are often smaller (lower molecular weight) than intact antibodies and are referred to as fragments.

Antibody fragments have the advantage that their affinity for a target antigen remains extremely high (sub-nanomolar range), while their molecular size can be adjusted to control blood pool and tissue clearance properties. Matching the physical half-life of the radionuclide with the biological half-life of the fragment and tuning the clearance properties for the desired application are important considerations in the design of radioimmunoconjugates. Wu and colleagues have investigated the effect of changing the type of antibody fragment on tumor uptake and blood clearance properties [234, 235]. They engineered a range of anti-carcinoembryonic antigen (anti-CEA) T84.88 mAb fragments, including a scFv, diabody, minibody, scFv-Fc-SM, scFv-Fc-DM, and the intact anti-CEA mAb, and subsequently measured the pharmacokinetics of the radioiodinated (^{124}I) species in athymic, nude mice bearing subcutaneous LS174T human colon carcinoma xenografts (Fig. 3.34). The bivalent, monospecific scFv-Fc-SM and scFv-Fc-DM antibodies have the same variable, C_H2, and C_H3 domains regions but have a either single or double mutation in the Fc region, respectively. These mutations modulate their interaction with the FcRn receptor and, as a result, modulate their pharmacokinetics. The studies provide a clear demonstration of the dramatic effect of molecular size and structure on both the absolute radiotracer uptake and retention in the tumor and the pharmacokinetics of clearance/excretion from the blood pool.

It is important to note that tumor and background tissue uptake and clearance are dependent not only on the size of the mAb fragment but also the antibody valency, topology, and antigen/receptor affinity. Phenotypic parameters—such as antigen expression levels in tumor and normal background tissue, tumor vascularization, and the natural rates of metabolism/excretion of the antigen and mAb/mAb fragment (including loss of the radionuclide from the immunoconjugate)—must also be considered when analyzing pharmacokinetic data.

Quality Control of Radiolabeled mAbs

In addition to the routine quality control tests which are performed for all radiolabeled compounds (see *Quality Control*, above), additional experiments are often conducted to ensure the suitability of the radioimmunoconjugates for use in humans. For radioimmunoconjugates, the chelation and radiolabeling chemistry involve modifying the structure of the

antibody species. As the function of antibodies is intimately linked to their structure, additional steps must be taken to verify that the antibody remains immunoreactive (i.e., retains its binding affinity and specificity for the target antigen) [236]. Immunoreactivity is often measured by using cell-based radiometric assays involving specific binding of the radioimmunoconjugate to cells expressing the target antigen. Simple cell association assays provide an estimate of the low bound of immunoreactive fraction, and for high-affinity antibodies, cellular-binding assays described by Lindmo et al. which involve extrapolation of the binding data to infinite antigen excess are frequently reported [237–239].

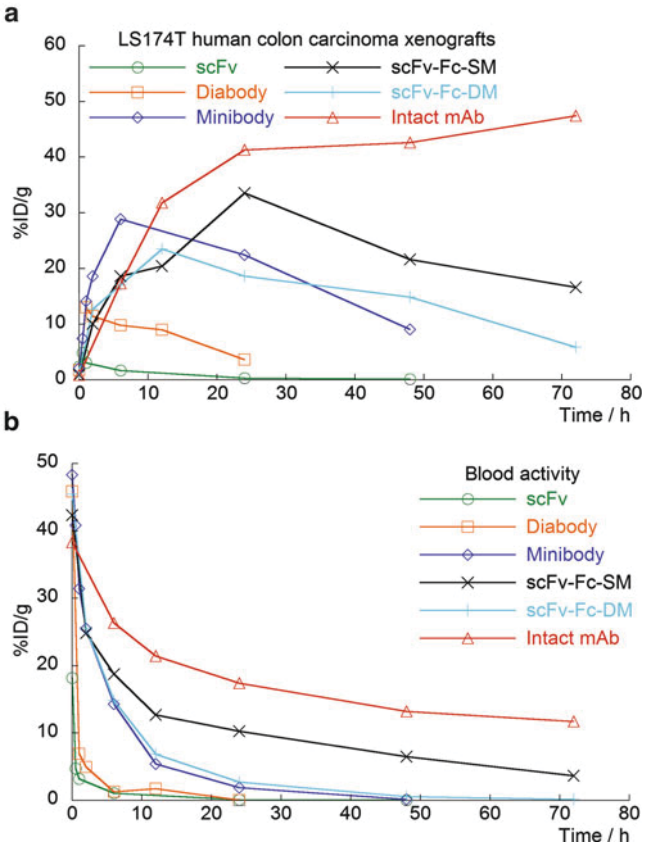

Fig. 3.34 Time–activity curves showing the uptake (**a**) and excretion (**b**) of ^{131}I-labeled anti-carcinoembryonic antigen (anti-CEA) T84.88 mAb fragments in athymic, nude mice bearing subcutaneous LS174T human colon carcinoma xenografts. Fragments studied include a scFv, diabody, minibody, scFv-Fc-SM, scFv-Fc-DM, and the intact anti-CEA mAb. (Data provided courtesy of Dr. Anna Wu)

In the case of conjugate labeling methods, the number of chelates covalently linked to the mAb is an important factor affecting both specific activity and immunoreactivity. One common approach for evaluating the number of accessible chelates is the use of radiometric isotopic dilution assays [240, 241]. Stability studies investigating both the loss of the radionuclide from the radioimmunoconjugate and the loss of immunoreactivity under varying conditions (e.g., incubation in human serum or DTPA solutions at pH7 and temperatures ranging from 4 to 37°C) must also be conducted prior to full in vivo studies.

Clinical Investigations

Despite the vast number of preclinical and clinical studies which have been reported over the last 15 years, only six radioimmunoconjugates (four immuno-SPECT radiotracers and two RIT agents) have received USFDA approval for use in humans (Table 3.7). Of the four immuno-SPECT agents that have been approved, only ProstaScint™ (EUSA Pharma) remains commercially available. In a recent review, Boswell and Brechbiel discussed the problems and challenges (both scientific and regulatory) that must be overcome if a radioimmunoconjugate is to be translated to the clinic [23]. Many of the problems associated with mAb translation arise from lack of progression through Phase III trials [242]. Selected ongoing Phase I, II, and III clinical trials involving radioimmunoconjugates for imaging and therapy are shown in Tables 3.8 and 3.9, respectively.

Table 3.7 Current USFDA-approved radioimmunoconjugates for use in the detection and treatment of cancer

Trade name	Generic name	Radionuclide	Antibody type	Target antigen	Cancer	Year of approval
Radioimmunodiagnostic agents						
OncoScint	Satumomab pendetide	^{111}In	Murine IgG	Anti-TAG-72	Colorectal and ovarian	1992
Verluma	Nofetumomab merpentan	^{99m}Tc	Murine fab'	Anti-EGP-1	Small-cell lung	1996
CEA-scan	Arcitumomab	^{99m}Tc	Murine fab'	Anti-CEA	Colorectal	1996
ProstaScint	Capromab pendetide	^{111}In	Murine IgG	Anti-PSMA	Prostate	1996
Radioimmunotherapeutic agents						
Zevalin	Ibritumomab tiuxetan	^{90}Y	Murine IgG+rituximab	Anti-CD20	B-cell lymphoma	2002
Bexxar	Tositumomab	^{131}I	Murine IgG+"cold" tositumomab	Anti-CD20	B-cell lymphoma	2003

Source: http://www.clinicaltrials.gov. Accessed October 15, 2009

Table 3.8 Selected ongoing clinical trials involving radioimmunoimaging

Sponsor	Radioimmunoconjugate	Cancer	Clinical trial code	Phase
Maastricht Radiation Oncology/VU University Medical Center	^{89}Zr-Cetuximab	Non-small-cell lung cancer	NCT00691548	I
Memorial Sloan-Kettering Cancer Center	^{64}Cu-Trastuzumab (anti-Her2/*neu*)	Breast cancer	NCT00605397	
Memorial Sloan-Kettering Cancer Center	^{68}Ga-Trastuzumab F(ab')$_2$	Breast cancer	NCT00613847	
Ludwig Institute for Cancer Research/ Memorial Sloan-Kettering Cancer Center	^{124}I-huA33	Colorectal cancer	NCT00199862	I
Ludwig Institute for Cancer Research/ Pfizer/Wilex	^{124}I-cG250 + Sunitinib malate	Renal cell carcinoma	NCT00520533	I

Source: http://www.clinicaltrials.gov. Accessed October 15, 2009

Table 3.9 Selected ongoing clinical trials involving radioimmunotherapy

Sponsor	Radioimmunoconjugate	Cancer	Clinical trial code	Phase
University of Nebraska	^{131}I-Tositumomab	Non-Hodgkin's lymphoma	NCT00574509	I
Weill Medical College of Cornell University	^{131}I-Tositumomab + radiosensitization with bortezomib	Non-Hodgkin's lymphoma	NCT00777114	I
Fred Hutchinson Cancer Research Center	^{131}I-Tositumomab + fludarabine + rituximab	B-cell chronic lymphocytic leukemia	NCT00476047	II
Peregrine Pharmaceuticals	^{131}I-chTNT-1/B (Cotara™)	Glioblastoma multiforme (GBM)	NCT00509301 NCT00677716	I/II
Nantes University Hospital	Anti-CEA × anti-DTPA bispecific antibody and di-DTPA-^{131}I	Medullary thyroid carcinoma	NCT00467506	II
University of Pennsylvania/ GlaxoSmithKline	^{131}I-Tositumomab	B-cell lymphoma	NCT00434629	I
Eastern Hepatobiliary Surgery Hospital	^{131}I-Metuximab (Licartin™)	Hepatocellular carcinoma	NCT00819650	II
Memorial Sloan-Kettering Cancer Center/NCI	^{131}I-A33 humanized	Colorectal cancer	NCT00003360	I
Ireland Cancer Center/NCI	^{131}I-Lym-1	Large B-cell lymphoma	NCT00028613	I
Duke University	^{131}I-81C6	Brain and CNS tumors	NCT00002753	I/II
Fred Hutchinson Cancer Research Center	^{131}I-BC8 (Anti-CD45)	Lymphoma	NCT00860171	I
Duke University/NCI	^{131}I-MEL-14 F(ab')$_2$	Brain and CNS tumors Melanoma (skin) Metastatic cancer	NCT00002754	I
University of Michigan Cancer Center GlaxoSmithKline Millennium Pharmaceuticals, Inc.	^{131}I-Tositumomab + Bortezomib	Lymphoma	NCT00398762	I
Memorial Sloan-Kettering Cancer Center/NCI	^{225}Ac-huM195 (Anti-CD33)	Leukemia Myelodysplastic syndrome	NCT00672165	I
Ludwig Institute for Cancer Research/Memorial Sloan-Kettering Cancer Center	^{90}Y-DOTA-cG250	Renal cell carcinoma Kidney neoplasm Renal cancer Kidney cancer	NCT00199875	I
Charite University, Berlin, Germany	^{90}Y-Ibritumomab tiuxetan + rituximab	Follicular lymphoma	NCT00772655	II
Weill Medical College of Cornell University	^{177}Lu-J591	Prostate cancer	NCT00859781	II
M.D. Anderson Cancer Center/ Biogen Idec	^{90}Y-Ibritumomab tiuxetan + rituximab	Lymphoma leukemia	NCT00048737	I/II

Diagnostic Radioimmunoconjugates

Only four agents have been approved for immuno-SPECT, and at present, no radioimmunoconjugate for immuno-PET has been approved for human use [23]. However, examination of the Clinical Trials database reveals that a large number of Phase I and II trials exploring the potential of both immuno-PET and immuno-SPECT agents as diagnostic radiotracers for a range of cancer phenotypes have been undertaken during the last 5 years (Table 3.8) [243, 244]. With the increased availability of unconventional radionuclides, many of the clinical trials are now using radionuclides such as ^{64}Cu, ^{68}Ga, ^{89}Zr, and ^{124}I. This section provides a brief overview of the reported clinical studies utilizing the aforementioned radionuclides.

^{64}Cu-Labeled Antibodies

^{64}Cu-BAT-2IT (where BAT = 6-bromoacetamidobenzyl-1,4,8,11-tetraazacyclotetradecane-1,4,8,11-tetraacetic acid and 2IT = 2-iminothiolane) conjugated to the monoclonal antibody 1A3 was one of the first ^{64}Cu-radioimmunoconjugates to be evaluated in humans [245]. Preclinical studies of ^{64}Cu-BAT-2IT-1A3 showed high immunoreactive fractions (85–95%), and in vivo experiments in GW39 human colon carcinoma tumor-bearing hamsters showed high tumor uptake (14.4 ± 4.8%ID/g) at 24 h post-i.v. administration [246].

In the first Phase I/II clinical study using a ^{64}Cu-radiopharmaceutical, Philpott et al. compared [^{18}F]FDG and ^{64}Cu-BAT-2IT-1A3 uptake in 36 patients with suspected advanced primary or metastatic colorectal cancer [245]. The results demonstrated that ^{64}Cu-BAT-2IT-1A3 was more specific for detecting colorectal tumors than [^{18}F]FDG. [^{18}F]FDG showed false-positive indications in patients with inflammatory lesions (Fig. 3.35). The sensitivity of ^{64}Cu-BAT-2IT-1A3 was found to be 86% per patient and 71% per lesion, which was improved over radioimmunoscintigraphy using ^{111}In-1A3 (76% per patient and 63% per lesion) [245, 247]. Further preclinical studies also investigated the therapeutic potential of BAT-2IT-1A3 radiolabeled with either ^{64}Cu or ^{67}Cu and demonstrated that ^{64}Cu has clear potential for use in the design of RIT agents [248].

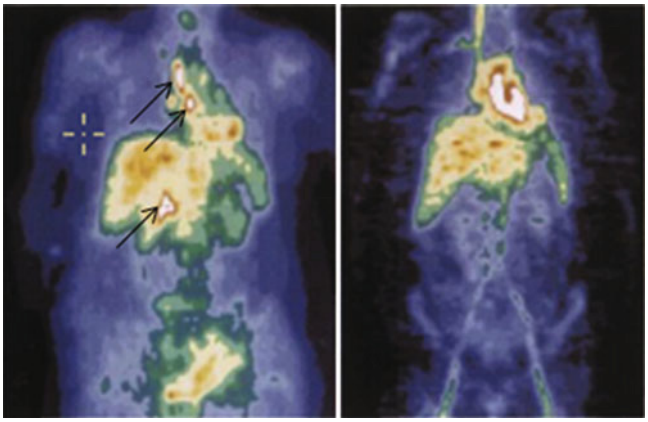

Fig. 3.35 Anterior volume-rendered re-projection PET images recorded by using [^{18}F]FDG (*left*) and ^{64}Cu-BAT-2IT-1A3 (*right*) in a woman post-resection of Dukes' C rectal cancer 12 months before enlarged mediastinal and periportal lymph nodes were observed. The lymph notes were strongly positive on [^{18}F]FDG-PET (*left panel—black arrows*) but were negative with ^{64}Cu-BAT-2IT-1A3 (*right panel*). Subsequent analysis of the lymph nodes demonstrated sarcoidosis. (From Philpott GW, Schwarz SW, Anderson CJ, et al. RadioimmunoPET: detection of colorectal carcinoma with positron-emitting copper-64-labeled monoclonal antibody. J Nucl Med. 1995;36:1818–24. Reprinted with permission of the Society of Nuclear Medicine)

^{89}Zr-Labeled Antibodies

The use of ^{89}Zr for immuno-PET has been pioneered by the research teams at the Vrije University Medical Centre (Amsterdam, The Netherlands). ^{89}Zr is a particularly attractive radionuclide for immuno-PET due to its favorable decay characteristics, including a 78.41 h half-life which matches closely the optimum biodistribution times for intact IgG molecules (Fig. 3.34). In addition, preclinical investigations have demonstrated that PET image resolution using ^{89}Zr is comparable to the high-resolution images obtained using ^{18}F or ^{64}Cu [28, 31, 249, 250]. Conjugation methods are based on the use of DFO [28–30, 251, 252]. Perk et al. reported the first human immuno-PET images recorded in a pilot study comparing the uptake of [^{18}F]FDG with ^{89}Zr-Zevalin™ in a B-cell CD20-positive patient with non-Hodgkin's lymphoma (NHL, Fig. 3.36) [249]. Serial PET images showed selective uptake of ^{89}Zr-Zevalin™ in all tumor lesions that had previously been identified by [^{18}F]FDG-PET. Evaluation of the ^{89}Zr-immuno-PET images suggested that tumor uptake of ^{89}Zr-Zevalin™ in NHL patients may be used as a screening method prior to commencing RIT using ^{90}Y-Zevalin.

In 2006, Börjesson et al. described results from the first full-scale clinical trial of a ^{89}Zr-labeled mAb. They investigated the ability of ^{89}Zr-DFO-U36 (a chimeric anti-CD44v6 mAb), in patients with squamous cell carcinoma of the head and neck (HNSCC). Twenty patients received 75 MBq of ^{89}Zr-DFO-U36 coupled to 10 mg of the mAb. Immuno-PET images were acquired up to 144 h after injection. Their results indicated that ^{89}Zr-immuno-PET detected all primary tumors ($n = 17$) as well as lymph node metastases with a sensitivity of 72% and accuracy of 93%. The data were comparable to the diagnostic results obtained by using [^{18}F]FDG-PET, computed tomography, and magnetic resonance imaging in the same patients.

^{124}I-Labeled Antibodies

^{124}I is a promising radionuclide for immuno-PET, yet the high-energy γ-ray emissions which occur during ^{124}I decay mean that dosimetry with this radionuclide may be a limiting factor to its clinical impact. However, standardized protocols

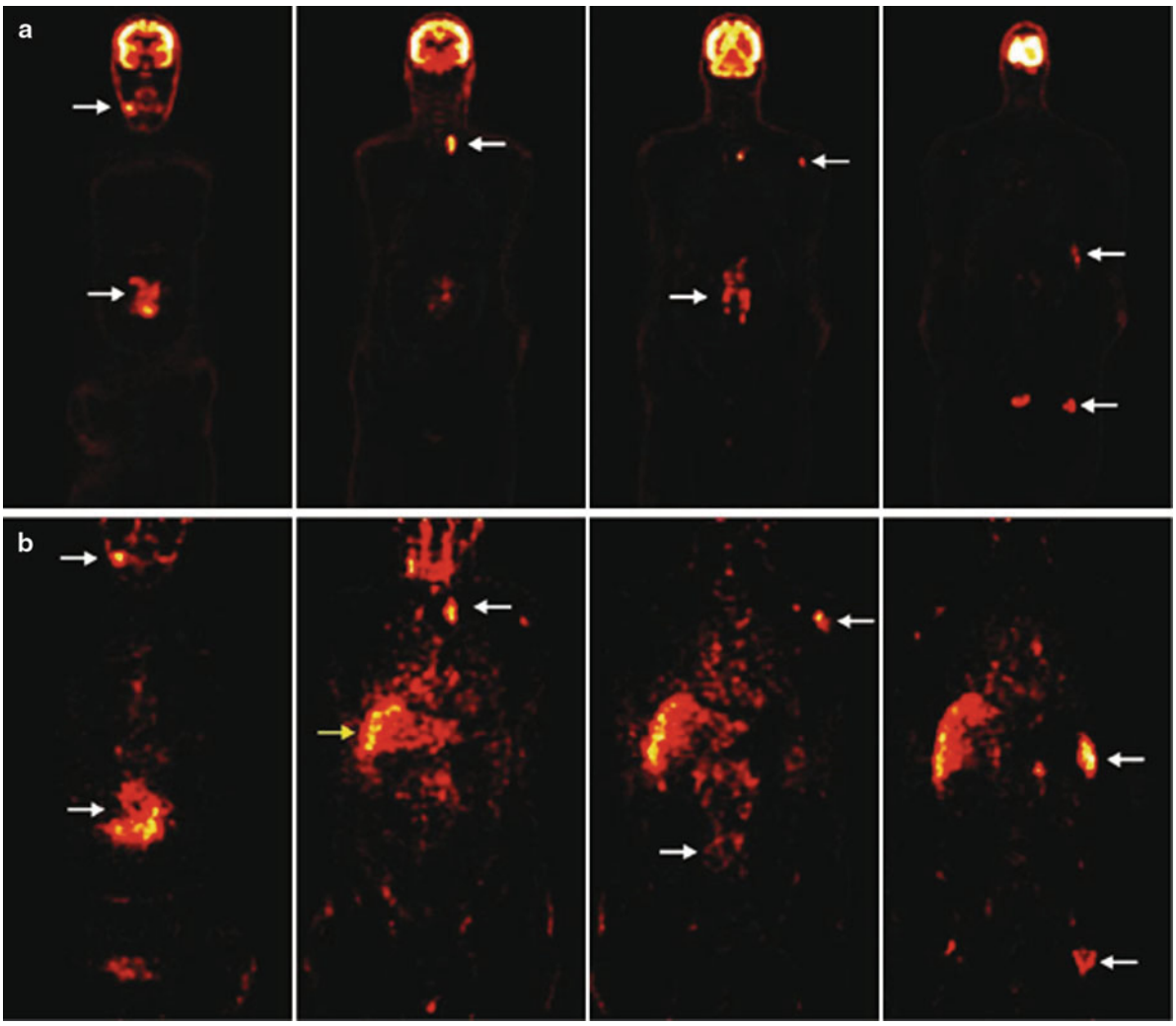

Fig. 3.36 (**a**) [^{18}F]FDG-PET scan of a non-Hodgkin's lymphoma patient. Coronal images from anterior (*left*) to posterior (*right*), with visualization of cervical, mediastinal, left caput humeri, splenic, para-aortic, and inguinal lymphomas. (**b**) ^{89}Zr-Zevalin immuno-PET scan 96 h postinjection of the same NHL patient. Coronal images from anterior (*left*) to posterior (*right*); slices correspond to those presented in the [^{18}F]FDG-PET images. Liver uptake (*yellow arrow*) is potentially due to retention of ^{89}Zr after catabolism of the radioimmunoconjugate. (From [249] with kind permission from Springer Science and Business Media)

for radiolabeling mAbs with iodine mean that in the immediate future, ^{124}I is set to play a prominent role in preclinical and clinical immuno-PET studies.

Divgi et al. recently completed Phase I clinical investigations of the ability of ^{124}I-cG250, a chimeric mAb directed against carbonic anhydrase IX, in clear-cell renal carcinoma, the most common and aggressive renal tumor [253]. In total, 26 patients with renal masses received a single intravenous infusion of 185 MBq/10 mg of ^{124}I-cG250. The results revealed that 15 of 16 clear-cell carcinomas were identified accurately by ^{124}I-immuno-PET, and all nine non-clear-cell renal masses were negative for the tracer (Fig. 3.37). The sensitivity of ^{124}I-cG250 immuno-PET for clear-cell kidney carcinoma in this trial was 94%, the negative predictive value was 90%, and the specificity and positive predictive accuracy were both 100%.

The conclusions from the study were that immuno-PET with ^{124}I-cG250 can identify accurately clear-cell renal carcinoma; further, a negative scan is highly predictive of a less aggressive phenotype. Stratification of patients with renal masses by ^{124}I-cG250 PET can identify aggressive tumors and help decide treatment.

Radioimmunotherapeutic Agents

The majority of clinical RIT investigations have focused on the use of the commercially available radionuclides ^{90}Y and ^{131}I. More recently, β- and α-emitting radionuclides such as ^{67}Cu, ^{177}Lu, $^{186/188}$Re, ^{213}Bi, and ^{225}Ac have been exploited for

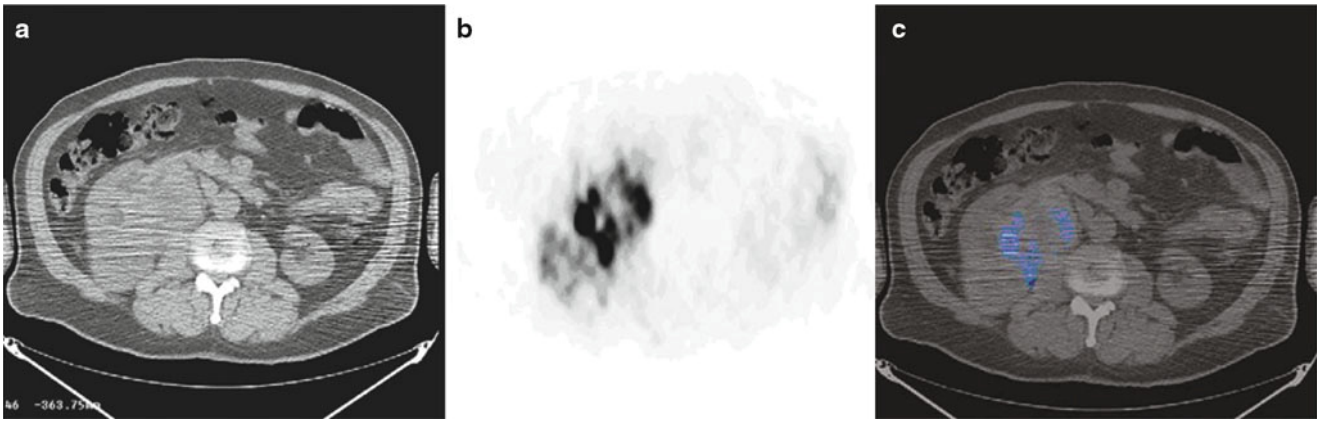

Fig. 3.37 Transaxial CT (**a**), immuno-PET (**b**), and fused image (**c**) from a patient with a large clear-cell renal carcinoma. Immuno-PET images were recorded using ^{124}I-cG250 (185 MBq/10 mg). (From Divgi CR, Pandit-Taskar N, Jungbluth AA, et al. Preoperative characterisation of clear-cell renal carcinoma using iodine-124-labeled antibody chimeric G250 ([^{124}I]-cG250) and PET in patients with renal masses: a phase I trial. Lancet Oncol. 2007;8:304–10 with permission)

site-directed RIT (Tables 3.3, 3.4, and 3.9). The concept of "arming antibodies" to carry a lethal radioactive or chemotherapeutic payload has been the subject of several excellent reviews [234, 254, 255].

The use of β-emitting radionuclides is particularly suited for the treatment of large, solid tumors. β-particles have a much longer range in tissue (approximately 1–10 mm) than α-particles (~50 μm). For this reason, α-therapy is best suited for combination with internalizing antibodies which sequester the radioactivity inside the cell, thereby enhancing the potential for DNA-ionization-induced apoptosis.

At present, clinical studies using β-emitting radionuclides are more advanced than studies involving α-immunotherapy agents. For example, many clinical trials using ^{90}Y and ^{131}I have entered Phase II/III, and one trial using the prostate-specific membrane antigen (PSMA) targeting humanized mAb, J591, functionalized with ^{177}Lu-DOTA for targeted therapy of prostate cancer has entered Phase II studies (NCT00859781, Table 3.9). Another clinical trial investigating the effect of ^{225}Ac-hM195 for anti-CD33 therapy of leukemia and myelodysplastic syndrome is ongoing (NCT00672165).

Conclusions

Above all, three impressions stand out from this or any other survey of radiopharmaceuticals in oncology: diversity, applicability, and potential. Not only have radiotracers facilitated the imaging of a wide variety of malignancies, but the field is characterized by remarkable diversity in the targeting strategies, molecular targets, and radiolabeling chemistry employed in the development of imaging agents. Every day, many of these radiopharmaceuticals—notably [^{18}F]FDG, [^{111}In]-Octreoscan™, and [^{90}Y]-Zevalin™—are having a clinical impact on the diagnosis, staging, and treatment of cancer. Yet the future of nuclear oncology is even more exciting than the present, with a burgeoning number of agents in clinical trials and an ever-increasing library of molecules in laboratory development. Indeed, the rest of this text—with chapters on topics ranging from the radioimaging of melanoma (Chap. 24) to the radiotherapy of lymphoma (Chap. 7)—will only continue to emphasize and elaborate on these important themes.

References

1. Rudin M, Weissleder R. Molecular imaging in drug discovery and development. Nat Rev Drug Discov. 2003;2:123–31.
2. Gillies RJ. In vivo molecular imaging. J Cell Biochem. 2002;87:231–8.
3. Smith SV. Molecular imaging with copper-64. J Inorg Biochem. 2004;98:1874–901.
4. Blower P. Towards molecular imaging and treatment of disease with radionuclides: the role of inorganic chemistry. Dalton Trans. 2006;(14):1705–11.
5. Mettler JFA, Guiberteau MJ. Essentials of nuclear medicine imaging. 5th ed. Philadelphia, Pennsylvania, USA: Saunders Elsevier; 2007.
6. Dilworth JR, Parrott SJ. The biomedical chemistry of technetium and rhenium. Chem Soc Rev. 1998;27:43–55.
7. Harper PV, Beck R, Charleston D, Lathrop KA. Mo/Tc generator. Nucleonics. 1964;22:1137.
8. Marsden PK. Detector technology challenges for nuclear medicine and PET. Nucl Instrum Meth Phys Res. 2003;513:1–7.
9. Brownell GL, Sweet WH. Localization of brain tumors with positron emitters. Nucleonics. 1953;11:40–5.
10. Sweet WH. The use of nuclear disintegration in the diagnosis and treatment of brain tumor. N Engl J Med. 1951;245:875–8.
11. Wrenn Jr FR, Good ML, Handler P. The use of positron-emitting radioisotopes for the localization of brain tumors. Science. 1951;113:525–7.
12. Phelps ME. Positron emission tomography provides molecular imaging of biological processes. Proc Natl Acad Sci USA. 2000;97:9226–33.

13. Bushberg JT, Seibert JA, Leidholdt EW, Boone JM. The essential physics of medical imaging. 2nd ed. Philadelphia: Lippincott Williams & Wilkins; 2006.
14. Marsden PK. Quantification in PET: what is it? Can we do it? Do we need it? Nucl Med Commun. 2004;25:635–6.
15. Wiebe LI. PET radiopharmaceuticals for metabolic imaging in oncology. Int Congr. 2004;1264:53–76.
16. Lodge MA, Lucas JD, Marsden PK, Cronin BF, O'Doherty MJ, Smith MA. A PET study of ^{18}FDG uptake in soft tissue masses. Eur J Nucl Med. 1999;26:22–30.
17. Somer Edward JR, Marsden Paul K, Benatar Nigel A, Goodey J, O'Doherty Michael J, Smith Michael A. PET-MR image fusion in soft tissue sarcoma: accuracy, reliability and practicality of interactive point-based and automated mutual information techniques. Eur J Nucl Med Mol Imaging. 2003;30:54–62.
18. Quon A, Napel S, Beaulieu Christopher F, Gambhir Sanjiv S. "Flying through" and "flying around" a PET/CT scan: pilot study and development of 3D integrated ^{18}F-FDG PET/CT for virtual bronchoscopy and colonoscopy. J Nucl Med. 2006; 47:1081–7.
19. Somer E, Benatar N, O'Doherty M, Smith M, Marsden P. Use of the CT component of PET/CT to improve PET/MR registration: demonstration in soft-tissue sarcoma. Phys Med Biol. 2007;52:6991–7006.
20. Stanford M-MIPa. Medical Imaging Program at Stanford. Stanford University, Palo Alto, CA.
21. Welch MJ, Redvanly CS, editors. Handbook of radiopharmaceuticals: radiochemistry and applications. Chichester: Wiley; 2003.
22. Katzenellenbogen JA. Designing steroid receptor-based radiotracers to image breast and prostate tumors. J Nucl Med. 1995;36:8S–13S.
23. Boswell CA, Brechbiel MW. Development of radioimmunotherapeutic and diagnostic antibodies: an inside-out view. Nucl Med Biol. 2007;34:757–78.
24. Hermanson GT. Bioconjugate techniques. London: Academic, Elsevier; 2008.
25. Nayak TK, Brechbiel MW. Radioimmunoimaging with longer-lived positron-emitting radionuclides: potentials and challenges. Bioconjug Chem. 2009;20:825–41.
26. Brechbiel MW. Bifunctional chelates for metal nuclides. Q J Nucl Med Mol Imaging. 2008;52:166–73.
27. Volkert WA, Hoffman TJ. Therapeutic radiopharmaceuticals. Chem Rev. 1999;99:2269–92.
28. Verel I, Visser GWM, Boellaard R, Stigter-van Walsum M, Snow GB, van Dongen GAMS. ^{89}Zr immuno-PET: comprehensive procedures for the production of ^{89}Zr-labeled monoclonal antibodies. J Nucl Med. 2003;44:1271–81.
29. Meijs WE, Haisma HJ, Van der Schors R, et al. A facile method for the labeling of proteins with zirconium isotopes. Nucl Med Biol. 1996;23:439–48.
30. Meijs WE, Herscheid JDM, Haisma HJ, Pinedo HM. Evaluation of desferal as a bifunctional chelating agent for labeling antibodies with Zr-89. Appl Radiat Isot. 1992;43:1443–7.
31. Holland JP, Sheh Y, Lewis JS. Standardized methods for the production of high specific-activity zirconium-89. Nucl Med Biol. 2009;36:729–39.
32. Katzenellenbogen JA. The pharmacology of steroid radiopharmaceuticals: specific and non-specific binding and uptake selectivity. In: Nunn AD, editor. Radiopharmaceuticals: chemistry and pharmacology. New York: Marcel Dekker, Inc; 1992. p. 297–331.
33. Gao H, Katzenellenbogen JA, Garg R, Hansch C. Comparative QSAR analysis of estrogen receptor ligands. Chem Rev. 1999;99:723–44.
34. Katzenellenbogen JA, Heiman DF, Carlson KE, Lloyd JE. In vivo and in vitro steroid receptor assays in the design of estrogen radiopharmaceuticals. In: Eckelman WC, editor. Receptor-binding radiotracers. Boca Raton: CRC; 1982. p. 93–126.
35. Francesconi LF, Cantorias MV, Howell RC. Metal-based imaging agents. In: King RB, editor. Encyclopedia of inorganic chemistry. 2nd ed. Chichester: Wiley; 2006. p. 3020–40.
36. Katzenellenbogen JA. Receptor imaging of tumors (non-peptide). In: Welch MJ, Redvanly CS, editors. Handbook of radiopharmaceuticals. Chichester: Wiley; 2003. p. 715–50.
37. Gallagher BM, Ansari A, Atkins H, et al. Radiopharmaceuticals 27. F-18-labeled 2-deoxy-2-fluoro-D-glucose as a radiopharmaceutical for measuring regional myocardial glucose metabolism in vivo—tissue distribution and imaging studies in animals. J Nucl Med. 1977;18:990–6.
38. Ido T, Wan CN, Casella V, et al. Labeled 2-deoxy-D-gluocose analogs—F-18-labeled 2-deoxy-2-fluoro-D-glucose, 2-deoxy-2-fluoro-D-mannose, and C-14-2-deoxy-2-fluoro-D-glucose. J Label Compd Radiopharm. 1978;14:175–83.
39. Dotzel MM. Federal register. In: United States Department of Health and Human Services, editor. 2000. 12999–3010.
40. Rohren EM, Turkington TG, Coleman RE. Clinical applications of PET in oncology. Radiology. 2004;231:305–32.
41. Plathow C, Weber WA. Tumor cell metabolism imaging. J Nucl Med. 2008;49:43S–63S.
42. Warburg O, Posener K, Negelein E. Ueber den stoffwechsel von carcinomzelle. Biochem Z. 1924;152:309–35.
43. Gillies RJ, Robey I, Gatenby RA. Causes and consequences of increased glucose metabolism of cancers. J Nucl Med. 2008;49:24S–42S.
44. Altenberg B, Greulich KO. Genes of glycolysis are ubiquitously overexpressed in 24 cancer classes. Genomics. 2004;84:1014–20.
45. Kim JW, Dang CV. Cancer's molecular sweet tooth and the Warburg effect. Cancer Res. 2006;66:8927–30.
46. Macheda ML, Rogers S, Best JD. Molecular and cellular regulation of glucose transporter (GLUT) proteins in cancer. J Cell Physiol. 2005;202:654–62.
47. Chesney J. 6-phosphofructo-2-kinase/fructose-2,6-bisphosphatase and tumor cell glycolysis. Curr Opin Clin Nutr Metab Care. 2006;9:535–9.
48. Pauwels EKJ, Sturm EJC, Bombardieri E, Cleton FJ, Stokkel MPM. Positron-emission tomography with [F-18]fluorodeoxyglucose Part I. Biochemical uptake mechanism and its implication for clinical studies. J Cancer Res Clin Oncol. 2000;126:549–59.
49. Voet D, Judith G, Pratt CW. Fundamentals of biochemistry: life at the molecular level. Hoboken: Wiley; 2008.
50. Caraco C, Aloj L, Eckelman WC. Retention of FDG in cancer cells: the role of glucose-6-phosphatase. J Nucl Med. 1997;38:1048.
51. Kostakoglu L, Agress H, Goldsmith SJ. Clinical role of FDG PET in evaluation of cancer patients. Radiographics. 2003;23:315–40.
52. Kostakoglu L, Wong JCH, Barrington SF, Cronin BF, Dynes AM, Maisey MN. Speech-related visualization of laryngeal muscles with fluorine-18-FDG. J Nucl Med. 1996;37:1771–3.
53. Park YH, Baik JH, Ahn MI, Kim JY. FDG uptake in the diaphragm and crura, vocal cords, and base of tongue in a crying child. Clin Nucl Med. 2005;30:752–3.
54. Shreve PD, Anzai Y, Wahl RL. Pitfalls in oncologic diagnosis with FDG PET imaging: physiologic and benign variants. Radiographics. 1999;19:61–77.
55. Khandani AH, Whitney KD, Keller SM, Isasi CR, Blaufox MD. Sensitivity of FDG PET, GLUT1 expression and proliferative index in bronchioloalveolar lung cancer. Nucl Med Commun. 2007;28:173–7.
56. Hicks RJ. Beyond FDG: novel PET tracers for cancer imaging. Cancer Imaging. 2003;4(1):22–4.
57. Bakheet SM, Saleem M, Powe J, Al Amro A, Larsson SG, Mahassin Z. F-18 fluorodeoxyglucose chest uptake in lung inflammation and infection. Clin Nucl Med. 2000;25:273–8.
58. Kubota R, Yamada S, Kubota K, Ishiwata K, Tamahashi N, Ido T. Intratumoral distribution of fluorine-18-fluorodeoxyglucose

in vivo—high accumulation in macrophages and granulation tissues studied by microautoradiography. J Nucl Med. 1992;33: 1972–80.
59. Ruers TJM, Langenhoff BS, Neeleman N, et al. Value of positron emission tomography with [F-18]fluorodeoxyglucose in patients with colorectal liver metastases: a prospective study. J Clin Oncol. 2002;20:388–95.
60. Kubota K. From tumor biology to clinical PET: a review of positron emission tomography (PET) in oncology. Ann Nucl Med. 2001;15:471–86.
61. Castell F, Cook GJR. Quantitative techniques in ^{18}FDG PET scanning in oncology. Br J Cancer. 2008;98:1597–601.
62. Thie JA. Understanding the standardized uptake value, its methods, and implications for usage. J Nucl Med. 2004;45:1431–4.
63. Romer W, Hanauske AR, Ziegler S, et al. Positron emission tomography in non-Hodgkin's lymphoma: assessment of chemotherapy with fluorodeoxyglucose. Blood. 1998;91:4464–71.
64. Gambhir SS, Czernin J, Schwimmer J, Silverman DHS, Coleman RE, Phelps ME. A tabulated summary of the FDG PET literature. J Nucl Med. 2001;42:1S–93S.
65. Brink I, Schumacher T, Mix M, et al. Impact of [F-18]FDG-PET on the primary staging of small-cell lung cancer. Eur J Nucl Med Mol Imaging. 2004;31:1614–20.
66. de Geus-Oei LF, Oyen LJG. Predictive and prognostic value of FDG-PET. Cancer Imaging. 2008;8:70–80.
67. Quon A, Gambhir SS. FDG-PET and beyond: molecular breast cancer imaging. J Clin Oncol. 2005;23:1664–73.
68. Fletcher JW, Djulbegovic B, Soares HP, et al. Recommendations on the use of F-18-FDG PET in oncology. J Nucl Med. 2008;49:480–508.
69. Cavallaro U, Christofori G. Molecular mechanisms of tumor angiogenesis and tumor progression. J Neurooncol. 2000;50: 63–70.
70. Vailhe B, Vittet D, Feige JJ. In vitro models of vasculogenesis and angiogenesis. Lab Invest. 2001;81:439–52.
71. Niu G, Chen X. PET imaging of angiogenesis. PET Clin. 2009;4:17–38.
72. Risau W. Mechanisms of angiogenesis. Nature. 1997;386:671–4.
73. Folkman J, Bach M, Rowe JW, et al. Tumor angiogenesis—therapeutic implications. N Engl J Med. 1971;285:1182–6.
74. van der Veldt AAM, Luurtsema G, Lubberink M, Lammertsma AA, Hendrikse NH. Individualized treatment planning in oncology: role of PET and radiolabelled anticancer drugs in predicting tumour resistance. Curr Pharm Des. 2008;14:2914–31.
75. Ferrara N. Vascular endothelial growth factor: basic science and clinical progress. Endocr Rev. 2004;25:581–611.
76. Cai WB, Chen XY. Multimodality molecular imaging of tumor angiogenesis. J Nucl Med. 2008;49:113S–28S.
77. Cai W, Chen K, Mohamedali KA, et al. PET of vascular endothelial growth factor receptor expression. J Nucl Med. 2006;47: 2048–56.
78. Jayson GC, Zweit J, Jackson A, et al. Molecular imaging and biological evaluation of HuMV833 anti-VEGF antibody: implications for trial design of antiangiogenic antibodies. J Natl Cancer Inst. 2002;94:1484–93.
79. Hynes RO. Integrins: bidirectional, allosteric signaling machines. Cell. 2002;110:673–87.
80. Lewis MR. Radiolabeled RGD peptides move beyond cancer: PET imaging of delayed-type hypersensitivity reaction. J Nucl Med. 2005;46:2–4.
81. Beer AJ, Haubner R, Goebel M, et al. Biodistribution and pharmacokinetics of the [alpha] v [beta]3-selective tracer 18F-galacto-RGD in cancer patients. J Nucl Med. 2005;46:1333–41.
82. Machac J. Cardiac positron emission tomography imaging. Semin Nucl Med. 2005;35:17–36.
83. Saha GB, Macintyre WJ, Go RT. Radiopharmaceuticals for brain imaging. Semin Nucl Med. 1994;24:324–49.
84. Schuster DP. The evaluation of lung function with PET. Semin Nucl Med. 1998;28:341–51.
85. Anderson H, Price P. Clinical measurement of blood flow in tumours using positron emission tomography: a review. Nucl Med Commun. 2002;23:131–8.
86. Bacharach SL, Libutti SK, Carrasquillo JA. Measuring tumor blood flow with (H_2O)-O-15: practical considerations. Nucl Med Biol. 2000;27:671–6.
87. Bruehlmeier M, Roelcke U, Schubiger PA, Ametamey SM. Assessment of hypoxia and perfusion in human brain tumors using PET with F-18-fluoromisonidazole and O-15-H_2O. J Nucl Med. 2004;45:1851–9.
88. Lassen U, Andersen P, Daugaard G, et al. Metabolic and hemodynamic evaluation of brain metastases from small cell lung cancer with positron emission tomography. Clin Cancer Res. 1998;4: 2591–7.
89. Beaney RP, Jones T, Lammertsma AA, McKenzie CG, Halnan KE. Positron emission tomography for in vivo measurement of regional blood-flow, oxygen utilization, and blood-volume in patients with breast carcinoma. Lancet. 1984;1:131–4.
90. Hentschel M, Paulus T, Mix M, Moser E, Nitzsche EU, Brink I. Analysis of blood flow and glucose metabolism in mammary carcinomas and normal breast: a (H_2O)-O-15 PET and F-18-FDG PET study. Nucl Med Commun. 2007;28:789–97.
91. Wilson C, Lammertsma AA, McKenzie CG, Sikora K, Jones T. Measurements of blood-flow and exchanging water space in breast tumors using positron emission tomography—a rapid and noninvasive dynamic method. Cancer Res. 1992;52:1592–7.
92. Anderson H, Yap JT, Wells P, et al. Measurement of renal tumour and normal tissue perfusion using positron emission tomography in a phase II clinical trial of razoxane. Br J Cancer. 2003;89:262–7.
93. Wells P, Jones T, Price P. Assessment of inter- and intrapatient variability in (CO_2)-O-15 positron emission tomography measurements of blood flow in patients with intra-abdominal cancers. Clin Cancer Res. 2003;9:6350–6.
94. Yamaguchi A, Taniguchi H, Kunishima S, Koh T, Yamagishi H. Correlation between angiographically assessed vascularity and blood flow in hepatic metastases in patients with colorectal carcinoma. Cancer. 2000;89:1236–44.
95. Hoekstra CJ, Stroobants SG, Hoekstra OS, Smit EF, Vansteenkiste JF, Lammertsma AA. Measurement of perfusion in stage IIIA-N2 non-small cell lung cancer using (H_2O)-O-15 and positron emission tomography. Clin Cancer Res. 2002;8:2109–15.
96. de Langen AJ, Lubberink M, Boellaard R, et al. Reproducibility of tumor perfusion measurements using O-15-labeled water and PET. J Nucl Med. 2008;49:1763–8.
97. de Langen AJ, van den Boogaart VEM, Marcus JT, Lubberink M. Use of (H_2O)-O-15-PET and DCE-MRI to measure tumor blood flow. Oncologist. 2008;13:631–44.
98. Herbst RS, Mullani NA, Davis DW, et al. Development of biologic markers of response and assessment of antiangiogenic activity in a clinical trial of human recombinant endostatin. J Clin Oncol. 2002;20:3804–14.
99. Mankoff DA, Dunnwald LK, Gralow JR, et al. Blood flow and metabolism in locally advanced breast cancer: relationship to response to therapy. J Nucl Med. 2002;43:500–9.
100. Anderson HL, Yap JT, Miller MP, Robbins A, Jones T, Price PM. Assessment of pharmacodynamic vascular response in a phase I trial of combretastatin A4 phosphate. J Clin Oncol. 2003;21: 2823–30.
101. Mathias CJ, Welch MJ, Raichle ME, et al. Evaluation of a potential generator-produced PET tracer for cerebral perfusion imaging—single-pass cerebral extraction measurements and imaging with radiolabeled Cu-PTSM. J Nucl Med. 1990;31:351–9.
102. Blower PJ, Lewis JS, Zweit J. Copper radionuclides and radiopharmaceuticals in nuclear medicine. Nucl Med Biol. 1996;23: 957–80.

103. Wallhaus TR, Lacy J, Whang J, Green MA, Nickles RJ, Stone CK. Human biodistribution and dosimetry of the PET perfusion agent copper-62-PTSM. J Nucl Med. 1998;39:1958–64.
104. Flower MA, Zweit J, Hall AD, et al. Cu-62-PTSM and PET used for the assessment of angiotensin II-induced blood flow changes in patients with colorectal liver metastases. Eur J Nucl Med. 2001;28:99–103.
105. Mathias CJ, Green MA, Morrison WB, Knapp DW. Evaluation of Cu-PTSM as a tracer of tumor perfusion—comparison with labeled microspheres in a spontaneous canine neoplasms. Nucl Med Biol. 1994;21:83–7.
106. Mathias CJ, Welch MJ, Perry DJ, et al. Investigation of copper-PTSM as a PET tracer for tumor blood-flow. Nucl Med Biol. 1991;18:807–11.
107. Mathias CJ, Bergmann SR, Green MA. Species-dependent binding of copper(II) bis(thiosemicarbazone) radiopharmaceuticals to serum albumin. J Nucl Med. 1995;36:1451–5.
108. Green MA, Mathias CJ, Willis LR, et al. Assessment of Cu-ETS as a PET radiopharmaceutical for evaluation of regional renal perfusion. Nucl Med Biol. 2007;34:247–55.
109. Holland JP, Aigbirhio FI, Betts HM, et al. Functionalized bis(thiosemicarbazonato) complexes of zinc and copper: synthetic platforms toward site-specific radiopharmaceuticals. Inorg Chem. 2007;46:465–85.
110. Bengel FM, Higuchi T, Javadi MS, Lautamaki R. Cardiac positron emission tomography. J Am Coll Cardiol. 2009;54:1–15.
111. Zhang XS, Wu XJ, Zhang Y, Chen WA. N-13-NH3: a selective contrast-enhancing tracer for brain tumor. Nucl Med Commun. 2008;29:1052–8.
112. Brown JM. The hypoxic cell: a target for selective cancer therapy-eighteenth Bruce F. Cain memorial award lecture. Cancer Res. 1999;59:5863–70.
113. Tatum JL, Kelloff GJ, Gillies RJ, et al. Hypoxia: importance in tumor biology, noninvasive measurement by imaging, and value of its measurement in the management of cancer therapy. Int J Radiat Biol. 2006;82:699–757.
114. Hockel M, Schlenger K, Aral B, Mitze M, Schaffer U, Vaupel P. Association between tumor hypoxia and malignant progression in advanced cancer of the uterine cervix. Cancer Res. 1996;56:4509–15.
115. Graeber TG, Osmanian C, Jacks T, et al. Hypoxia-mediated selection of cells with diminished apoptotic potential in solid tumours. Nature. 1996;379:88–91.
116. Crabtree HG, Cramer W. Action of radium on cancer cells. I. Effects of hydrocyanic acid, iodoacetic acid and sodium fluoride on the metabolism and transplantability of cancer cells. Proc Roy Soc. 1933;B113:226–38.
117. Brown JM, Giaccia AJ. The unique physiology of solid tumors: opportunities (and problems) for cancer therapy. Cancer Res. 1998;58:1408–16.
118. Thomlinson RH, Gray LH. The histological structure of some human lung cancers and the possible implications for radiotherapy. Br J Cancer. 1955;9:539–49.
119. Gray LH, Conger AD, Ebert M, Hornsey S, Scott OCA. The concentration of oxygen dissolved in tissues at the time of irradiation as a factor in radiotherapy. Br J Radiol. 1953;26:638–48.
120. Heacock CS, Sutherland RM. Induction characteristics of oxygen regulated proteins. Int J Radiat Oncol Biol Phys. 1986;12:1287–90.
121. Hodgkiss RJ. Use of 2-nitroimidazoles as bioreductive markers for tumor hypoxia. Anticancer Drug Des. 1998;13:687–702.
122. Holland JP, Barnard PJ, Collison D, et al. Spectroelectrochemical and computational studies on the mechanism of hypoxia selectivity of copper radiopharmaceuticals. Chemistry. 2008;14:5890–907.
123. Dearling JLJ, Lewis JS, Mullen GED, Welch MJ, Blower PJ. Copper bis(thiosemicarbazone) complexes as hypoxia imaging agents: structure-activity relationships. J Biol Inorg Chem. 2002;7:249–59.
124. O'Donoghue JA, Zanzonico P, Pugachev A, et al. Assessment of regional tumor hypoxia using ^{18}F-fluoromisonidazole and ^{64}Cu(II)-diacetyl-bis(N4-methylthiosemicarbazone) positron emission tomography: comparative study featuring microPET imaging, P2 probe measurement, autoradiography, and fluorescent microscopy in the R3327-AT and FaDu rat tumor models. Int J Radiat Oncol Biol Phys. 2005;61:1493–502.
125. Holland JP, Lewis Jason S, Dehdashti F. Assessing tumor hypoxia by positron emission tomography with Cu-ATSM. Q J Nucl Med Mol Imaging. 2009;53:193–200.
126. Dehdashti F, Grigsby PW, Lewis JS, Laforest R, Siegel BA, Welch M. Assessing tumor hypoxia in cervical cancer by PET with ^{60}Cu-labeled diacetyl-bis (N4-emthylthiosemicarbazone). J Nucl Med. 2008;49:201–5.
127. Dehdashti F, Mintun MA, Lewis JS, et al. In vivo assessment of tumor hypoxia in lung cancer with ^{60}Cu-ATSM. Eur J Nucl Med Mol Imaging. 2003;30:844–50.
128. Yuan H, Schroeder T, Bowsher JE, Hedlund LW, Wong T, Dewhirst MW. Intertumoral differences in hypoxia selectivity of the PET imaging agent ^{64}Cu(II)-diacetyl-Bis(N4-methylthiosemicarbazone). J Nucl Med. 2006;47:989–98.
129. Dehdashti F, Grigsby Perry W, Mintun Mark A, Lewis Jason S, Siegel Barry A, Welch Michael J. Assessing tumor hypoxia in cervical cancer by positron emission tomography with ^{60}Cu-ATSM: relationship to therapeutic response-a preliminary report. Int J Radiat Oncol Biol Phys. 2003;55:1233–8.
130. Vavere AL, Lewis JS. Cu-ATSM: a radiopharmaceutical for the PET imaging of hypoxia. Dalton Trans. 2007;4:4893–902.
131. Burgman P, O'Donoghue JA, Lewis JS, Welch MJ, Humm JL, Ling CC. Cell line-dependent differences in uptake and retention of the hypoxia-selective nuclear imaging agent Cu-ATSM. Nucl Med Biol. 2005;32:623–30.
132. Takahashi N, Fujibayashi Y, Yonekura Y, et al. Evaluation of ^{62}Cu labeled diacetyl bis(N^4-methylthiosemicarbazone) in hypoxic tissue in patients with lung cancer. Ann Nucl Med. 2000;14:323–8.
133. Chen DL, Dehdashti F. Advances in positron emission tomographic imaging of lung cancer. Proc Am Thorac Soc. 2005;2:541–4.
134. Lewis JS, Laforest R, Buettner TL, et al. Copper-64-diacetyl-bis(N4-methylthiosemicarbazone): an agent for radiotherapy. Proc Natl Acad Sci USA. 2001;98:1206–11.
135. Jurisson S, Lydon J. Potential technetium small molecule radiopharmaceuticals. Chem Rev. 1999;99:2205–18.
136. Cutler CS, Lewis JS, Anderson CJ. Utilization of metabolic, transport and receptor-mediated processes to deliver agents for cancer diagnosis. Adv Drug Deliv Rev. 1999;37:189–211.
137. Hagooly A, Rossin R, Welch MJ. Small molecule receptors as imaging targets. In: Semmler W, Shwaiger M, editors. Handbook of experimental pharmacology. Berlin: Springer; 2008. p. 93–129.
138. Rowland DJ, Tu Z, Xu J, Ponde D, Mach RH, Welch MJ. Synthesis and in vivo evaluation of 2 high-affinity ^{76}Br-labeled {sigma}2-receptor ligands. J Nucl Med. 2006;47:1041–8.
139. Mathias CJ, Lewis MR, Reichert DE, et al. Preparation of ^{66}Ga- and ^{68}Ga-labeled Ga(III)-deferoxamine-folate as potential folate-receptor-targeted PET radiopharmaceuticals. Nucl Med Biol. 2003;30:725–31.
140. Vallabhajosula S. ^{18}F-Labeled positron emission tomographic radiopharmaceuticals in oncology: an overview of radiochemistry and mechanisms of tumor localization. Semin Nucl Med. 2007;37:400–19.
141. Mankoff DA, Shields AF, Krohn KA. PET imaging of cellular proliferation. Radiol Clin North Am. 2005;43:153–67.
142. Kiesewetter DO, Kilbourn MR, Landvatter SW, Heiman DF, Katzenellenbogen JA, Welch MJ. Preparation of four fluorine-18-labeled estrogens and their selective uptakes in target tissues of immature rats. J Nucl Med. 1984;25:1212–21.

143. Kumar P, Mercer J, Doerkson C, Tonkin K, McEwan AJB. Clinical production, stability studies and PET imaging with 16-alpha-[^{18}F]fluoroestradiol ([^{18}F]FES) in ER positive breast cancer patients. J Pharm Pharm Sci. 2007;10:256s–65s.
144. Mintun MA, Welch MJ, Siegel BA, et al. Breast cancer—PET imaging of estrogen receptors. Radiology. 1988;169:45–8.
145. Dehdashti F, Mortimer J, Trinkaus K, et al. PET-based estradiol challenge as a predictive biomarker of response to endocrine therapy in women with estrogen-receptor-positive breast cancer. Breast Cancer Res Treat. 2009;113:509–17.
146. Seimbille Y, Ali H, van Lier JE. Synthesis of 2,16 alpha- and 4,16 alpha-difluoroestradiols and their 11 beta-methoxy derivatives as potential estrogen receptor-binding radiopharmaceuticals. J Chem Soc Perkin Trans. 2002;1:657–63.
147. VanBrocklin HF, Rocque PA, Lee HV, Carlson KE, Katzenellenbogen JA, Welch MJ. 16[beta]-[^{18}F]fluoromoxestrol: a potent, metabolically stable positron emission tomography imaging agent for estrogen receptor positive human breast tumors. Life Sci. 1993;53:811–9.
148. Larson SM, Morris M, Gunther I, et al. Tumor localization of 16{beta}-^{18}F-fluoro-5{alpha}-dihydrotestosterone versus [^{18}F] FDG in patients with progressive, metastatic prostate cancer. J Nucl Med. 2004;45:366–73.
149. Zanzonico PB, Finn R, Pentlow KS, et al. PET-based radiation dosimetry in man of ^{18}F-fluorodihydrotestosterone, a new radiotracer for imaging prostate cancer. J Nucl Med. 2004;45:1966–71.
150. Kuhajda FP. Fatty acid synthase and cancer: new application of an old pathway. Cancer Res. 2006;66:5977–80.
151. Glunde K, Bhujwalla ZM. Choline kinase alpha in cancer prognosis and treatment. Lancet Oncol. 2007;8:855–7.
152. Halestrap AP, Price NT. The proton-linked monocarboxylate transporter (MCT) family: structure, function and regulation. Biochem J. 1999;343(Pt 2):281–99.
153. Hara T, Kosaka N, Kishi H. PET imaging of prostate cancer using carbon-11-choline. J Nucl Med. 1998;39:990–5.
154. DeGrado TR, Baldwin SW, Wang S, et al. Synthesis and evaluation of ^{18}F-labeled choline analogs as oncologic PET tracers. J Nucl Med. 2001;42:1805–14.
155. Hara T, Kosaka N, Kishi H. Development of ^{18}F-fluoroethylcholine for cancer imaging with PET: synthesis, biochemistry, and prostate cancer imaging. J Nucl Med. 2002;43:187–99.
156. Bansal A, Shuyan W, Hara T, Harris RA, Degrado TR. Biodisposition and metabolism of [^{18}F]fluorocholine in 9L glioma cells and 9L glioma-bearing fisher rats. Eur J Nucl Med Mol Imaging. 2008;35:1192–203.
157. Henriksen G, Herz M, Hauser A, Schwaiger M, Wester HJ. Synthesis and preclinical evaluation of the choline transport tracer deshydroxy-[^{18}F]fluorocholine ([^{18}F]dOC). Nucl Med Biol. 2004;31:851–8.
158. Ng CK, Huang SC, Schelbert HR, Buxton DB. Validation of a model for [1-^{11}C]acetate as a tracer of cardiac oxidative metabolism. Am J Physiol. 1994;266:H1304–15.
159. Shreve P, Chiao PC, Humes HD, Schwaiger M, Gross MD. Carbon-11-acetate PET imaging in renal disease. J Nucl Med. 1995;36:1595–601.
160. Vavere AL, Kridel SJ, Wheeler FB, Lewis JS. 1-^{11}C-acetate as a PET radiopharmaceutical for imaging fatty acid synthase expression in prostate cancer. J Nucl Med. 2008;49:327–34.
161. Kwock L, Smith JK, Castillo M, et al. Clinical role of proton magnetic resonance spectroscopy in oncology: brain, breast, and prostate cancer. Lancet Oncol. 2006;7:859–68.
162. Schoder H, Herrmann K, Gonen M, et al. 2-[^{18}F]fluoro-2-deoxyglucose positron emission tomography for the detection of disease in patients with prostate-specific antigen relapse after radical prostatectomy. Clin Cancer Res. 2005;11:4761–9.
163. Giovacchini G, Picchio M, Coradeschi E, et al. [^{11}C]choline uptake with PET/CT for the initial diagnosis of prostate cancer: relation to PSA levels, tumour stage and anti-androgenic therapy. Eur J Nucl Med Mol Imaging. 2008;35:1065–73.
164. Krause BJ, Souvatzoglou M, Tuncel M, et al. The detection rate of [^{11}C]choline-PET/CT depends on the serum PSA-value in patients with biochemical recurrence of prostate cancer. Eur J Nucl Med Mol Imaging. 2008;35:18–23.
165. McGivan JD, Pastor-Anglada M. Regulatory and molecular aspects of mammalian amino acid transport. Biochem J. 1994;299(Pt 2):321–34.
166. Sang J, Lim YP, Panzica M, Finch P, Thompson NL. TA1, a highly conserved oncofetal complementary DNA from rat hepatoma, encodes an integral membrane protein associated with liver development, carcinogenesis, and cell activation. Cancer Res. 1995;55:1152–9.
167. Asano S, Kameyama M, Oura A, et al. L-type amino acid transporter-1 expressed in human astrocytomas, U343MGa. Biol Pharm Bull. 2007;30:415–22.
168. Kondoh N, Imazeki N, Arai M, et al. Activation of a system A amino acid transporter, ATA1/SLC38A1, in human hepatocellular carcinoma and preneoplastic liver tissues. Int J Oncol. 2007;31:81–7.
169. Nawashiro H, Otani N, Shinomiya N, et al. L-type amino acid transporter 1 as a potential molecular target in human astrocytic tumors. Int J Cancer. 2006;119:484–92.
170. Nakanishi K, Ogata S, Matsuo H, et al. Expression of LAT1 predicts risk of progression of transitional cell carcinoma of the upper urinary tract. Virchows Arch. 2007;451:681–90.
171. Ishiwata K, Kubota K, Murakami M, et al. Re-evaluation of amino acid PET studies: can the protein synthesis rates in brain and tumor tissues be measured in vivo? J Nucl Med. 1993;34:1936–43.
172. Becherer A, Karanikas G, Szabo M, et al. Brain tumour imaging with PET: a comparison between [^{18}F]fluorodopa and [^{11}C]methionine. Eur J Nucl Med Mol Imaging. 2003;30:1561–7.
173. Plathow C, Weber WA. Tumor cell metabolism imaging. J Nucl Med. 2008;49 Suppl 2:43S–63S.
174. Sutinen E, Jyrkkio S, Gronroos T, Haaparanta M, Lehikoinen P, Nagren K. Biodistribution of [^{11}C] methylaminoisobutyric acid, a tracer for PET studies on system A amino acid transport in vivo. Eur J Nucl Med. 2001;28:847–54.
175. Tolvanen T, Nagren K, Yu M, et al. Human radiation dosimetry of [11C]MeAIB, a new tracer for imaging of system A amino acid transport. Eur J Nucl Med Mol Imaging. 2006;33:1178–84.
176. Sutinen E, Jyrkkio S, Alanen K, Nagren K, Minn H. Uptake of [N-methyl-^{11}C]alpha-methylaminoisobutyric acid in untreated head and neck cancer studied by PET. Eur J Nucl Med Mol Imaging. 2003;30:72–7.
177. Langen KJ, Jarosch M, Muhlensiepen H, et al. Comparison of fluorotyrosines and methionine uptake in F98 rat gliomas. Nucl Med Biol. 2003;30:501–8.
178. Langen KJ, Hamacher K, Weckesser M, et al. O-(2-[^{18}F]fluoroethyl)-L-tyrosine: uptake mechanisms and clinical applications. Nucl Med Biol. 2006;33:287–94.
179. Oka S, Hattori R, Kurosaki F, et al. A preliminary study of anti-1-amino-3-^{18}F-fluorocyclobutyl-1-carboxylic acid for the detection of prostate cancer. J Nucl Med. 2007;48:46–55.
180. Langen KJ, Ziemons K, Kiwit JC, et al. 3-[^{123}I]iodo-alpha-methyl-tyrosine and [methyl-^{11}C]-L-methionine uptake in cerebral gliomas: a comparative study using SPECT and PET. J Nucl Med. 1997;38:517–22.
181. Deloar HM, Fujiwara T, Nakamura T, et al. Estimation of internal absorbed dose of L-[methyl-^{11}C]methionine using whole-body positron emission tomography. Eur J Nucl Med. 1998;25:629–33.
182. Floeth FW, Pauleit D, Sabel M, et al. ^{18}F-FET PET differentiation of ring-enhancing brain lesions. J Nucl Med. 2006;47:776–82.

183. Nunez R, Macapinlac HA, Yeung HW, et al. Combined [^{18}F]FDG and ^{11}C-methionine PET scans in patients with newly progressive metastatic prostate cancer. J Nucl Med. 2002;43:46–55.
184. Schuster DM, Votaw JR, Nieh PT, et al. Initial experience with the radiotracer anti-1-amino-3-^{18}F-fluorocyclobutane-1-carboxylic acid with PET/CT in prostate carcinoma. J Nucl Med. 2007;48:56–63.
185. Kaira K, Oriuchi N, Otani Y, et al. Fluorine-18-alpha-methyltyrosine positron emission tomography for diagnosis and staging of lung cancer: a clinicopathologic study. Clin Cancer Res. 2007;13:6369–78.
186. Pirotte B, Goldman S, Massager N, et al. Comparison of [^{18}F]FDG and ^{11}C-methionine for PET-guided stereotactic brain biopsy of gliomas. J Nucl Med. 2004;45:1293–8.
187. Van Laere K, Ceyssens S, Van Calenbergh F, et al. Direct comparison of [^{18}F]FDG and ^{11}C-methionine PET in suspected recurrence of glioma: sensitivity, inter-observer variability and prognostic value. Eur J Nucl Med Mol Imaging. 2005;32:39–51.
188. Grosu AL, Piert M, Weber WA, et al. Positron emission tomography for radiation treatment planning. Strahlenther Onkol. 2005;181:483–99.
189. Bergstrom M, Collins VP, Ehrin E, et al. Discrepancies in brain tumor extent as shown by computed tomography and positron emission tomography using [^{68}Ga]EDTA, [^{11}C]glucose, and [^{11}C] methionine. J Comput Assist Tomogr. 1983;7:1062–6.
190. Kracht LW, Miletic H, Busch S, et al. Delineation of brain tumor extent with [^{11}C] L-methionine positron emission tomography: local comparison with stereotactic histopathology. Clin Cancer Res. 2004;10:7163–70.
191. Pauleit D, Floeth F, Hamacher K, et al. O-(2-[^{18}F]fluoroethyl)-L-tyrosine PET combined with MRI improves the diagnostic assessment of cerebral gliomas. Brain. 2005;128:678–87.
192. Grosu AL, Weber WA, Franz M, et al. Reirradiation of recurrent high-grade gliomas using amino acid PET (SPECT)/CT/MRI image fusion to determine gross tumor volume for stereotactic fractionated radiotherapy. Int J Radiat Oncol Biol Phys. 2005;63:511–9.
193. Kenny LM, Aboagye EO, Price PM. Positron emission tomography imaging of cell proliferation in oncology. Clin Oncol. 2004;16:176–85.
194. Toyohara J, Fujibayashi Y. Trends in nucleoside tracers for PET imaging of cell proliferation. Nucl Med Biol. 2003;30:681–5.
195. Nimmagadda S, Shields A. The role of DNA synthesis imaging in cancer in the era of targeted therapeutics. Cancer Metastasis Rev. 2008;27:575–87.
196. Schwartz JL, Tamura Y, Jordan R, Grierson JR, Krohn KA. Monitoring tumor cell proliferation by targeting DNA synthetic processes with thymidine and thymidine analogs. J Nucl Med. 2003;44:2027–32.
197. Christman D, Crawford EJ, Friedkin M, Wolf AP. Detection of DNA-synthesis in intact organisms with positron-emitting methyl-C-11 thymidine. Proc Natl Acad Sci USA. 1972;69:988–92.
198. Mach RH, Dehdashti F, Wheeler KT. PET radiotracers for imaging the proliferative status of solid tumors. PET Clin. 2009; 4:1–15.
199. Conti PS, Hilton J, Wong DF, et al. High performance liquid chromatography of carbon-11 labeled thymidine and its major catabolites for clinical PET studies. Nucl Med Biol. 1994;21:1045–51.
200. Bading JR, Shields AF. Imaging of cell proliferation: status and prospects. J Nucl Med. 2008;49:64S–80S.
201. Dunphy MPS, Lewis JS. Radiopharmaceuticals in preclinical and clinical development for monitoring of therapy with PET. J Nucl Med. 2009;50:106S–21S.
202. Reubi JC. Peptide receptors as molecular targets for cancer diagnosis and therapy. Endocr Rev. 2003;24:389–427.
203. Meisetschlager G, Poethko T, Stahl A, et al. Gluc-Lys([^{18}F]FP)-TOCA PET in patients with SSTR-positive tumors: biodistribution and diagnostic evaluation compared with [^{111}In] DTPA-octreotide. J Nucl Med. 2006;47:566–73.
204. Zhang H, Chen J, Waldherr C, et al. Synthesis and evaluation of bombesin derivatives on the basis of pan-bombesin peptides labeled with indium-111, lutetium-177, and yttrium-90 for targeting bombesin receptor-expressing tumors. Cancer Res. 2004;64:6707–15.
205. Haubner R, Kuhnast B, Mang C, et al. [^{18}F]Galacto-RGD: synthesis, radiolabeling, metabolic stability, and radiation dose estimates. Bioconjug Chem. 2004;15:61–9.
206. Froidevaux S, Eberle AN, Christe M, et al. Neuroendocrine tumor targeting: study of novel gallium-labeled somatostatin radiopeptides in a rat pancreatic tumor model. Int J Cancer. 2002;98:930–7.
207. Prasanphanich AF, Nanda PK, Rold TL, et al. [^{64}Cu-NOTA-8-Aoc-BBN(7-14)NH_2] targeting vector for positron-emission tomography imaging of gastrin-releasing peptide receptor-expressing tissues. Proc Natl Acad Sci USA. 2007;104:12462–7.
208. de Jong M, Breeman WA, Bakker WH, et al. Comparison of ^{111}In-labeled somatostatin analogues for tumor scintigraphy and radionuclide therapy. Cancer Res. 1998;58:437–41.
209. Wester HJ, Schottelius M, Scheidhauer K, et al. PET imaging of somatostatin receptors: design, synthesis and preclinical evaluation of a novel F-18-labelled, carbohydrated analogue of octreotide. Eur J Nucl Med Mol Imaging. 2003;30:117–22.
210. Haubner R, Wester HJ, Burkhart F, et al. Glycosylated RGD-containing peptides: tracer for tumor targeting and angiogenesis imaging with improved biokinetics. J Nucl Med. 2001;42:326–36.
211. Wu Z, Li ZB, Chen K, et al. microPET of tumor integrin $alpha_v beta_3$ expression using ^{18}F-labeled PEGylated tetrameric RGD peptide (^{18}F-FPRGD4). J Nucl Med. 2007;48:1536–44.
212. Antunes P, Ginj M, Walter MA, Chen J, Reubi JC, Maecke HR. Influence of different spacers on the biological profile of a DOTA-somatostatin analogue. Bioconjug Chem. 2007;18:84–92.
213. Jia B, Liu Z, Shi J, et al. Linker effects on biological properties of ^{111}In-labeled DTPA conjugates of a cyclic RGDfK dimer. Bioconjug Chem. 2008;19:201–10.
214. Garrison JC, Rold TL, Sieckman GL, et al. Evaluation of the pharmacokinetic effects of various linking group using the ^{111}In-DOTA-X-BBN(7-14)NH_2 structural paradigm in a prostate cancer model. Bioconjug Chem. 2008;19:1803–12.
215. Parry JJ, Kelly TS, Andrews R, Rogers BE. In vitro and in vivo evaluation of ^{64}Cu-labeled DOTA-linker-bombesin(7-14) analogues containing different amino acid linker moieties. Bioconjug Chem. 2007;18:1110–7.
216. Schottelius M, Wester HJ. Molecular imaging targeting peptide receptors. Methods. 2009;48:161–77.
217. Rolleman EJ, Kooij PP, de Herder WW, Valkema R, Krenning EP, de Jong M. Somatostatin receptor subtype 2-mediated uptake of radiolabelled somatostatin analogues in the human kidney. Eur J Nucl Med Mol Imaging. 2007;34:1854–60.
218. Huerta S, Goulet EJ, Huerta-Yepez S, Livingston EH. Screening and detection of apoptosis. J Surg Res. 2007;139:143–56.
219. Gottlieb RA. Part III: molecular and cellular hematology apoptosis. In: Lichtman MA, Beutler E, Kipps TJ, editors. Williams hematology. 7th ed. New York: McGraw-Hill Book Co; 2007. p. 125–30.
220. Yang MY, Chuang H, Chen RF, Yang KD. Reversible phosphatidylserine expression on blood granulocytes related to membrane perturbation but not DNA strand breaks. J Leukoc Biol. 2002;71:231–7.
221. Boersma HH, Kietselaer BL, Stolk LM, et al. Past, present, and future of annexin A5: from protein discovery to clinical applications. J Nucl Med. 2005;46:2035–50.

222. Munoz LE, Franz S, Pausch F, et al. The influence on the immunomodulatory effects of dying and dead cells of Annexin V. J Leukoc Biol. 2007;81:6–14.
223. Blankenberg FG. In vivo detection of apoptosis. J Nucl Med. 2008;49 Suppl 2:81S–95S.
224. Belhocine T, Steinmetz N, Hustinx R, et al. Increased uptake of the apoptosis-imaging agent ^{99m}Tc recombinant human Annexin V in human tumors after one course of chemotherapy as a predictor of tumor response and patient prognosis. Clin Cancer Res. 2002;8:2766–74.
225. Kemerink GJ, Liu X, Kieffer D, et al. Safety, biodistribution, and dosimetry of ^{99m}Tc-HYNIC-annexin V, a novel human recombinant annexin V for human application. J Nucl Med. 2003;44: 947–52.
226. Boersma HH, Liem IH, Kemerink GJ, et al. Comparison between human pharmacokinetics and imaging properties of two conjugation methods for ^{99m}Tc-annexin A5. Br J Radiol. 2003;76: 553–60.
227. Rottey S, Slegers G, Van Belle S, Goethals I, Van de Wiele C. Sequential ^{99m}Tc-hydrazinonicotinamide-annexin V imaging for predicting response to chemotherapy. J Nucl Med. 2006;47: 1813–8.
228. Belhocine T, Steinmetz N, Li C, Green A, Blankenberg FG. The imaging of apoptosis with the radiolabeled annexin V: optimal timing for clinical feasibility. Technol Cancer Res Treat. 2004;3:23–32.
229. van de Wiele C, Lahorte C, Vermeersch H, et al. Quantitative tumor apoptosis imaging using technetium-99m-HYNIC annexin V single photon emission computed tomography. J Clin Oncol. 2003;21:3483–7.
230. Tait JF, Brown DS, Gibson DF, Blankenberg FG, Strauss HW. Development and characterization of annexin V mutants with endogenous chelation sites for ^{99m}Tc. Bioconjug Chem. 2000;11: 918–25.
231. Tait JF, Smith C, Blankenberg FG. Structural requirements for in vivo detection of cell death with ^{99m}Tc-annexin V. J Nucl Med. 2005;46:807–15.
232. Himmelweit F. The collected papers of Paul Ehrlich. Immunology and cancer research, vol. 2. London: Pergamon; 1960.
233. Kohler G, Milstein C. Continuous cultures of fused cells secreting antibody of predefined specificity. Nature. 1975;256:495–7.
234. Wu AM, Senter PD. Arming antibodies: prospects and challenges for immunoconjugates. Nat Biotechnol. 2005;23:1137–46.
235. Kenanova V, Wu AM. Tailoring antibodies for radionuclide delivery. Exp Opin Drug Delivery. 2006;3:53–70.
236. Reilly RM. The immunoreactivity of radiolabeled antibodies—its impact on tumor targeting and strategies for preservation. Cancer Biother Radiopharm. 2004;19:669–72.
237. Lindmo T, Boven E, Cuttitta F, Fedorko J, Bunn Jr PA. Determination of the immunoreactive fraction of radiolabeled monoclonal antibodies by linear extrapolation to binding at infinite antigen excess. J Immunol Methods. 1984;72:77–89.
238. Lindmo T, Bunn Jr PA. Determination of the true immunoreactive fraction of monoclonal antibodies after radiolabeling. Methods Enzymol. 1986;121:678–91.
239. Konishi S, Hamacher K, Vallabhajosula S, et al. Determination of immunoreactive fraction of radiolabeled monoclonal antibodies: what is an appropriate method? Cancer Biother Radiopharm. 2004;19:706–15.
240. Anderson CJ, Connett JM, Schwarz SW, et al. Copper-64-labeled antibodies for PET imaging. J Nucl Med. 1992;33:1685–90.
241. Anderson CJ, Schwarz SW, Connett JM, et al. Preparation, biodistribution and dosimetry of copper-64-labeled anti-colorectal carcinoma monoclonal antibody fragments 1A3-F(ab')$_2$. J Nucl Med. 1995;36:850–8.
242. Saijo N. What are the reasons for negative phase III trials of molecular-target-based drugs? Cancer Sci. 2004;95:772–6.
243. Wu AM. Antibodies and antimatter: the resurgence of immuno-PET. J Nucl Med. 2009;50:2–5.
244. http://www.clinicaltrials.gov. Accessed 15 Oct 2009.
245. Philpott GW, Schwarz SW, Anderson CJ, et al. RadioimmunoPET: detection of colorectal carcinoma with positron-emitting copper-64-labeled monoclonal antibody. J Nucl Med. 1995;36: 1818–24.
246. Anderson CJ, Connett JM, Schwarz SW, et al. Copper-64-labeled antibodies for PET imaging. J Nucl Med. 1992;33:1685–91.
247. Philpott GW, Siegel BA, Schwarz SW, et al. Immunoscintigraphy with a new indium-111-labeled monoclonal antibody (MAb 1A3) in patients with colorectal cancer. Dis Colon Rectum. 1994;37:782–92.
248. Connett JM, Anderson CJ, Guo LW, et al. Radioimmunotherapy with a ^{64}Cu-labeled monoclonal antibody: a comparison with ^{67}Cu. Proc Natl Acad Sci USA. 1996;93:6814–8.
249. Perk LR, Visser OJ, Stigter-van Walsum M, et al. Preparation and evaluation of ^{89}Zr-Zevalin for monitoring of ^{90}Y-Zevalin biodistribution with positron emission tomography. Eur J Nucl Med Mol Imaging. 2006;33:1337–45.
250. Nagengast WB, de Vries EG, Hospers GA, et al. In vivo VEGF imaging with radiolabeled bevacizumab in a human ovarian tumor xenograft. J Nucl Med. 2007;48:1313–9.
251. Meijs WE, Haisma HJ, Klok RP, et al. Zirconium-labeled monoclonal antibodies and their distribution in tumor-bearing nude mice. J Nucl Med. 1997;38:112–8.
252. Perk LR, Vosjan MJWD, Visser GWM, et al. Isothiocyanatobenzyl-desferrioxamine: a new bifunctional chelate for facile radiolabeling of monoclonal antibodies with zirconium 89 for immuno-PET imaging Eur J Nucl Med Mol Imaging 2010;37:250–259.
253. Divgi CR, Pandit-Taskar N, Jungbluth AA, et al. Preoperative characterisation of clear-cell renal carcinoma using iodine-124-labelled antibody chimeric G250 (^{124}I-cG250) and PET in patients with renal masses: a phase I trial. Lancet Oncol. 2007;8:304–10.
254. Milenic DE, Brady ED, Brechbiel MW. Antibody-targeted radiation cancer therapy. Nat Rev Drug Discov. 2004;3:488–98.
255. McDevitt MR, Ma D, Simon J, Frank RK, Scheinberg DA. Design and synthesis of 225Ac radioimmunopharmaceuticals. Appl Radiat Isot. 2002;57:841–7.
256. Abe K, Sasaki M, Kuwabara Y, et al. Comparison of ^{18}FDG-PET with Tc-99m-HMDP scintigraphy for the detection of bone metastases in patients with breast cancer. Ann Nucl Med. 2005;19:573–9.
257. Adler LP, Faulhaber PF, Schnur KC, AlKasi NL, Shenk RR. Axillary lymph node metastases: screening with [F-18]2-deoxy-2-fluoro-D-glucose (FDG) PET. Radiology. 1997;203:323–7.
258. Avril N, Dose J, Janicke F, et al. Assessment of axillary lymph node involvement in breast cancer patients with positron emission tomography using radiolabeled 2-(fluorine-18)fluoro-2-deoxy-D-glucose. J Natl Cancer Inst. 1996;88:1204–9.
259. Amit A, Beck D, Lowenstein L, et al. The role of hybrid PET/CT in the evaluation of patients with cervical cancer. Gynecol Oncol. 2006;100:65–9.
260. Arulampalam T, Costa D, Visvikis D, Boulos P, Taylor I, Ell P. The impact of FDG-PET on the management algorithm for recurrent colorectal cancer. Eur J Nucl Med. 2001;28:1758–65.
261. Arulampalam THA, Francis DL, Visvikis D, Taylor I, Ell PJ. FDG-PET for the pre-operative evaluation of colorectal liver metastases. Eur J Surg Oncol. 2004;30:286–91.

262. Chen LB, Tong IL, Song HZ, Zhu H, Wang YC. F-18-DG PET/CT in detection of recurrence and metastasis of colorectal cancer. World J Gastroenterol. 2007;13:5025–9.
263. Abdel-Nabi H, Doerr RJ, Lamonica DM, et al. Staging of primary colorectal carcinomas with fluorine-18 fluorodeoxyglucose whole-body PET: correlation with histopathologic and CT findings. Radiology. 1998;206:755–60.
264. Adams S, Baum RP, Stuckensen T, Bitter K, Hor G. Prospective comparison of F-18-FDG PET with conventional imaging modalities (CT, MRI, US) in lymph node staging of head and neck cancer. Eur J Nucl Med. 1998;25:1255–60.
265. Akcali C, Zincirkeser S, Erbagcy Z, et al. Detection of metastases in patients with cutaneous melanoma using FDG-PET/CT. J Int Med Res. 2007;35:547–53.
266. Chang JTC, Chan SC, Yen TC, et al. Nasopharyngeal carcinoma staging by ^{18}F-fluorodeoxyglucose positron emission tomography. Int J Radiat Oncol Biol Phys. 2005;62:501–7.
267. Bury T, Barreto A, Daenen F, Barthelemy N, Ghaye B, Rigo P. Fluorine-18 deoxyglucose positron emission tomography for the detection of bone metastases in patients with non-small cell lung cancer. Eur J Nucl Med. 1998;25:1244–7.
268. Castellucci P, Perrone AM, Picchio M, et al. Diagnostic accuracy of F-18-FDG PET/CT in characterizing ovarian lesions and staging ovarian cancer: correlation with transvaginal ultrasonography, computed tomography, and histology. Nucl Med Commun. 2007;28:589–95.
260. Chang CH, Wu HC, Tsai JJP, Shen YY, Changlai SP, Kao A. Detecting metastatic pelvic lymph nodes by F-18-2-deoxyglucose positron emission tomography in patients with prostate-specific antigen relapse after treatment for localized prostate cancer. Urol Int. 2003;70:311–5.
270. Cermik TF, Mavi A, Acikgoz G, Houseni M, Dadparvar S, Alavi A. FDG PET in detecting primary and recurrent malignant salivary gland tumors. Clin Nucl Med. 2007;32:286–91.
271. Aide N, Cappele O, Bottet P, et al. Efficiency of [F-18]FDG PET in characterising renal cancer and detecting distant metastases: a comparison with CT. Eur J Nucl Med Mol Imaging. 2003;30: 1236–45.
272. Chang CH, Shiau YC, Shen YY, Kao A, Lin CC, Lee CC. Differentiating solitary pulmonary metastases in patients with renal cell carcinomas by F-18-fluoro-2-deoxyglucose positron emission tomography—a preliminary report. Urol Int. 2003; 71:306–9.
273. Chen J, Cheong JH, Yun MJ, et al. Improvement in preoperative staging of gastric adenocarcinoma with positron emission tomography. Cancer. 2005;103:2383–90.
274. Choi JY, Lee KH, Shim YM, et al. Improved detection of individual nodal involvement in squamous cell carcinoma of the esophagus by FDG PET. J Nucl Med. 2000;41:808–15.
275. Bennink RJ, van Tienhoven G, Rijks LJ, Noorduyn AL, Janssen AG, Sloof GW. In vivo prediction of response to antiestrogen treatment in estrogen receptor-positive breast cancer. J Nucl Med. 2004;45:1–7.
276. Caveliers V, Everaert H, John CS, Lahoutte T, Bossuyt A. Sigma receptor scintigraphy with N-[2-(1′-piperidinyl)ethyl]-3-^{123}I-iodo-4-methoxybenzamide of patients with suspected primary breast cancer: first clinical results. J Nucl Med. 2002;43:1647–9.
277. Jonson SD, Bonasera TA, Dehdashti F, Cristel ME, Katzenellenbogen JA, Welch MJ. Comparative breast tumor imaging and comparative in vitro metabolism of 16[alpha]-[^{18}F] Fluoroestradiol-17[beta] and 16[beta]-[^{18}F]fluoromoxestrol in isolated hepatocytes. Nucl Med Biol. 1999;26:123–30.
278. Dehdashti F, Flanagan FL, Mortimer JE, Katzenellenbogen JA, Welch MJ, Siegel BA. Positron emission tomographic assessment of "metabolic flare" to predict response of metastatic breast cancer to antiestrogen therapy. Eur J Nucl Med Mol Imaging. 1999;26:51–6.
279. McGuire AH, Dehdashti F, Siegel BA, et al. Positron tomographic assessment of 16{alpha}-[^{18}F] fluoro-17{beta}-estradiol uptake in metastatic breast carcinoma. J Nucl Med. 1991;32:1526–31.
280. Mortimer JE, Dehdashti F, Siegel BA, Trinkaus K, Katzenellenbogen JA, Welch MJ. Metabolic flare: indicator of hormone responsiveness in advanced breast cancer. J Clin Oncol. 2001;19:2797–803.
281. Mortimer JE, Dehdashti F, Siegel BA, Katzenellenbogen JA, Fracasso P, Welch MJ. Positron emission tomography with 2- F-18 fluoro-2-deoxy-D-glucose and 16 alpha- F-18 fluoro-17 beta-estradiol in breast cancer: correlation with estrogen receptor status and response to systemic therapy. Clin Cancer Res. 1996;2:933–9.
282. Linden HM, Stekhova SA, Link JM, et al. Quantitative fluoroestradiol positron emission tomography imaging predicts response to endocrine treatment in breast cancer. J Clin Oncol. 2006;24:2793–9.
283. Dehdashti F, Picus J, Michalski JM, et al. Positron tomographic assessment of androgen receptors in prostatic carcinoma. Eur J Nucl Med Mol Imaging. 2005;32:344–50.